MESOSCALE PREDICTABILITY OF AN EXTREME WARM-SEASON PRECIPITATION EVENT

A Thesis

by

ANDREW MICHAEL ODINS

Submitted to the Office of Graduate Studies of
Texas A&M University
in partial fulfillment of the requirements for the degree of

MASTER OF SCIENCE

December 2004

Major Subject: Atmospheric Sciences

MESOSCALE PREDICTABILITY OF AN EXTREME WARM-SEASON PRECIPITATION EVENT

A Thesis

by

ANDREW MICHAEL ODINS

Submitted to the Office of Graduate Studies of
Texas A&M University
in partial fulfillment of the requirements for the degree of

MASTER OF SCIENCE

Approved as to style and content by:

Fuqing Zhang (Co-Chair of Committee)	John Nielsen-Gammon (Co-Chair of Committee)
Edwin A. Smith III (Member)	Richard Orville (Head of Department)

December 2004

Major Subject: Atmospheric Sciences

ABSTRACT

Mesoscale Predictability of an Extreme Warm-Season Precipitation Event.

(December 2004)

Andrew Michael Odins, B.S., The University of Louisiana at Monroe;

B.S., University of New Mexico

Co-Chairs of Advisory Committee: Dr. Fuqing Zhang
Dr. John Nielsen-Gammon

During the period of June 29 through July 6, 2002, an extreme precipitation event occurred over Texas, resulting in catastrophic flooding. Operational forecasts performed poorly, neither predicting the copious amounts of rain nor its longevity. The Penn State University/NCAR Mesoscale Model version 5 (MM5) was used to conduct predictability experiments, which follow closely to the research conducted by Zhang et al. A control simulation initialized at 00Z 1 July is established over a 30-km grid. First, practical predictability experiments are performed by exploring the impacts due to different lead-times, resolution dependence, and different physics parameterizations. Second, intrinsic predictability is investigated by inducing a random temperature perturbation in the initial conditions, followed by numerous simulations with various perturbed initializations. Similar results to those found by Zhang et al. were discovered here: the prominent initial error growth is associated with moist processes leading to convection. Eventually these errors grow from the convective scale to sub-synoptic scale, essentially below 1000 kilometers. This indicates that as the forecast time extends further beyond initialization, the resulting errors will impact forecasts of larger-scale features such as differences in the

positioning and intensity of positive PV anomalies and distribution of precipitation from the control simulation.

ACKNOWLEDGEMENTS

I would like to thank the Department of Atmospheric Sciences at Texas A&M University. I want to thank Dr. Fuqing Zhang, my committee chair, for his support and development of my understanding of predictability. He has provided support for my endeavors, as well as computational support. I would like to thank Dr. John Nielsen-Gammon, my co-chair, for his advice and development of my understanding of the dynamic features of this case. I thank him for an assistantship in the Office of the State Climatologist, as well as other opportunities in support of my research. I would also like to thank my other committee member, Dr. Art Smith, for his help with the basic understanding of financial risk, advice and support.

I would like to thank Reliant Energy for an internship opportunity, and those I worked with. It was during my internship that the 2002 Texas Flood event occurred, which caused me difficulties in forecasting for Reliant's needs. This sparked an interest in researching this event to understand the mechanisms behind predictability.

I would like to thank the graduate students at Texas A&M for their support and friendship. I would like to thank Nyzette Rydell and the employees at the National Weather Service in New Braunfels, Texas for graphics and support of my research endeavors.

Last, but certainly not least, I would like to thank my family. I want to thank my wife, Shari, for all of her understanding and support. I want to thank Emily, my daughter for her love and the constant reminder of the successes that my wife and I achieve everyday. And I want to thank my parents for their moral support and encouragement.

TABLE OF CONTENTS

CHAPTER Page

LIST OF FIGURES

FIGURE Page

FIGURE Page

LIST OF TABLES

CHAPTER I

INTRODUCTION

On 29 June 2002, a heavy rainfall event was initiated over central Texas that lasted through 7 July 2002. Several counties in the Edwards Plateau and South Central regions received excessive amounts of precipitation, causing flooding, millions of dollars in damages and loss of life. Operational models used at the National Centers for Environmental Prediction (NCEP) had forecasted some heavy precipitation in the area; however, the rainfall amounts and duration of the storm event were not predicted well even within a 36-hour forecast. It is hypothesized that forecast models tend to produce errors within the vicinity of heavy precipitation, particularly at the mesoscale. The motivation behind this research is to explore the limits of mesoscale predictability of an extreme summer-time weather event, and comparing the results to a similar predictability study of a winter-time extreme weather event.

1.1 Background on mesoscale predictability

Predictability, applied to a numerical weather prediction (NWP) model, has been a topic of interest for many researchers. Investigations, by Lorenz (1963, 1969), explored the limits of predictability based on the chaotic nature of the dynamics of the atmospheric system (Schneider & Griffies 1998). Predictability can be best explained as the capability to which the future state of the atmosphere can be predicted based on the initial state of the forecast variables. The degree of predictability comes from the inability to

---

This thesis follows the style of the *Journal of the Atmospheric Sciences.*

know the exact state of the atmospheric variables both in the past and present timeframes. Since the initial state of the atmosphere is not known, errors in the initial conditions are incorporated into a forecast model, and the forecast model itself has deficiencies (Kalnay, pp 205-208).

Lorenz (1969) proposed that a finite limit of predictability would be reached despite improvements in initial conditions. His conclusions were based on error growth at small scales; despite improvements, errors would originate at smaller scales and would grow rapidly ultimately affecting larger scales. As a result of this rapid error growth, there would exist a finite limit of predictability, since steady improvements in the initial conditions would yield decreasing improvements in forecast length and quality. This notion is also known as *intrinsic* predictability; theoretically if there existed a perfect model, and initial conditions were near perfect, there still would be this finite limit of predictability (Zhang et al 2003, hereafter ZSR03). In contrast, *practical* predictability is the overall ability to forecast, encompassing both the model imperfections and the uncertainties in the initial conditions (Lorenz 1996, ZSR03). The focus of this study will be the random error growth at the mesoscale, more specifically the impacts of moist physics, initial conditions, and resolution of a numerical model on both practical and intrinsic predictability. It is important for this research to focus on the mesoscale since that is the scale of convective systems, and hence the probable scale of the fastest growing model errors.

Previous studies have shown that small errors expand in magnitude and scale as the model forecast advances further in time. These investigations have explored mesoscale predictability but have not determined the mechanisms behind the error

growth. Most recently, Zhang et al. (2002, hereafter ZSR02) have established in at least one instance that forecast differences grow rapidly at small scales with moist processes. ZSR02 researched the "surprise" snowstorm of 24-25 January, 2000 that unleashed enormous amounts of snow along the eastern coast of the United States. This event is of interest due to the inadequacy of the forecasts provided by the operational models, particularly the inability to predict the quantity of precipitation that occurred. The experiments showed that differences at small scales grew rapidly in the presence of moist physics. Dry processes, or those without latent heat release, had an error growth rate much slower than the moist simulations; therefore, the result is improved predictability at the mesoscale. Model resolution also impacted error growth in a manner similar to that proposed by Lorenz. Model differences grew faster at higher resolution and at smaller scales which ultimately indicates there exists an intrinsic limitation to predictability (ZSR02).

ZSR03 focused on the impacts of moist convection on predictability at the mesoscale. This research continued that of ZSR02, but it explored error development and growth both at high- and low-resolution simulations. The study concluded that errors at small scales, between 100-200 km within the first six-hour forecast, grew rapidly; these differences then expanded to larger scales, ultimately affecting the "subsynoptic-scale structure of the surface low," while the small scale error growth slowed (ZSR03). Moist convection appeared to be the primary source of initial rapid error growth at the low resolution of 30-km grid spacing. Similarly, a high-resolution simulation of 3.3-km grid spacing showed that the greatest differences between the control and perturbed runs occurred in the vicinity of convective cells. These results coincide with Lorenz's theory

of the limits of predictability; even with improvements, this poses the question of how far present model forecasts are from *the* limit of predictability in the mesoscale.

1.2 Methodology and objectives

The ability to predict the future state of the atmosphere is largely dependent on the accuracy of the forecast by numerical models. This research will focus on mesoscale predictability in a one- to two-day timeframe with a state-of-the-art numerical weather prediction model. Specifically, complementary to ZSR02 and ZSR03, this study will investigate mesoscale predictability, both practically and intrinsically, for the extreme precipitation event introduced in the previous subsection. However, there are notable mesoscale/synoptic differences between ZSR02 and ZSR03 and this research; this event is warm-season with low baroclinicity, and there is stronger convective instability. The present investigation will explore a late June, early July subtropical event, in a much smaller locale, where temperature contrasts will be minimal, compared to the cold-season extreme event that encompassed a greater area studied in ZSR02 and ZSR03. With regards to research methodologies, this examination will utilize random grid perturbations and will explore effects of various physics parameterization schemes both practically and intrinsically. Using random temperature perturbations with a specified standard deviation distributed over the model grid points, an assessment of the rate of error growth and the forecast period of maximum growth rate is determined. Since atmospheric variables often are at “critical” points, the induction of a very small temperature perturbation can yield a rapid error growth in the early forecast period (ZSR03).

Similar to ZSR03, this research will examine intrinsic predictability through (1) the evolution of small-scale small-amplitude errors and their growth dynamics, including diurnal growth rates, (2) the impacts of model grid resolution on error growth, and (3) the impacts of model physics, including moist convection and different physics parameterizations. The 2002 Summer Texas Flood event ('02 Flood hereafter) lasted for a longer duration than the Surprise Snowstorm of 2000, and therefore it will be important to see the error behavior during different days and times of initialization. ZSR03 found that model resolution (high resolution) contributed to rapid error growth during the early forecast period; therefore high resolution error growth will be investigated in this case. Difference growth (divergence of a control simulation compared to a perturbed simulation) due to varying the physics parameterization schemes, specifically individual changes to the cumulus, microphysics, and planetary boundary layer (PBL hereafter) options within the model, will be explored. Lastly, determination of error growth stemming from moist physics will include simulations comparing one run with moist physics with one in which latent heat will be turned off. Results from ZSR03 showed that without moist processes, error growth was reduced in the early forecast period.

The present research will also explore practical predictability, but will involve methods relatively different from ZSR02. First, an assessment of the precipitation forecast resulting from different lead times will be examined. Next, resolution dependence on forecasted rainfall, a similar experiment to ZSR02, will be determined. Lastly, individual changes to the model physics parameterization schemes will be conducted to see the impacts on the accumulated precipitation forecast. The primary objective behind these experiments is to determine the value of the forecast, essentially to

mimic complications that may arise in operational forecasting and to diagnose potential constraints within a forecast model.

This research will incorporate the Pennsylvania State University-National Center for Atmospheric Research (PSU-NCAR) nonhydrostatic fifth-generation Mesoscale Model (MM5) version 3.6 (Dudhia 1993) using ETA GCIP data (details to be discussed in a subsequent section) to simulate an idealized forecast. The simulation will run for a total of 36-hours which will (1) focus on the time-frame that the operational NCEP models began to lose accuracy, and (2) explore the limits of predictability within the mesoscale timeframe. An investigation into model initial conditions and configuration, by comparison with the idealized forecast, will show model biases and sources and timing of error growth.

Motivation behind this research originates with the complications in the operational forecasting of such an event. Both the amount of the rainfall and the duration of the ’02 Flood was not well simulated by the operational models (details discussed later). It is therefore important to explore the source of such complications from a practical standpoint. However, if given a perfect model, errors may still develop, and the mechanisms by which these errors develop and grow are also of interest.

1.3 Outline of thesis

Following the introduction to mesoscale predictability and objectives of this research, Chapter II will have an overview of the ’02 Flood. This will include a summary of the heaviest rainfall and a detailed mesoscale/synoptic analysis. Chapter III will detail the experimental design, and will included an overview of the data used for this study, a model description, a comparison of a control simulation with observations, and a

description of experiments to be employed. Chapter IV will include the results of the practical predictability experiments, and Chapter V will include intrinsic predictability results. Lastly, Chapter VI will include a summary and discussion of the research.

CHAPTER II

OVERVIEW OF THE FLOODING EVENT

2.1 Rainfall analysis and operational forecasts

The “surprise” snowstorm of 2002 is considered an extreme event due to the intensity of the system and the precipitation amount; when considering the predictability of this event, the interest lies in the failure of the operational models to forecast both the timing and amount of precipitation. At the present time, there has been very limited research conducted on the predictability of a summertime extreme event, in particular investigating the effects of moist processes.

Beginning early on June 29, 2002, and lasting through July 6, 2002, an extreme rainfall event occurred in Texas with the heaviest precipitation falling in the Edwards Plateau and South Central regions. This event delivered copious amounts of precipitation to San Antonio, Austin, and areas surrounding and between the two cities. Storm totals included: 16.16 inches (410mm) of rain at the San Antonio International Airport, with 9.52 inches (242 mm) falling on 1 July 2002, 34.17 inches (868 mm) at Camp Verde 3 W, 31.59 inches (802 mm) at Comfort 2, 30.75 inches (781 mm) at Sisterdale, 29.38 inches (746 mm) at Bankersmith, and 27.63 inches (702 mm) at Boerne (data acquired through NCDC). Fig. 2.1 shows an analysis of precipitation between 28 June 2002 12Z and 7 July 2002 12Z, which encompasses the storm duration; a dot indicates the location of the San Antonio International Airport (KSAT). The rainfall composites in Fig. 2.1 are compiled from NCEP daily precipitation data. The data are acquired from River Forecast Center and Climate Anomaly Data Base gauges; the data is then averaged

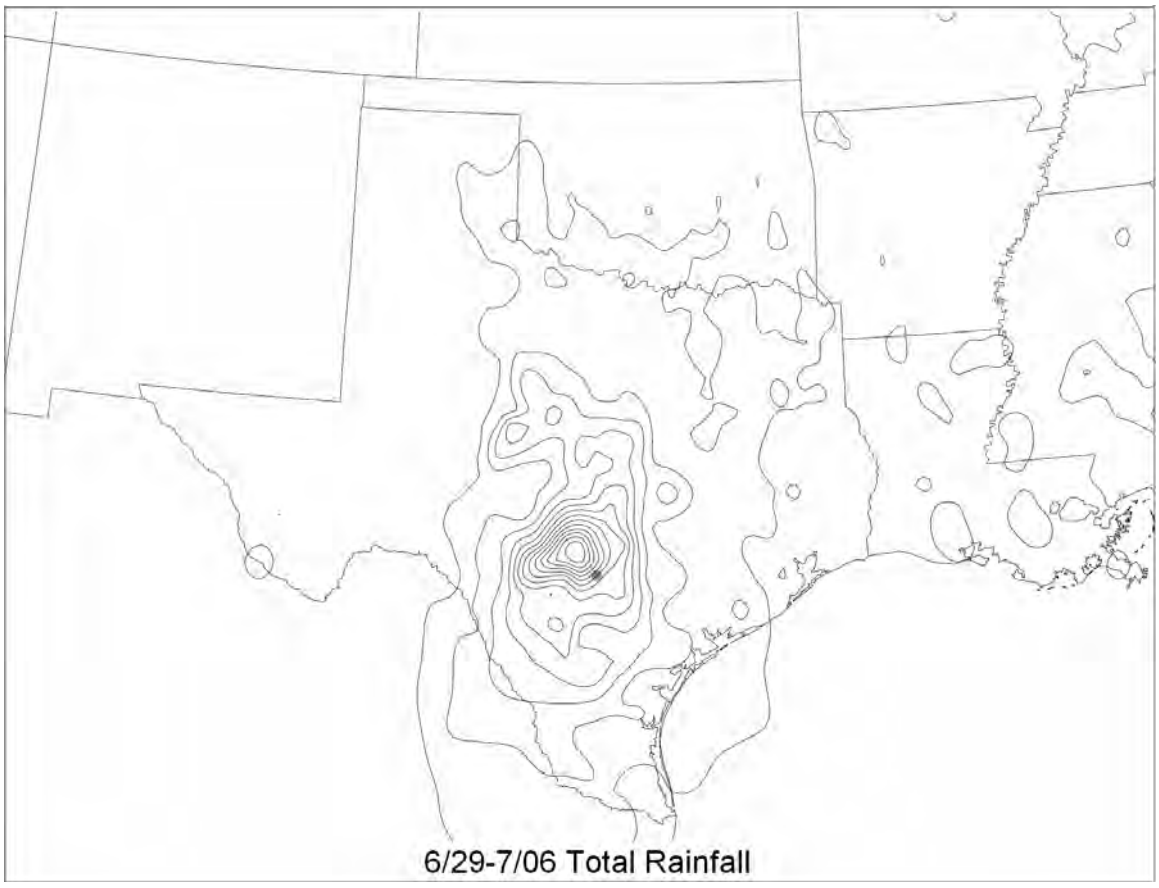

Fig. 2.1 Analyzed accumulated precipitation during the 2002 South-Central Texas flood ('02 Flood) for the 8-day period beginning on 28 June at 12Z. The San Antonio International Airport (KSAT) is indicated by the gray dot. Contours at every 50 mm.

with a resolution of 0.25 degree latitude by 0.25 degree longitude (NCEP). Although this was an extreme event, several other extreme rainfall events have occurred in Texas; some that have been investigated include: 1-4 August 1978 (Caracena and Fritsch, 1983), 16-19 September 1979 (Bosart, 1984), 16-19 October 1994 (Petroski, 2000), and 17-19 October 1998 (Scott, 2001). Although each event produced significant rainfall, the focusing mechanisms for the rainfall included synoptic-scale or mesoscale fronts, or topography, and several have been associated with tropical dynamics.

Figs. 2.2 and 2.3 show the 24-hour precipitation totals for each day of the storm event, using the same NCEP analysis data as in Fig. 2.1. When describing the precipitation observation for a given day, the date used will represent the 24-hour accumulated precipitation from 12Z of the previous day (i.e. the precipitation total for 29 June will cover 28 June 12Z through 29 June 12Z). Widely scatted precipitation fell on 29 June, with the southern portions of the state receiving the majority of rainfall. By 30 June, more widespread precipitation fell across the southeastern half of the state, with heavier rainfall near the Austin area. Rainfall continued in the central portions of the state, with the heaviest amounts occurring primarily in the South Central, Edwards Plateau, and Southern regions of the state for the next three days. The precipitation had slowly shifted away from the hardest hit areas towards the west by 4 July, but this relief was short-lived as heavier rain fell on central Texas on 5 July. By 6 July, convection was lighter as the system responsible for delivering the great quantity of rain moved to the west (details to follow in the next section) and into a more stable environment.

With such heavy precipitation, 29 counties experienced damages from flooding and were declared Federal Disaster areas by President George Bush. Rivers and streams

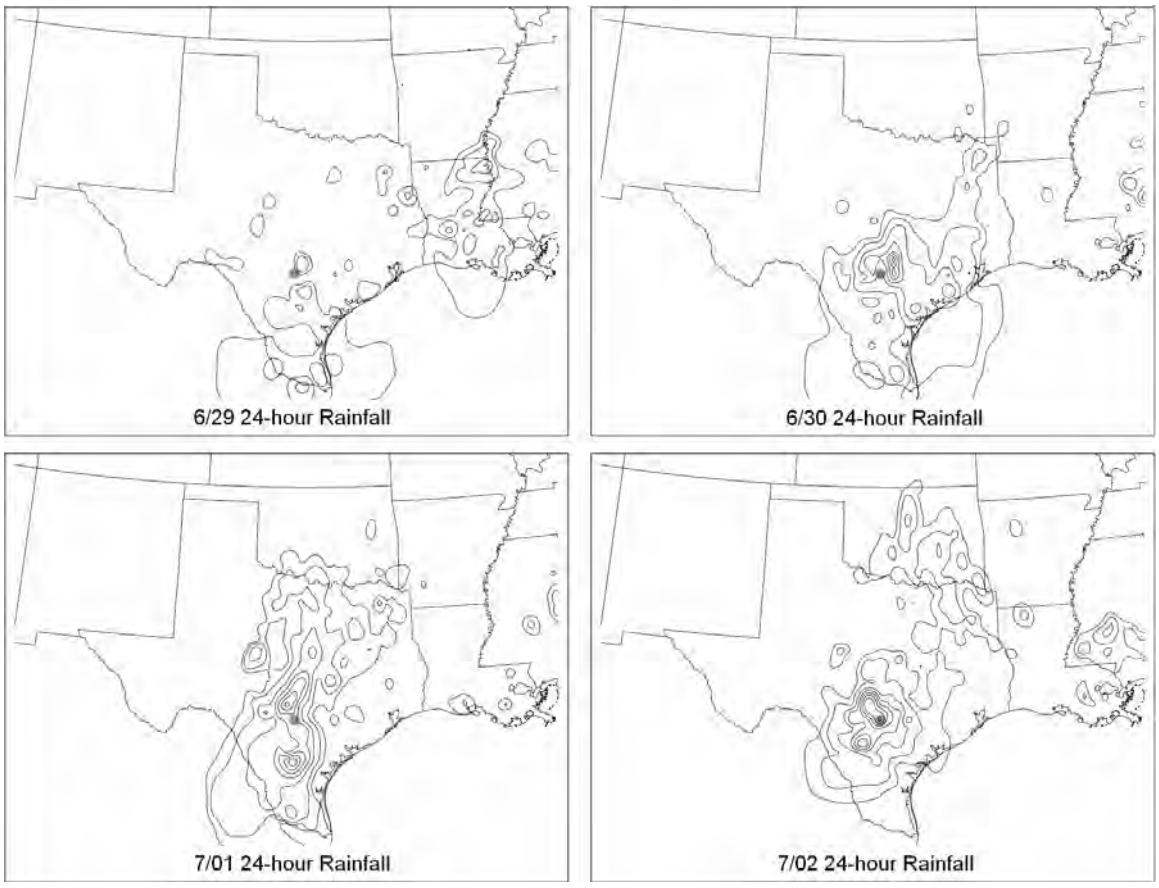

Fig. 2.2 Analyzed accumulated precipitation for successive 24-hour periods beginning and ending at 12Z. Contours are every 20 mm beginning with a 10 mm contour.

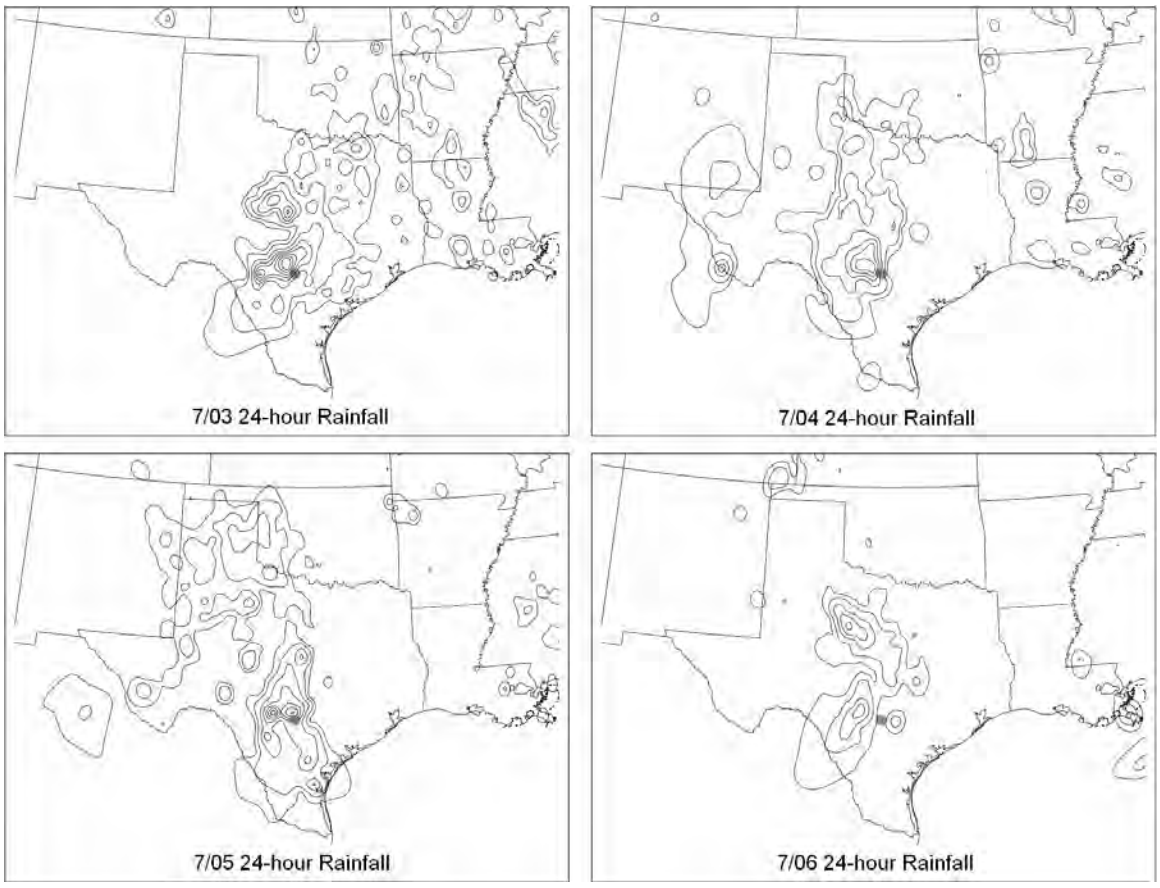

Fig. 2.3 24-hour accumulated precipitation, as in Fig. 2.2

flooded, and lake levels rose to record levels. Seven people lost their lives in flood waters and numerous homes were destroyed; damages are estimated to be near $500 million.

Analysis of ‘02 Flood will include evaluation of the synoptic and mesoscale features throughout the duration of the event, utilizing model initializations, as well as composite radar images and station soundings. This is followed by a brief discussion relating predictability to the conditions that were conducive for convective development and sustainability.

2.2 Synoptics

Hoskins et al. (1985) introduced isentropic potential vorticity (IPV) thinking as a way of describing the dynamics of weather phenomenon. This methodology considers regions of high PV anomalies with respect to the balance of atmospheric components such as wind and temperature. PV is conserved, but during rain formation, it can be generated at lower tropospheric levels and destroyed at upper tropospheric levels. The synoptic analysis of the ‘02 Flood will utilize IPV thinking to explain the mechanisms behind the catastrophic rainfall. The analysis is performed using the 0 hour forecast from the model output, and the southern boundary of the graphic is the lateral boundary used in the model.

On 29 June at 00Z, an upper-level vortex of approximately 3 PVU (where 1 PVU is $1*10^{6}m^{2}*K*s^{-1}*kg^{-1}$) is present south of Brownsville along the Mexican coast at the 350K isentropic level, seen in Fig. 2.4; the 350K isentropic level is representative in that it shows the important features that spanned several isentropic surfaces and controlled the upper-level wind patterns during this period. The 350K isentropic level will be used to show the upper-level features, PV and flow in the ‘02 Flood case that can contribute to

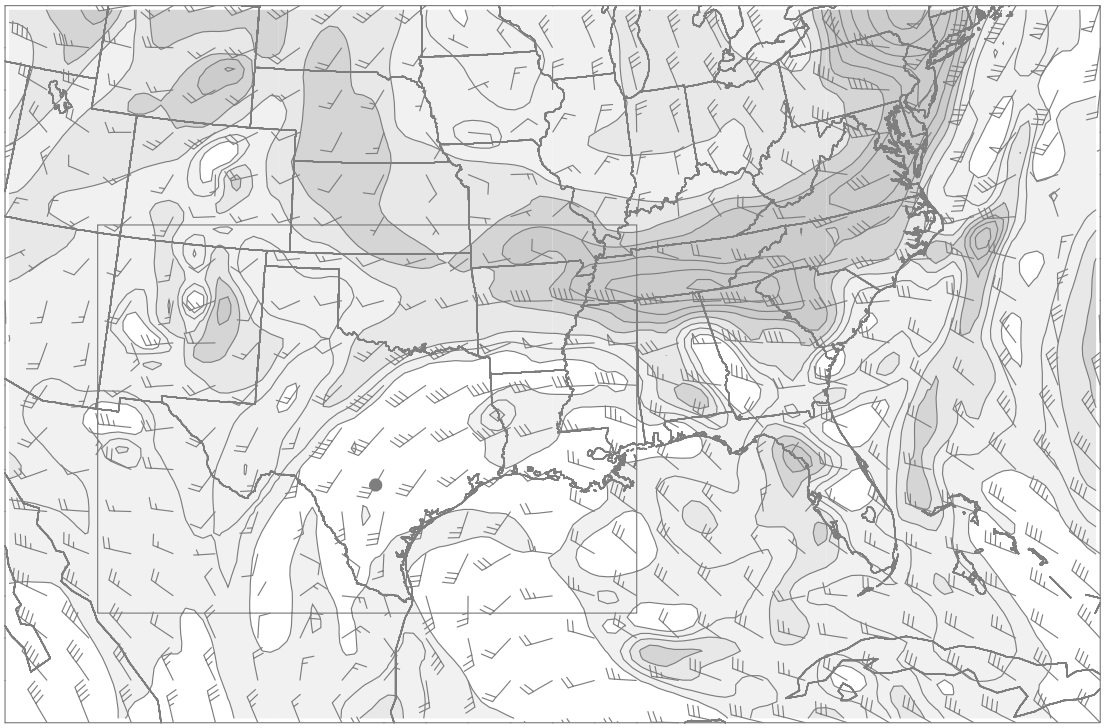

Fig. 2.4 Isentropic potential vorticity at 350K (shading, every 1 PVU) and wind vectors (full barb denotes 5 ms^{-1}) on 29 June at 00Z. Box denotes area of precipitation analysis.

the disturbances that lead to convection. The 20 to 30 ms^{-1} southerly winds along the Mexican coast are helping to advect this vortex towards Texas. Fig. 2.5 depicts the locations and parameters of vertical sections that will be used within this analysis: the sections are averaged over 300 km north-south, extend 1400 km east-west, and extend 14 km vertically, with a designation of A and B for the southern and northern cross-sections respectively. The purpose for averaging across 300 km is so that small-scale structure is not missed, as it potentially would be in a single plane, but without averaging away the significant features.

Fig 2.6 shows a vertical section of PV and isentropes (will be designated a PV-I section) for A, and the primary point of interest is the positive PV anomaly near the Texas Coast, extending down to 11 km, which corresponds to the vortex seen in the 350K isentropic analysis; this PV anomaly helps to provide the upper-level support for a convective environment. The other notable feature is the positive PV anomaly off the Texas Coast (flanked between the two solid lines below the X-axis on the graphic) centered at 328K, which is also present in the 320K isentropic analysis, Fig 2.7, as the small positive PV anomaly to the southeast of Brownsville. Winds at this vortex are east-southeast at 10 ms^{-1}, and will advect this anomaly towards the Mexican Coast, south of Brownsville. The 00Z Brownsville and Corpus Christi soundings (Figs. 2.8a and 2.8b, provided by the University of Wyoming) indicate convective available potential energy (CAPE, $J*kg^{-1}$) values at 743 and 1435 respectively. Precipitable water values (PWAT) for each sounding are over 50 mm, which is favorable for heavy rainfall (Petroski, 2000 and references therein).

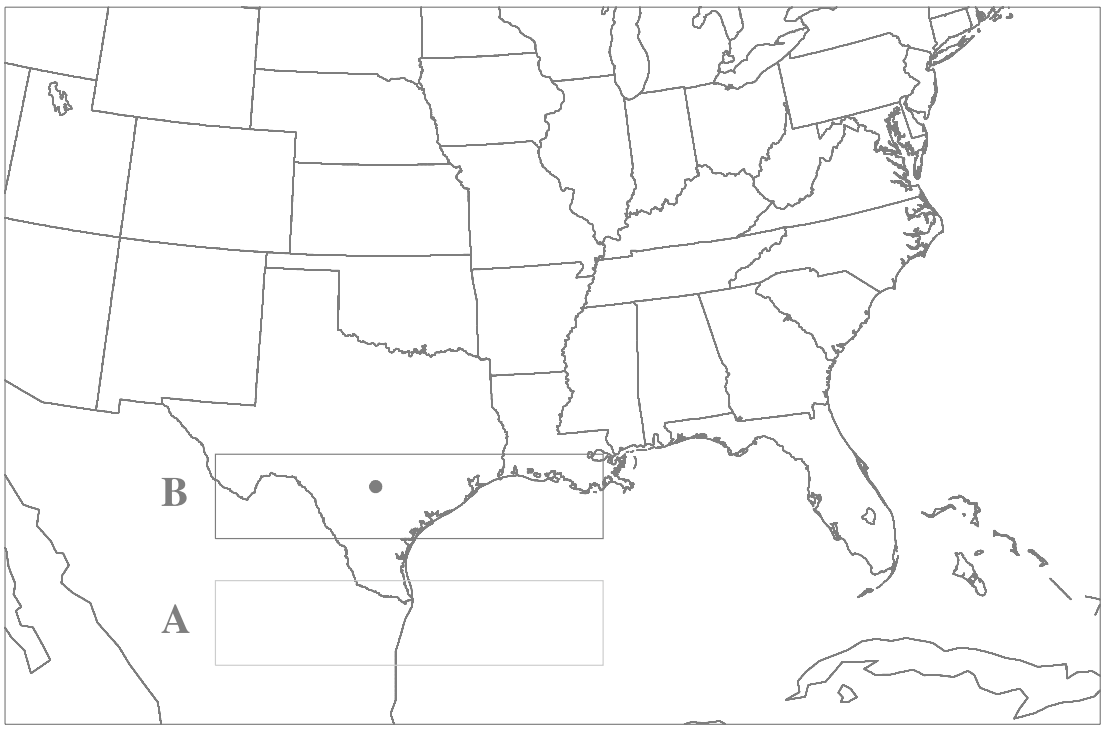

Fig. 2.5 Locations of the vertical sections, averaged over 300 km north-south, extend 1400 km east-west, and extend 14 km vertically.

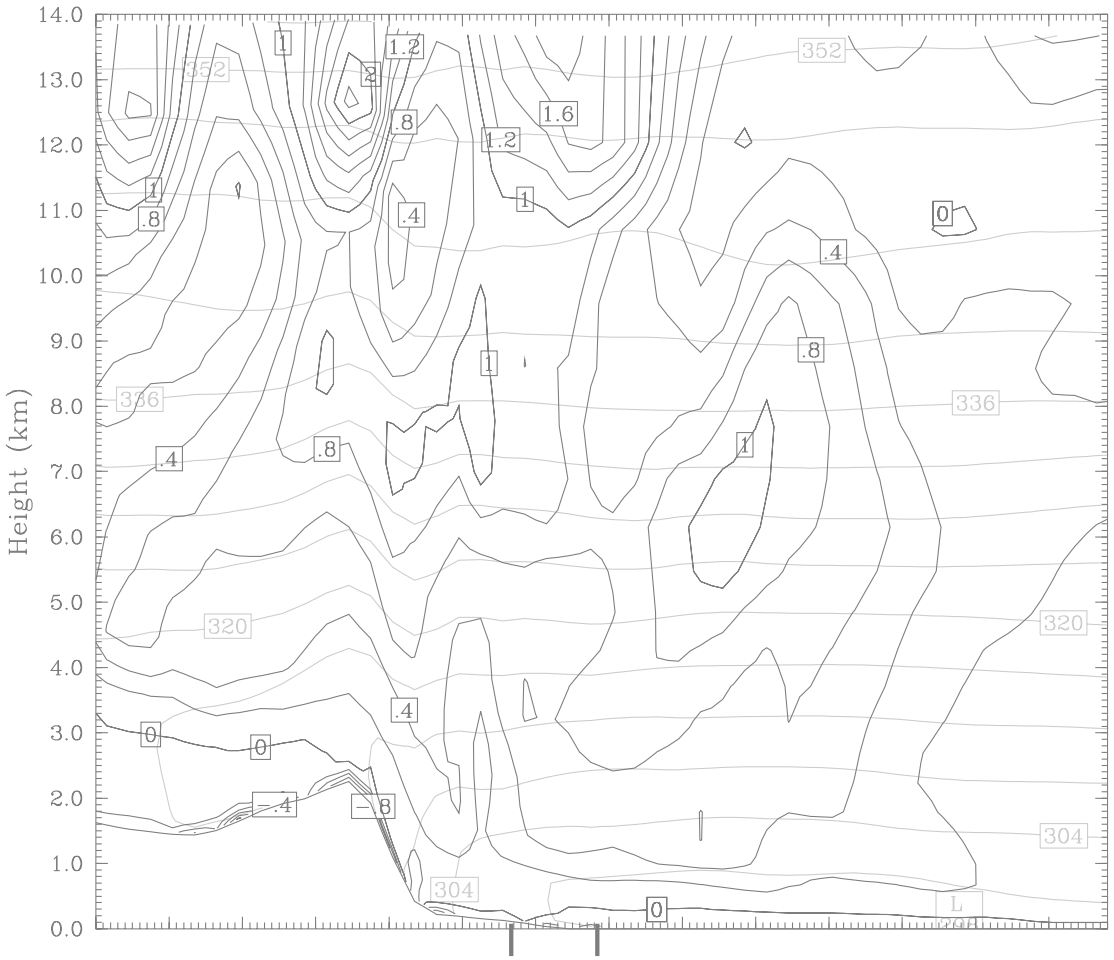

Fig. 2.6 Cross section (A) of potential vorticity (thin contours every 0.2 PVU, thick contours every 1.0 PVU) and isentropes (every 4K), valid at 00Z 29 June. The two lines below the X-axis represents the location of the Texas coast.

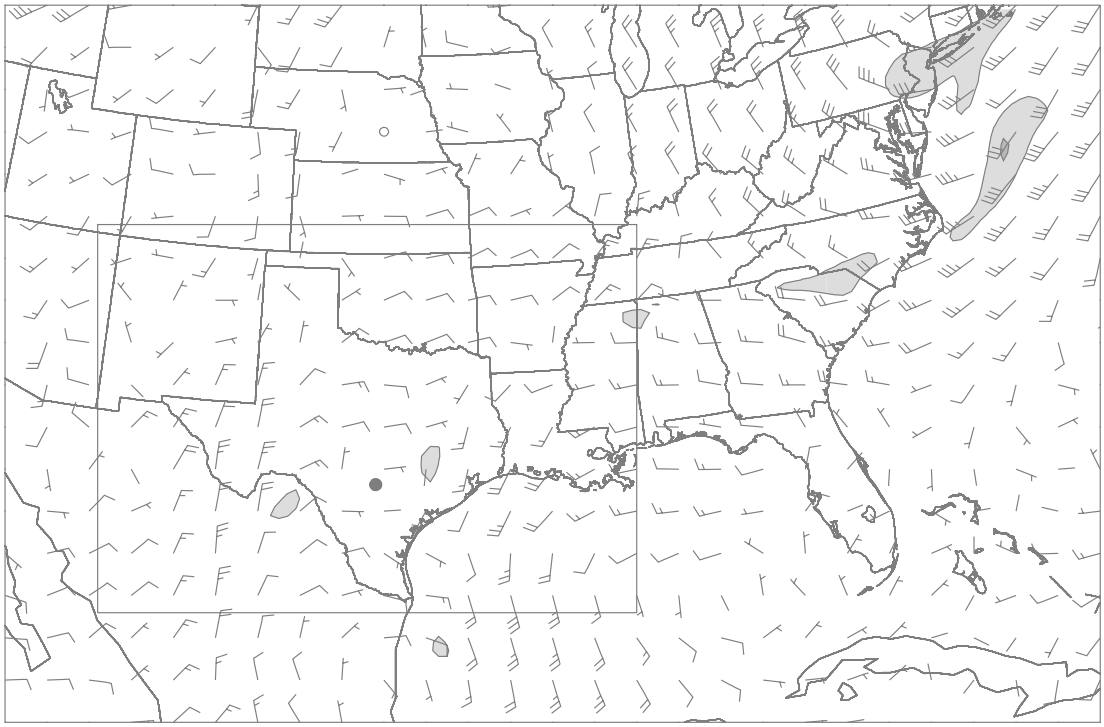

Fig. 2.7 Isentropic potential vorticity at 320K (shading, every 0.5 PVU) and wind vectors (full barb denotes 5 ms^{-1}) on 29 June at 00Z. Box denotes area of precipitation analysis.

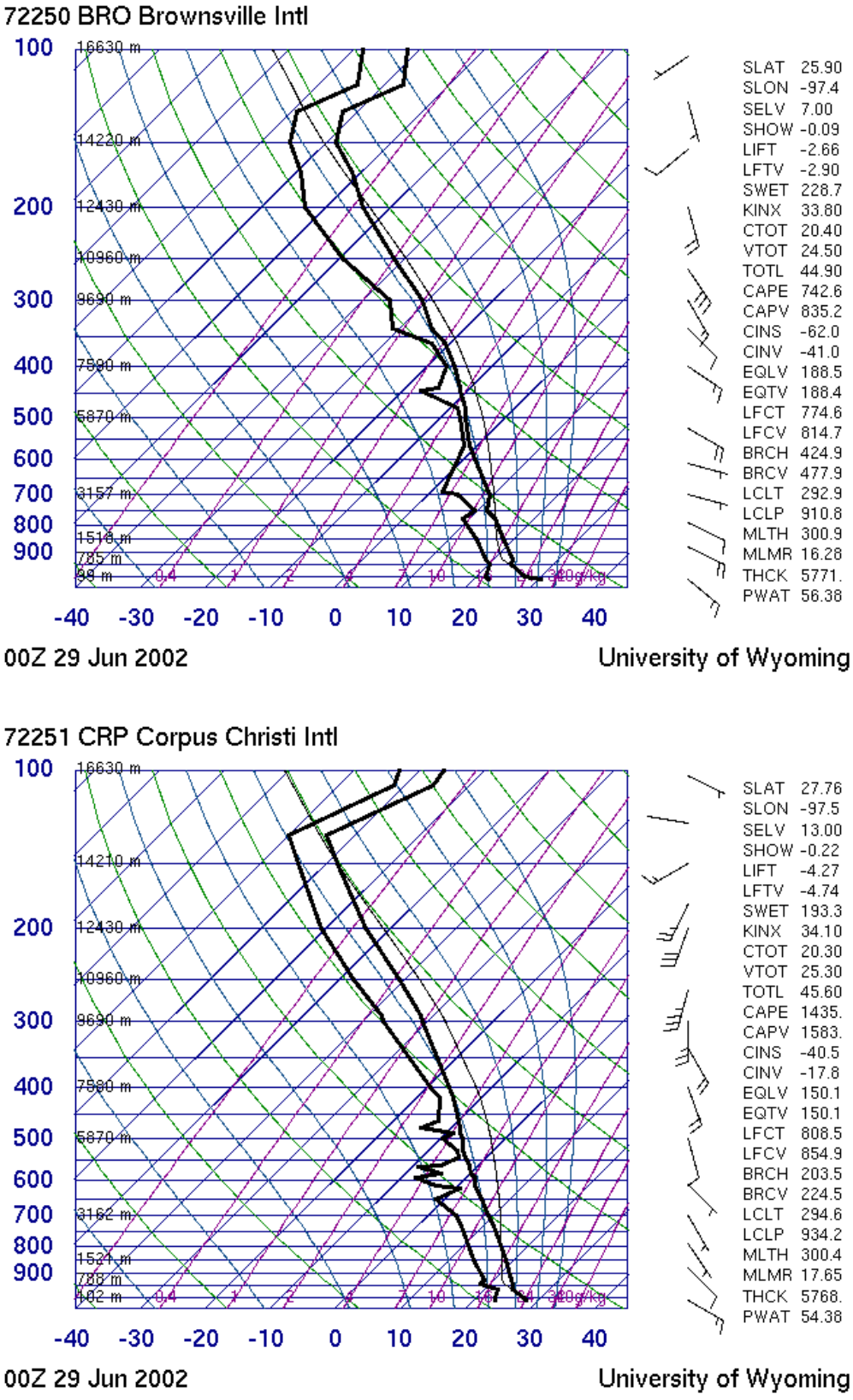

Fig. 2.8 Skew-T soundings on 29 June at 00Z for (a) Brownsville and (b) Corpus Christi.

Convection is first observed off the coast of Texas and Mexico at 9Z 29 June (not shown) in association with the 350K vortex described in Fig. 2.4; the convection according to radar is developing below the vortex 350K vortex. These storms move towards Brownsville and become a broad area of moderate rain and thunderstorms by 12Z (Fig. 2.9). A positive PV anomaly, located within the Brownsville vicinity at the 320K isentropic level (Fig 2.10), has been diabatically generated as evident by the convection seen in Fig 2.9; the location of the positive PV anomaly is positioned in the area of convection. A 950 hPa theta-e (θ_e) and wind analysis (seen in Fig. 2.11) shows elevated levels of θ_e off the southern Texas coast, in conjunction with the convection in that area. Warm-air advection, moisture advection, or surface fluxes contribute to higher θ_e which is indicative of greater instability. Since the winds near the Texas coast are from the south-southeast, coming from the Gulf of Mexico, it is speculated that the higher θ_e levels are a result of moisture advection. The normal-wind and relative humidity (NW-RH) cross-section of A, seen in Fig. 2.12, also shows RH to be through 70% over 6 km. The NW exhibit little vertical wind shear, which is important to the sustainability of the convection since the storms will not shear apart (Raymond et al, 1990).

Between 12Z 29 June and 00Z 30 June, the positive PV anomaly at the 320K isentropic level in the preceding paragraph advected northward across much of the South Central region of Texas (not shown) within 10 to 25 ms^{-1} southerly winds, and it has diabatically intensified into a deep vortex seen in Fig. 2.13 (coincides with the convection seen in radar, not shown). Cross-section B of NW-RH (Fig. 2.14) shows very little vertical wind shear, as well as high moisture content from the surface to 8.5 km, where

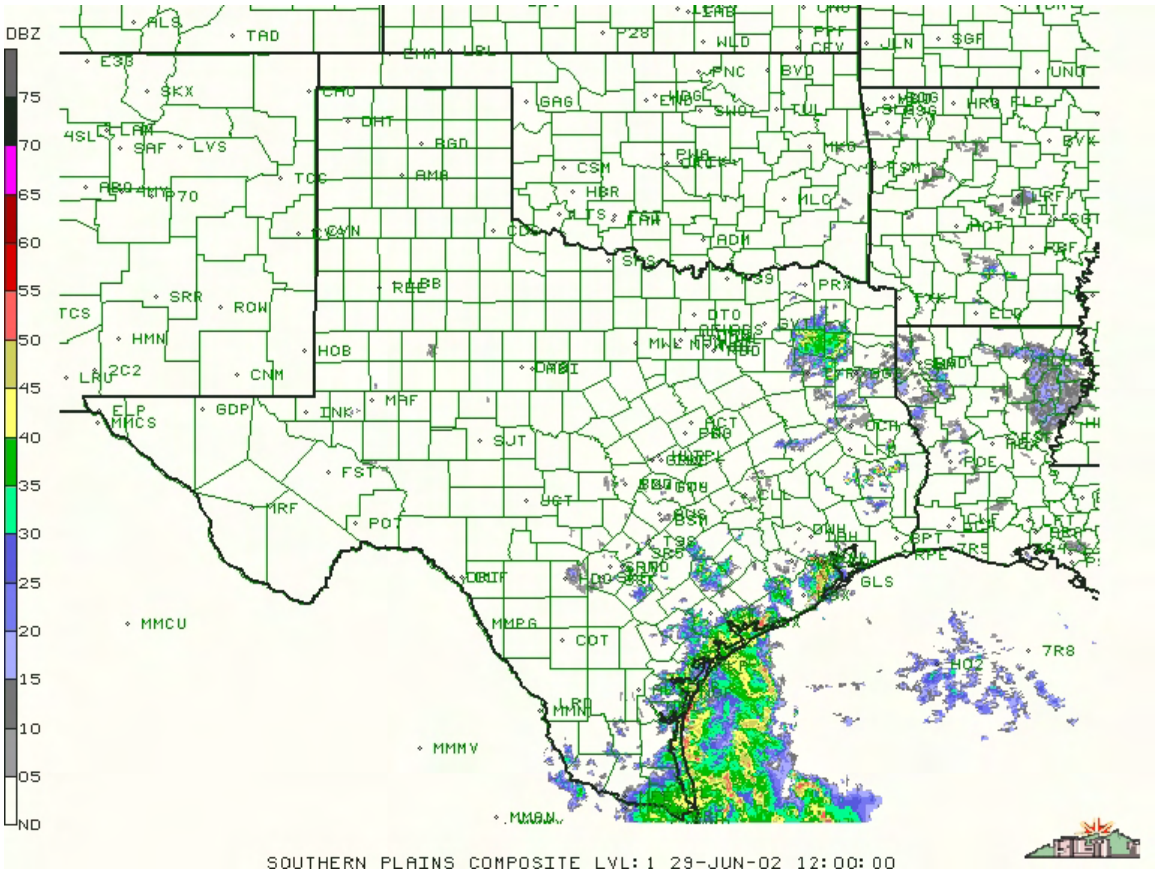

Fig. 2.9 Radar composite valid at 12Z 29 June.

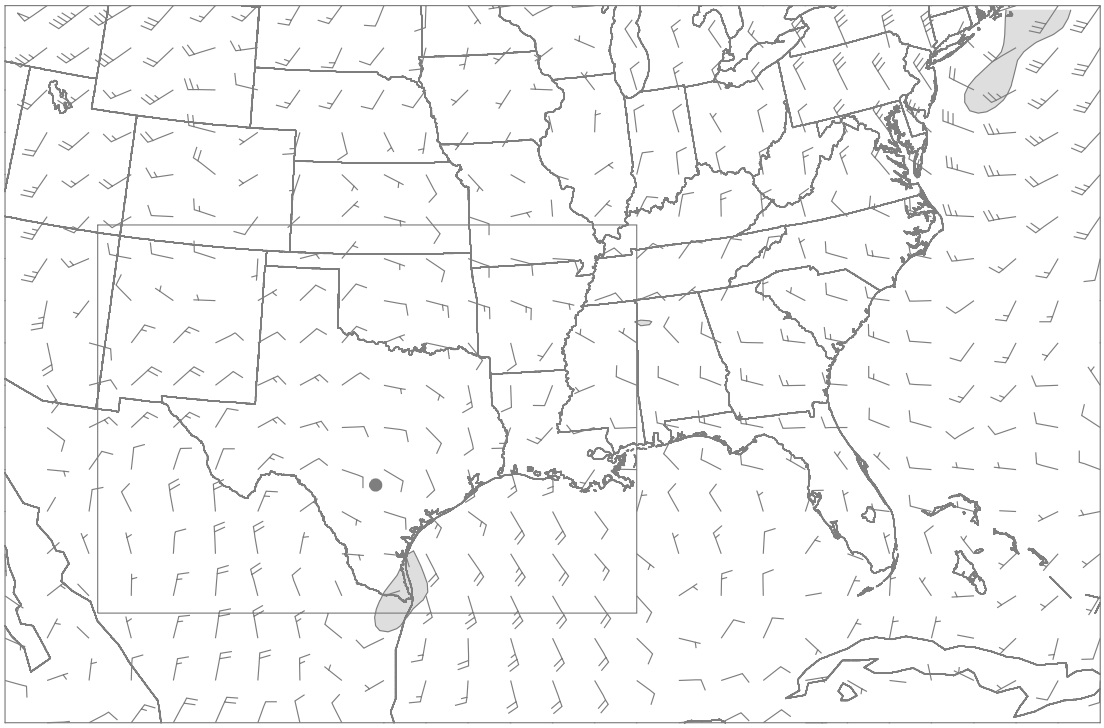

Fig 2.10 Isentropic potential vorticity and wind speed at 320K as in Fig 2.7, valid at 12Z 29 June.

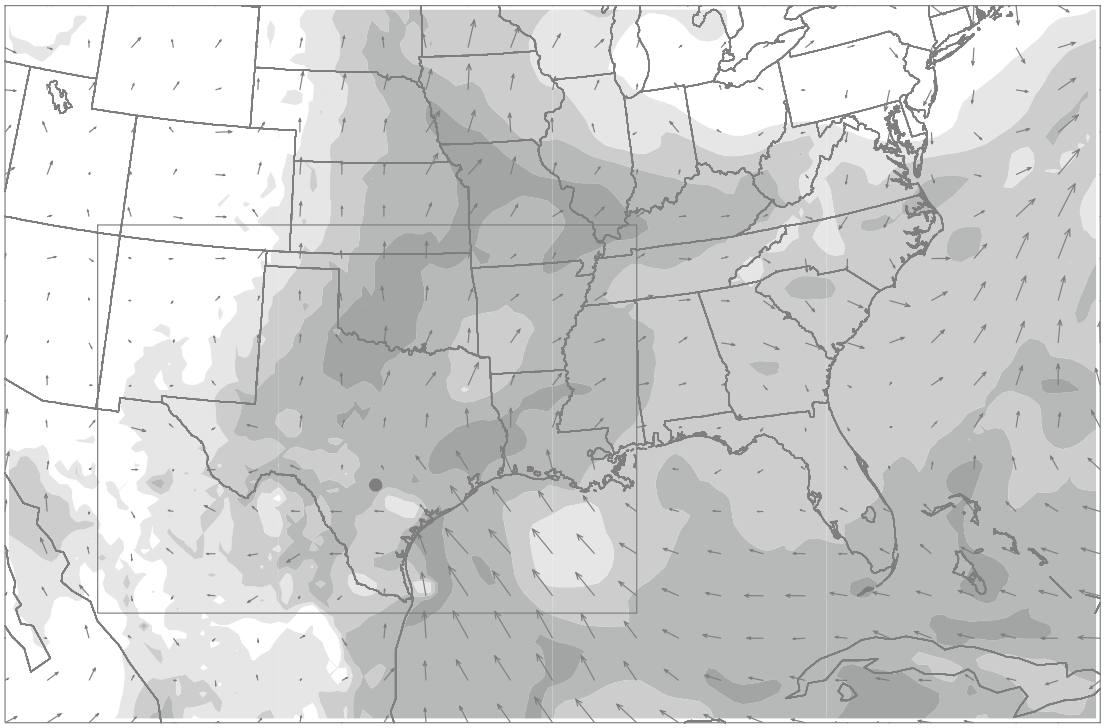

Fig. 2.11 Theta-e (shading every 6K beginning at 330K) and wind analysis at 950 hPa, valid at 12Z 29 June.

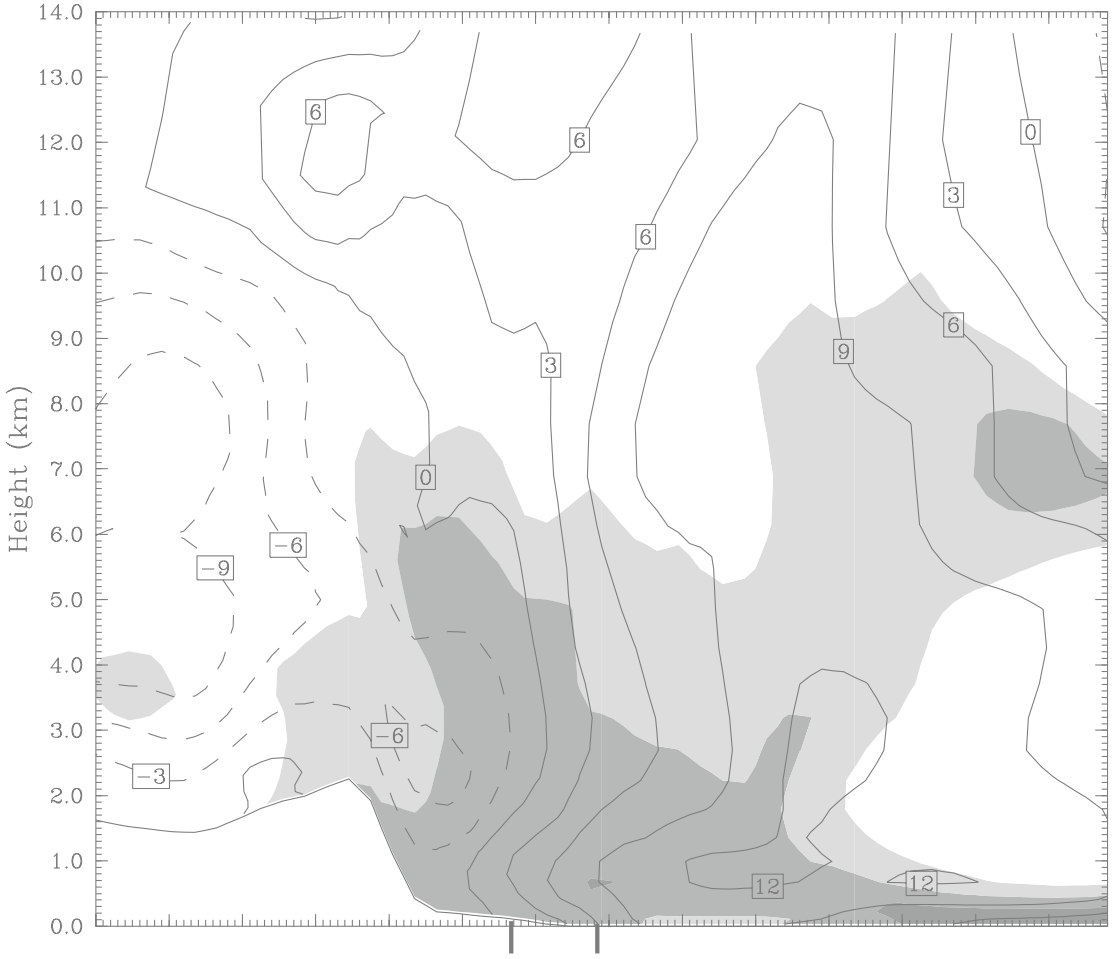

Fig. 2.12 Cross section (A) of normal wind and relative humidity with respect to water (shading, every 10% beginning at 70%), valid at 12Z 29 June.

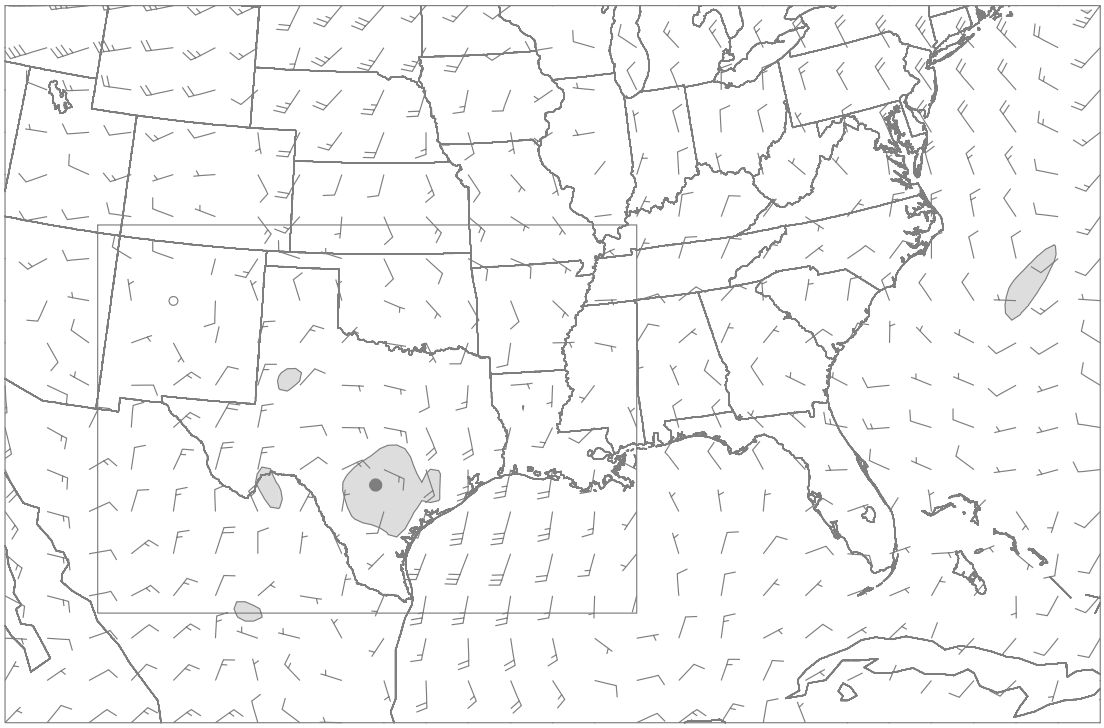

Fig. 2.13 Isentropic potential vorticity and wind speed at 320K as in Fig. 2.7, valid at 00Z 30 June.

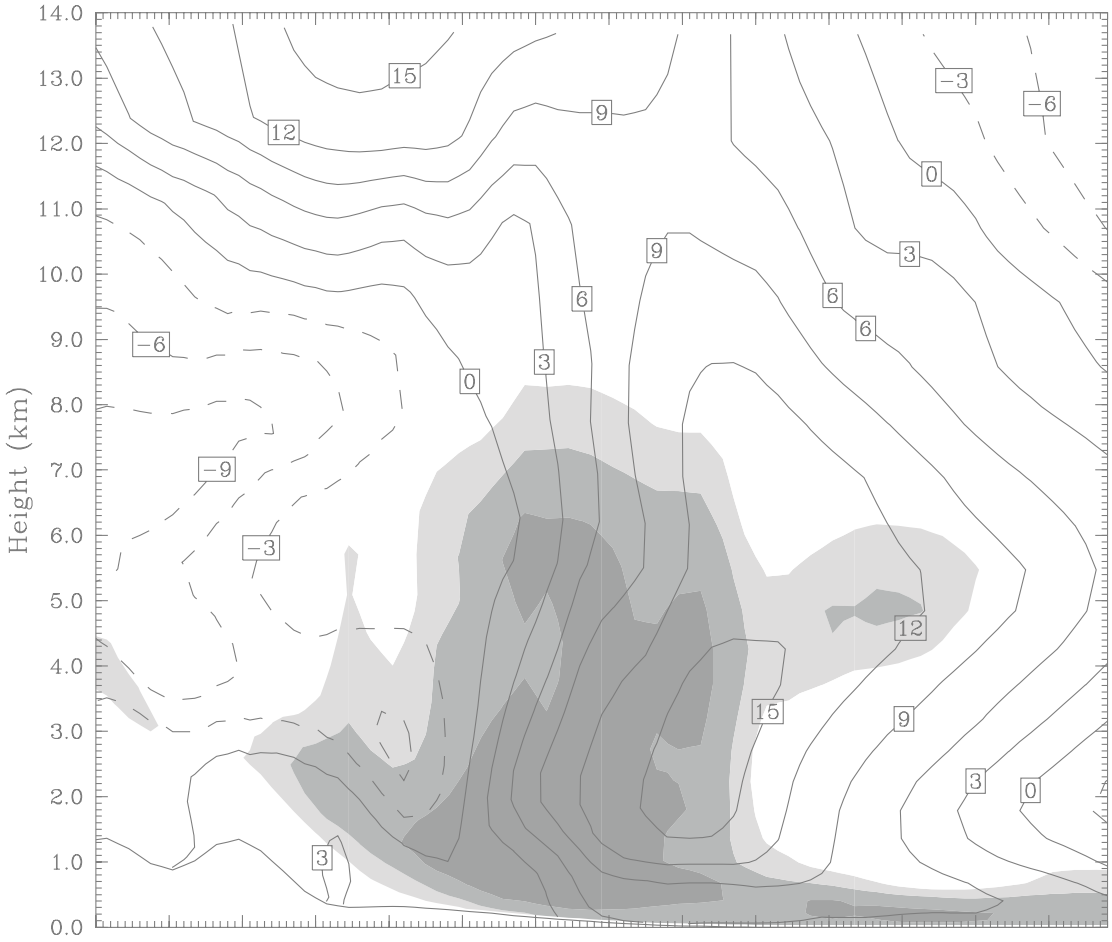

Fig. 2.14 Cross section (B) of normal wind and relative humidity as in Fig. 2.12, valid at 00Z 30 June.

convection is a plausible mechanism for the redistribution of the moisture. There has been an increase in θ_e levels (Fig 2.15) as well in the vicinity of the convection.

Between the times of 12Z 30 June and 12Z 1 July, the bulk of the original vortex, seen in the 320K isentropic analysis on 00Z 29 June, has advected northward and has intensified (not shown), and a small area of positive PV, positioned to the west of Brownsville, is also advecting northward. Fig. 2.16 shows the broad positive PV anomaly in northern Texas on 1 July at 00Z, but the vortex has weakened from over 2 PVU to 1.5 PVU, which correlates to reduced rainfall intensity according to radar (not shown). This positive PV anomaly is also being stretched due to the 20 ms^{-1} southerly winds to the east and 20 to 25 ms^{-1} northerly winds to the west of the vortex. A small positive PV anomaly is present near Laredo, Texas that continues to advect to the north, towards the San Antonio area. The onset of the heaviest precipitation near the San Antonio area, and generation of the mesoscale convective system (MCS), occurred between 00Z 1 July and 12Z 1 July. Fig. 2.17 shows the radar image at 12Z 1 July, indicating a large area of moderate to heavy convection over San Antonio and areas to the north, extending to Austin, which has contributed to a deep diabatically generated vortex, seen in a B cross-section of PV-I (Fig 2.18). This deep vortex can is also seen in the 320K isentropic analysis, with the center of the vortex over 2 PVU (Fig. 2.19).

By 2 July at 12Z, convection has initiated once again in south-central Texas, with strong showers in the San Antonio area according to radar (Fig. 2.20). An elongated trough can now be seen from the Texas-Mexico border near Brownsville that extends to northern Kansas (Fig. 2.21) according to the 320K isentropic analysis. The positive PV

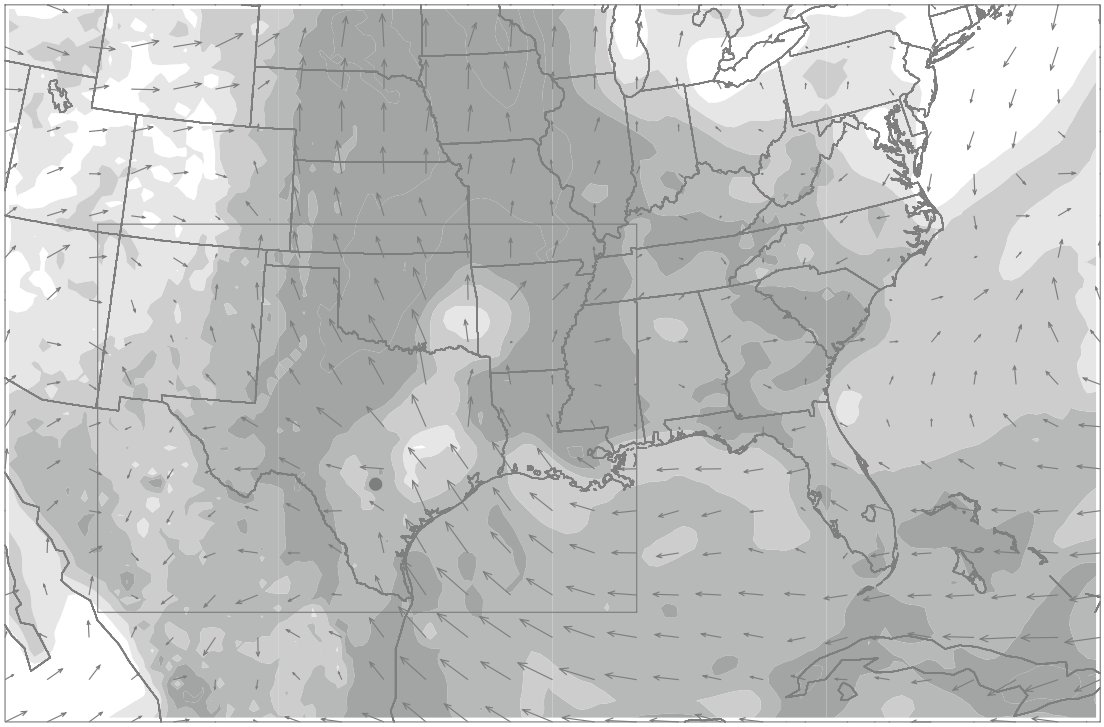

Fig. 2.15 Theta-e and wind analysis as in Fig. 2.11, valid at 00Z 30 June.

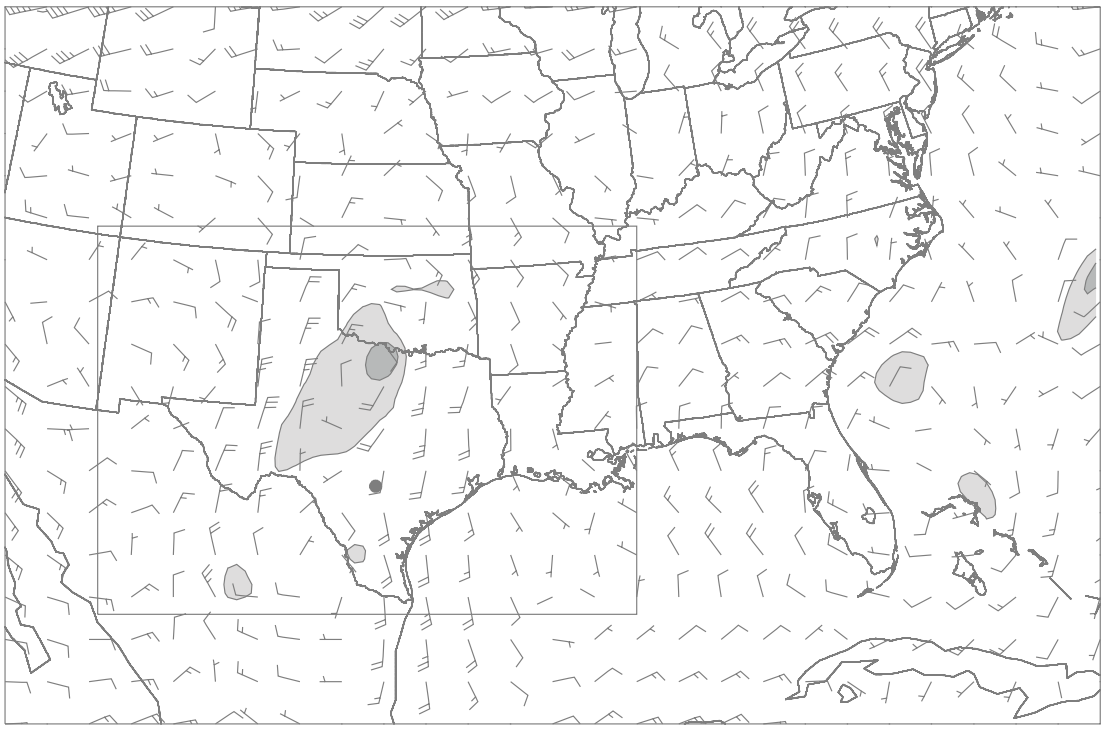

Fig. 2.16 Isentropic potential vorticity and wind speed at 320K as in Fig. 2.7, valid at 00Z 1 July.

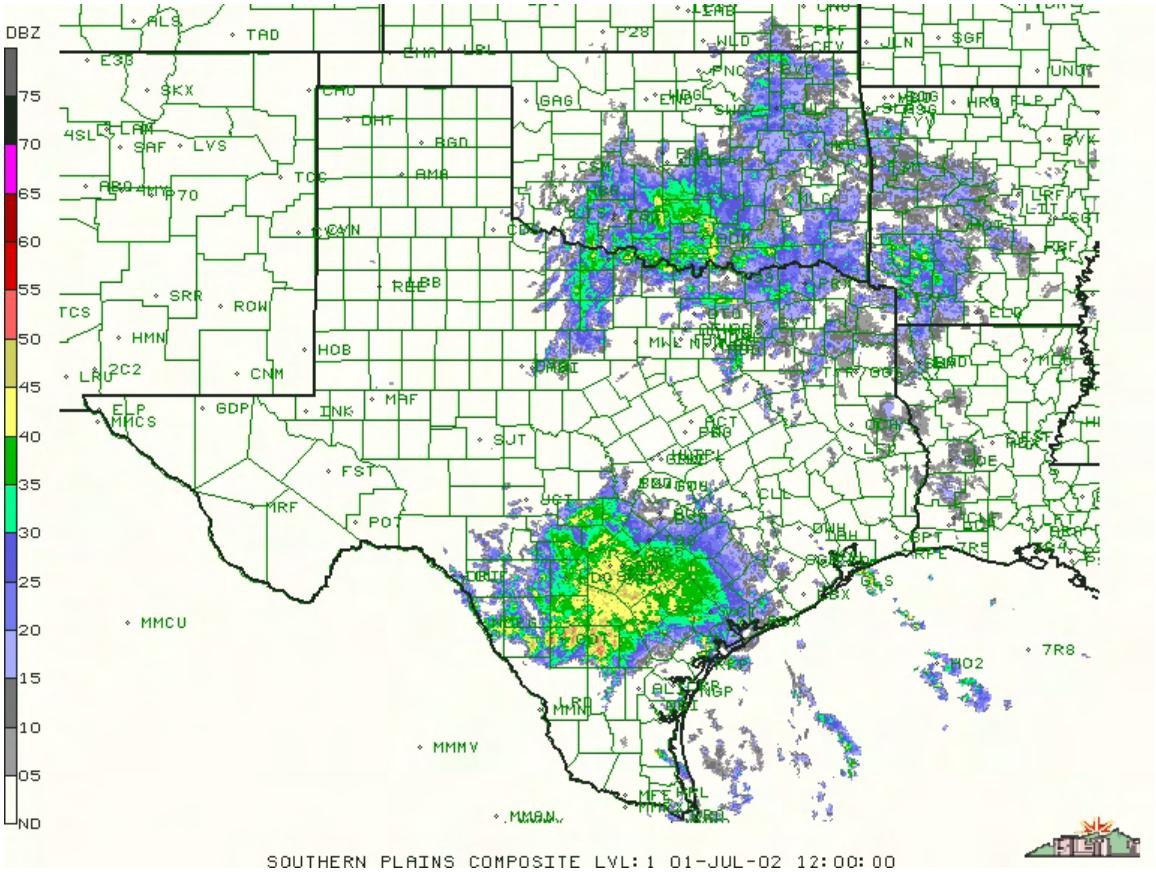

Fig. 2.17 Radar composite valid at 12Z 1 July.

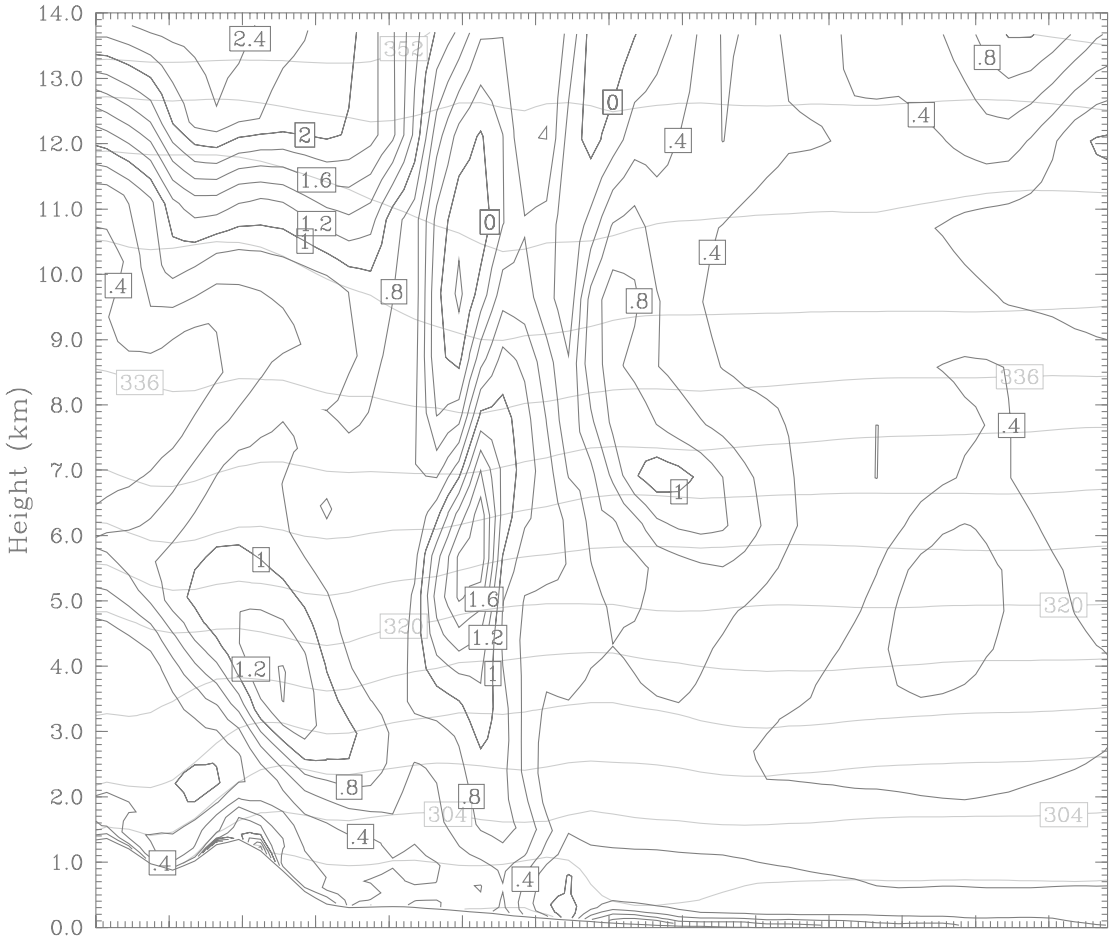

Fig. 2.18 Cross section (B) of potential vorticity and isentropes as in Fig. 2.6, valid at 12Z 1 July.

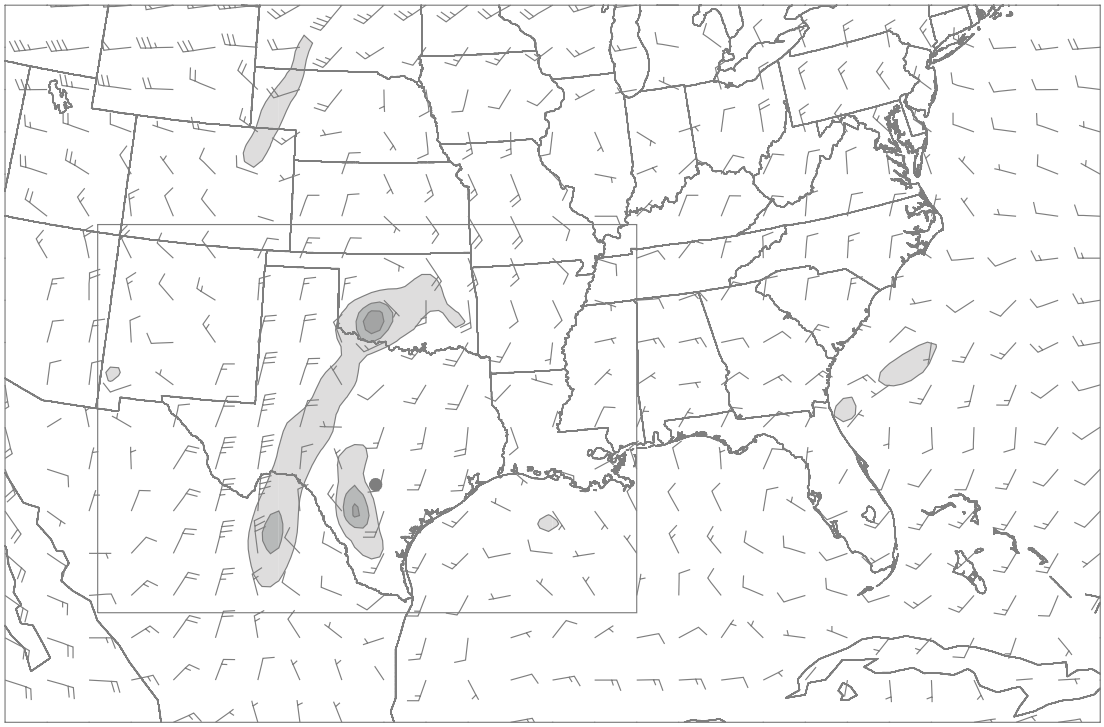

Fig. 2.19 Isentropic potential vorticity and wind speed at 320K as in Fig. 2.7, valid at 12Z 1 July.

anomaly has been sheared, with one section in central Texas advecting northward, and a finger in Mexico, south of Big Bend, advecting to the southeast. The southern edge of this PV finger will wrap around the southern edge of the shear zone and into the Edwards Plateau region, due to the northerly winds rotating toward the east near the southern edge of the trough. With weak winds (5 ms^{-1}) in the center and east of the northern positive PV finger, and rather weak winds to the west, the bulk of it will remain stationary with slight shearing. Again, another deep diabatically generated vortex has been established, and there is ample moisture and little vertical wind shear which is favorable for a convective environment (figures not shown).

At this point, several factors contribute to a self-perpetuating system, which includes a shear zone, sufficient moisture, positive PV, and little vertical wind shear. With a continued supply of warm, moist air from the Gulf of Mexico combined with little vertical wind shear, and reduced convective inhibition (not shown), convective development and diabatic generation of PV continues. The positive PV anomalies that are convectively generated, in association with a little vertical shear, can provide vertical motion (Raymond et al, 1990). For the next several days, between 3 July 00Z through 5 July at 12Z, a similar trend described in the preceding paragraph continues: the shear zone remains located from Mexico, south of Zapata, Texas extending toward northern Oklahoma. The positive PV anomaly continues to get stretched along the shear zone due to 15 to 30 ms^{-1} winds on the eastern edge, and 20 to 30 ms^{-1} winds on the western edge of the vortex. As the positive PV anomaly is advected southward, it encounters the southern edge of the shear zone, in which westerly winds help to advect it toward the Edwards Plateau region. The return flow from the southern edge of the shear zone

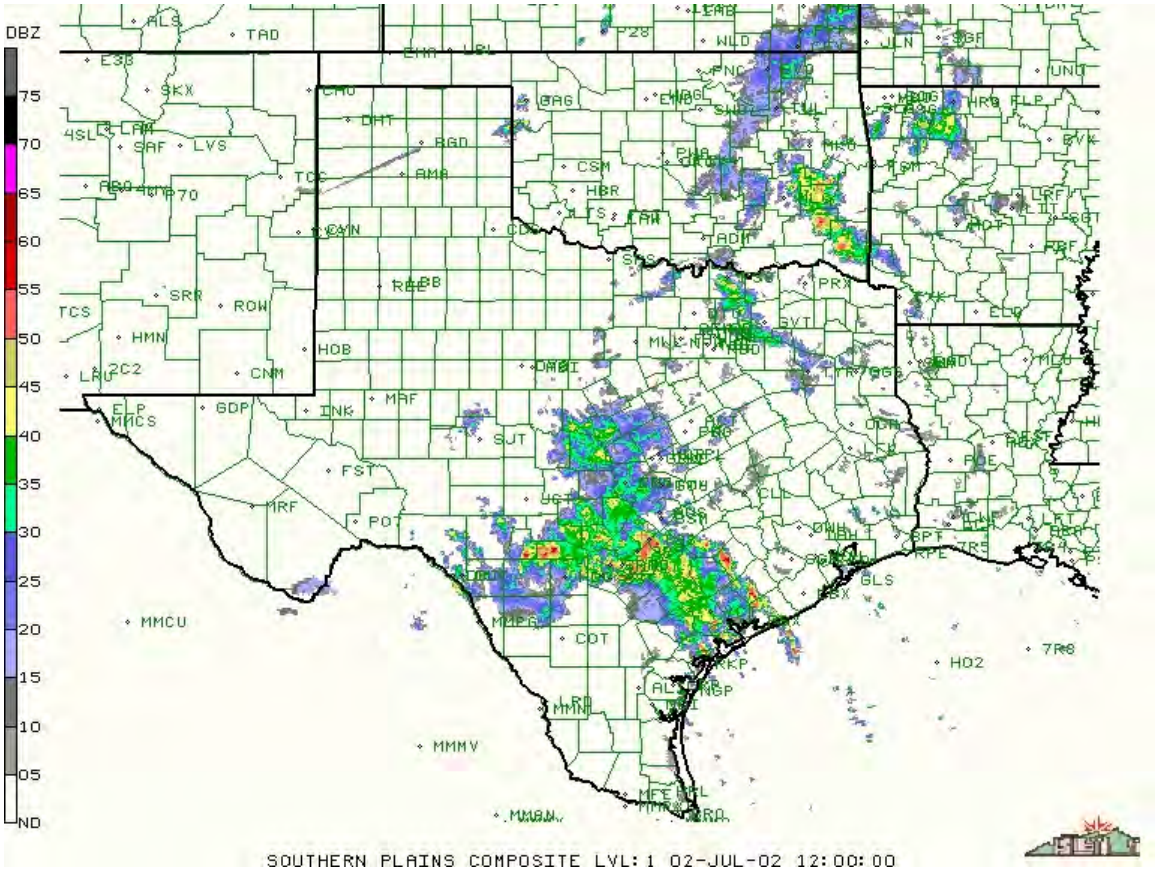

Fig. 2.20 Radar composite valid at 12Z 2 July.

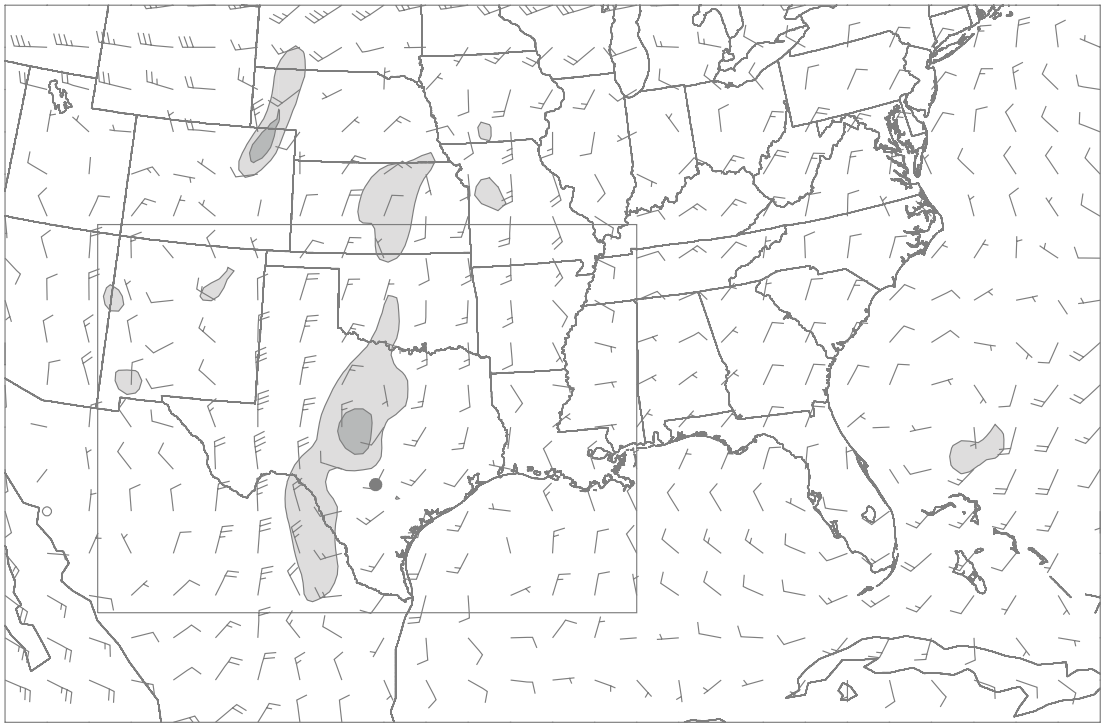

Fig. 2.21 Isentropic potential vorticity and wind speed at 320K as in Fig. 2.7, valid at 12Z 2 July.

continues to advect positive PV to the region; in addition, plentiful moisture and relatively high CAPE values help in the diabatic generation of stronger vortices.

The northern portion of the elongated PV anomaly has advected into southwest Colorado by 5 July at 12Z, but there continues to be diabatic generation of PV to the west of San Antonio, as convection is once again initiated (Fig. 2.22). The strong northerly winds in west Texas have diminished to less than 5 ms^{-1} by 6 July at 00Z and have shifted northwest, while the strong positive PV anomalies formerly in central Texas have advected to the northern portions of the state, aided by 15 to 30 ms^{-1} southerly winds (Fig. 2.23). Reduced winds, more vertical shear, and considerably less relative humidity are present in the NW-RH cross-section (not shown). The strongest convection is now prominent in northern Texas, with some diabatic intensification of PV (12Z 6 July), and this positive PV anomaly continues to advect north-northwest as winds in the center of it are between 10 and 15 ms^{-1} from the southeast. Convection is minimal on 00Z 6 July but intensifies well to the west and north of the San Antonio area by 12Z, coinciding with the positioning of the vortex (not shown).

To briefly summarize the factors contributing to the self-perpetuating mechanisms, and the extent and duration of the heavy rainfall across Texas, the first component is the upper-level positive PV anomaly over southern Texas that stems from remnants of a breaking Rossby wave. This positive PV, which then undergoes destruction, helps to establish a positive PV anomaly seen in a 320K isentropic analysis. Strong convection initiates over the Gulf of Mexico, just off the coast of Brownsville, and this helps to diabatically generate the PV in that area which advects towards the San

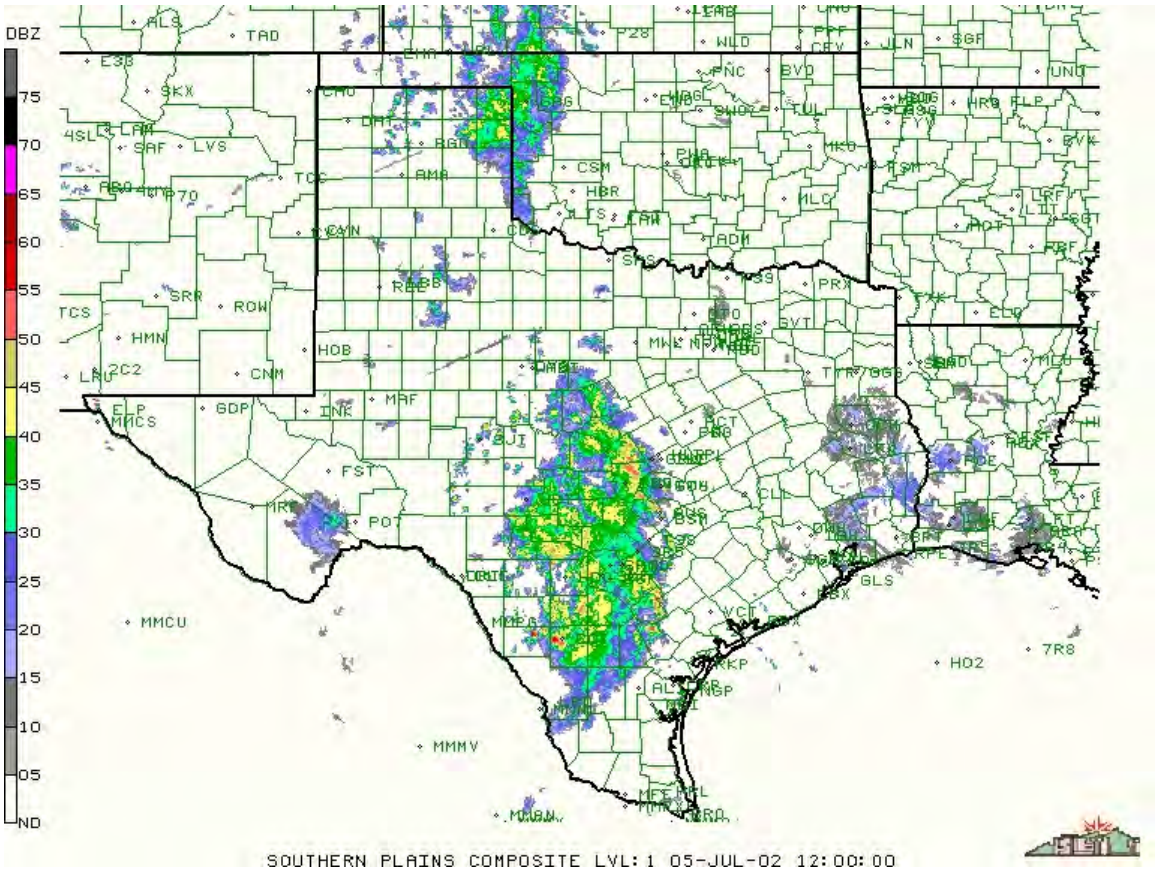

Fig. 2.22 Radar composite valid at 12Z 5 July.

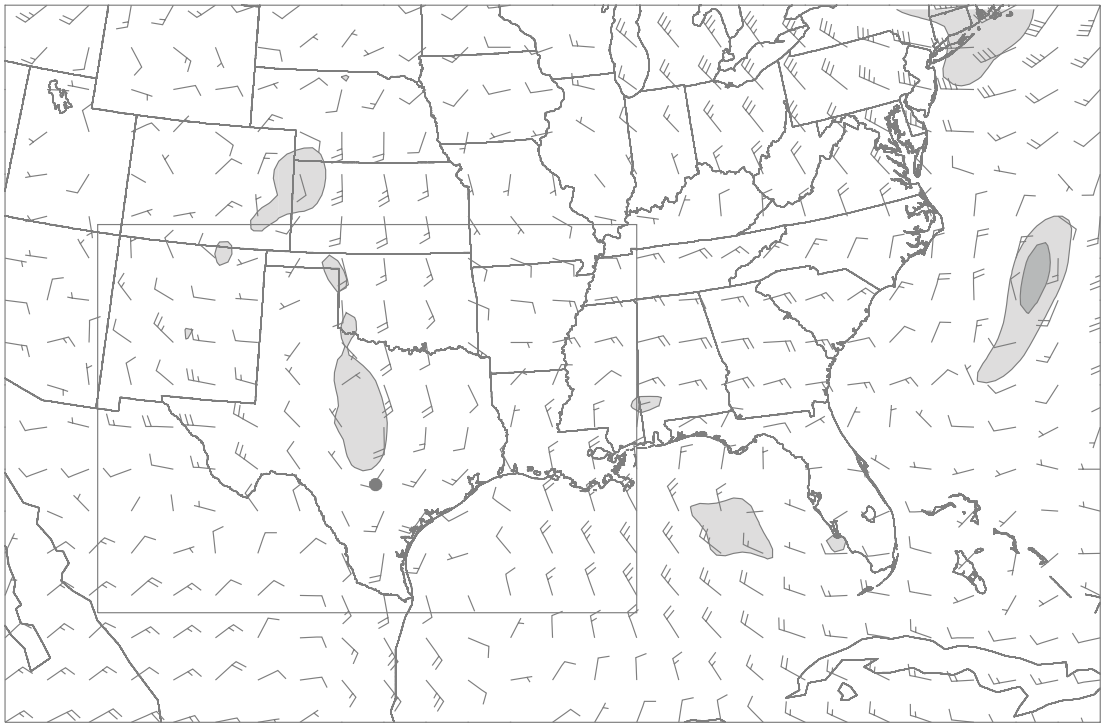

Fig. 2.23 Isentropic potential vorticity and wind speed at 320K as in Fig. 2.7, valid at 00Z 6 July.

Antonio area. Moist air is either advected or low-level moisture is lifted upward (due to stable upglide or convergence), helping to diabatically generate more positive PV. As the region remains convectively unstable, a strong MCS forms that keeps regenerating; the conditions for the regeneration include limited vertical shear, plentiful moisture, and the advection of positive PV from the return flow (westerly winds) at the southern-most end of the shear zone in south Texas. As the northern positive PV advects to the west, the well-defined elongated trough becomes less pronounced, therefore reducing advection of PV to the area.

2.3 Predictable versus non-predictable features

The previous section depicts many of the necessary ingredients that contribute to an extreme rainfall event. In order to forecast an extreme precipitation event, it is imperative to have an accurate forecast of all the elements. Some elements discussed in the previous section are more difficult to forecast using numerical weather prediction than others. The location of the large-scale features, such as the positive PV vortex seen in Fig. 2.4 are typically not difficult to predict. At the mesoscale, certain ingredients necessary for convection can be more difficult to predict, but some are not: ingredients that are not difficult to forecast include moisture content, broad areas of instability, and in this case the lifting mechanism. Such forcing (lifting mechanism) is often difficult to predict, however the localized forcing required to break the cap is not difficult to forecast.

The more difficult components to simulate properly includes the high rainfall rate and the evolution and duration of the event. In this case, the event lasted for nearly eight days, delivering copious amounts of rainfall as previously described. The research of ZSR03 found that model errors initiated at the mesoscale, then grew to affect the larger

scales in as little as 36 hours, under perfect model assumptions. Distinct individual convective cells can be difficult to predict, particularly in locations where the temperature of a parcel is at a threshold of being stable or convectively unstable. Therefore, it is of interest to examine the predictability of extreme precipitation events with respect to the uncertainties associated with rainfall distribution and intensity.

CHAPTER III

EXPERIMENTAL DESIGN

3.1 Forecast model, configuration, and data

For this investigation, the National Center for Atmospheric Research-The Pennsylvania State University (NCAR/PSU) nonhydrostatic fifth-generation Mesoscale Model (MM5) version 3.6 (Dudhia 1993) is employed. The coarse 30-km grid domain consists of 190 X 120 grid points with 23 vertical layers encompassing the contiguous United States, and northern portions of Mexico and the Gulf of Mexico. Finer-resolution simulations will utilize one or two nested domains (D2 and D3) with 10- and 3.3-km grid sizes, respectively. Both D2 and D3 employ a total of 241x181 horizontal grid points with two-way nesting, and the 3.3-km simulation will use 46 vertical layers; the domain locations can be seen in Fig. 3.1. The model is integrated for 36 hours, and the output is saved every 3 hours. Following several tests of physics parameterization combinations to most accurately represent the 36-hour forecasted 24-hour accumulated rainfall total, the following configuration is selected for the control experiment (CNTL30km). The Eta planetary boundary layer scheme (Mellor and Yamada 1981), the Reisner 2 (Reisner et al. 1998) microphysics scheme with graupel, and the Grell cumulus scheme are incorporated in CNTL30km. For the high resolution simulations, Reisner 1 microphysics, and the Grell cumulus scheme (Grell 1993) are used for D1 and D2, while D3 is fully explicit. The unperturbed control simulation incorporates GEWEX (Global Energy and Water Cycle Experiment) Continental-Scale International Project (GCIP) ETA model data with the Advanced

Fig. 3.1 The relative locations of MM5 model domains. The grid resolutions of D1, D2, and D3 are 30, 10, and 3.3 km, respectively.

Weather Interactive Processing System (AWIPS) Grid 212, which has a horizontal resolution of 40-km and grid dimensions of 185 X 129, and output is provided on 25 pressure surfaces (NCEP EMC, 2002).

3.2 A comparison with ZSR02 and ZSR03

The investigation into the predictability of the ‘02 Flood follows the research conducted in ZSR02 and ZSR03 closely. Several similarities exist between ZSR02 and ZSR03 and the present research, both from a weather point-of-view and with the experiment procedures employed. The fundamental similarities include that each event was extreme, and the operational models performed poorly at forecasting these two events, even as short as 36 hours. However, there are some notable differences between ZSR03 and this research. ZSR02 and ZSR03 focused on an extreme extratropical cold-season event in which heavy snowfall blanketed several areas along the eastern seaboard. The ‘02 Flood was a warm-season, subtropical event with stronger convective instability. In addition, heavy precipitation was much more localized and extended for a greater duration than with the “Surprise Snowstorm” of January 2000.

Experimental differences and similarities are also evident in this investigation. Since the mechanisms responsible for the catastrophic flooding in Texas were very localized, movable nested grids will not be utilized. The investigation into the practical forecast uncertainties will explore the same resolution dependence with the same domain sizes as ZSR02. However, in this study we will not use different data sources for the initial conditions, nor will we explore the sensitivity to individual soundings as was performed in ZSR02. The present research will investigate practical issues pertaining to different lead times, as well as changes to physics parameterizations (details to be

discussed in the next sub-section). For the intrinsic predictability studies, ZSR03 induced a monotonic perturbation in temperature across the grids, whereas the '02 Flood research will utilize random "grid-point" perturbations of temperature across the domain with a specified standard deviation (as used in Tan et al. 2003, hereafter TZRS04). This research will also diagnose error growth due to model resolution and varying the perturbation amplitude, and a "fake-dry" model run, similar to ZSR03, will be used. In addition studies of error growth stemming from different physics parameterizations, different days during the event (including diurnal variation), and different realizations (an ensemble of simulations with the same perturbation amplitude) will also be performed. The intrinsic predictability results will use the same DTE and spectrum analysis methodologies as ZSR03, as well as graphical difference fields. A comparison of the results between the studies of ZSR02 and ZSR03 with the '02 Flood will be addressed in the appropriate chapters.

3.3 Experimental design

Table 1. List of practical predictability experiments and details regarding each of the studies.

Name	Grid Size	Initial Time	CPS	PBL	Microphysis
CNTL30km	30 km	00Z 1 July	Grell	ETA	Reisner 2
LEAD24hr	30 km	*12Z 1 July*	Grell	ETA	Reisner 2
LEAD48hr	30 km	*12Z 30 June*	Grell	ETA	Reisner 2
HIGH30km	30 km	00Z 1 July	Grell	ETA	*Reisner 1*
HIGH10km	*10 km*	00Z 1 July	Grell	ETA	*Reisner 1*
HIGH3.3km	*3.3 km*	00Z 1 July	Grell	ETA	*Reisner 1*
CPS-KF	30 km	00Z 1 July	*Kain-Fritsch*	ETA	Reisner 2
NoCPS	30 km	00Z 1 July	*None*	ETA	Reisner 2
EXP-GD	30 km	00Z 1 July	Grell	ETA	*Goddard*
EXP-SI	30 km	00Z 1 July	Grell	ETA	*Simple Ice*
PBL-MRF	30 km	00Z 1 July	Grell	*MRF*	Reisner 2
PBL-HIR	30 km	00Z 1 July	Grell	*Blackadar*	Reisner 2

A series of experiments have been formulated to examine both intrinsic and practical mesoscale predictability of the ‘02 Flood. A concise list of the experiments utilized in this research is found in Tables 1 and 2 with details to follow.

Table 1 shows the experiments conducted to investigate practical predictability. First, the control simulation will be compared with the observational analysis to examine any differences. Next, simulations with different lead times to include initializations at 12Z 30 June and 12Z 1 July, along with the CNTL30km, will be performed. These simulations will be used to generate the 24-hour total precipitation valid at 12Z 2 July, with the forecast lead-time of 24-, 36-, and 48-hr, respectively (LEAD24hr and LEAD48hr). Then the value of the forecast, essentially the quality of the forecast with respect to the proximity, aerial coverage, and total rainfall, will be examined. The next set of experiments will look into resolution dependence of the model forecast by performing nested simulations at 10-km and at 3.3-km (HIGH10km and HIGH3.3km). A 36-hour forecast run initialized at 00Z 1 July will be performed for each of the respective resolutions. A simpler version of the Reisner microphysics scheme was utilized which does not include graupel; this scheme was used due to computer memory constraints in the HIGH3.3km.

The last group of experiments exploring practical predictability includes changes in the physics parameterizations. Recall that CNTL30km incorporated the Grell cumulus, ETA planetary boundary layer (PBL), and the Reisner 2 microphysics schemes (Grell-ETA-R2); a single change in one of the parameterizations will be made to explore the effects of cumulus, PBL, and microphysics on a 36-hour simulation that is initialized at 00Z 1 July. Changes to the cumulus schemes include using the Kain-Fritsch (CPS-KF)

and no cumulus parameterization scheme (NoCPS); for the PBL, changes will include using the MRF and the Blackadar (PBL-HIR); lastly, the microphysics options will be changed to the Goddard microphysics scheme (EXP-GD) and simple ice (EXP-SI). Again, the 24-hour accumulated rainfall forecast valid at 12Z 2 July will be compared with the analysis, and a qualitative description and assessment of the value of the simulation will follow.

Table 2. List of intrinsic predictability experiments and details regarding each of the studies.

Experiment	Details
PERT30km	Same as CNTL30km, but with perturbation amplitude of 0.2
Resolution Dependence (PERT3.3km)	3.3-km simulation with perturbation amplitude of 0.2
Varying Perturbation Magnitude	Incorporates perturbation amplitudes of 0.002K, 0.02K, 0.4K, 1.0K, 2.0K
Realization	Five separate simulations with perturbation amplitude of 0.2
Different Days/Diurnal Variation	Unperturbed and perturbed simulation, amplitude of 0.2, initialized at 00Z and 12Z for each day from 28 June through 5 July
Moist Convection	Unperturbed and perturbed simulation, amplitude of 0.2, for each of the physics parameterizations listed above, and a "Fake-Dry" simulation

Table 2 summarizes the experiments conducted to examine intrinsic predictability. Using “grid-point” random temperature perturbations (TZRS04), with a specified standard deviation added to all the model grid points, an attempt will be made to assess the rate of error growth and the forecast period of maximum growth rate. These perturbations are induced to the initial conditions of the 30 kilometer coarse grid for all simulations. Since atmospheric variables are often at “critical” points, the induction of a very small temperature perturbation can yield a rapid error growth in the early forecast period (ZSR03). The control perturbation simulation (PERT30km) utilizes a standard deviation of 0.2K added to the initial conditions of the horizontal temperature field at all model grid points.

The next experiment will involve the same random grid-point perturbation amplitude (0.2K) to the 30 kilometer domain, but will be interpolated to the 3.3-km high resolution domain, initializing at 00Z 1 July. Comparison between the control and perturbed simulation will follow by exploring the rate of error growth throughout the forecast period. ZSR03 found that in the higher resolution simulation, the errors grew at a faster rate early in the forecast period, coinciding with Lorenz's (1963) theory of the finite limit of predictability. If given perfect initial conditions, even incorporated in higher resolution simulations, forecast divergence will still occur, as shown in ZSR03. Further discussion of this will follow in the subsequent chapters.

The next set of experiments will be to create an ensemble of simulations varying the perturbation amplitude. The random grid-point perturbation standard deviation will be changed from the control of 0.2K to 0.002K, 0.02K, 0.4K, 1.0K, and 2.0K. ZSR03 found that errors grew at a faster rate early in the forecast period with lower perturbation amplitudes, and that a saturation of error growth took place near the end of the forecast simulation, again showing that Lorenz's (1963) theory of limits of predictability holds true. A second set of experiments will include another ensemble set utilizing the control perturbation amplitude. Five separate simulations with a random grid-point perturbation of 0.2K will be performed to investigate different realizations of the same perturbation amplitude; this will check if the evolution of error growth changes substantially given the same perturbation magnitude but a different realization.

To explore the behavior of the error growth throughout the '02 Flood, the control perturbation amplitude of 0.2K will be induced to each grid point of the unperturbed simulations every 12 hours throughout the storm duration. Beginning at 00Z on 29 June

and extending through 12Z on 5 July, the initial conditions for each day at 00Z and 12Z will be perturbed and a 36-hour forecast will be generated. There are two purposes behind this: first, this experiment aims to determine if there is a significant outlier of error growth for any particular day throughout the event. Second, this will also determine any significant changes of the error growth diurnally.

The last group of experiments will involve inducing the control perturbation amplitude of 0.2K to each of the unperturbed simulations with the different physics parameterizations as detailed previously in this section. This experiment will ensure that error growth is not susceptible to one type of convective parameterization. Included will be a "fake-dry" simulation, in which latent heat will be turned off. ZSR03 found that moist convection was the primary source of the initial rapid error growth. In their experiments, the "fake-dry" simulation showed a substantially reduced error growth throughout the forecast duration, and this is expected with the '02 Flood.

To quantify the error growth, the difference total energy (DTE) per unit mass will be calculated and is defined by:

$$DTE = \tfrac{1}{2} \Sigma \left(U_{ijk}'^2 + V_{ijk}'^2 + \kappa(T_{ijk}')^2\right)$$

where U′, V′, and T′ are the difference of wind components and temperature respectively, $\kappa = C_p/T_{ref}$, where C_p is the specific heat at constant pressure (equal to 1004 J deg^{-1} kg^{-1}), T_{ref} equals 270K, and i, j, and k run over x, y, and σ grid points (ZSR03 and references therein). The DTE will be utilized to determine the evolution of error growth versus time and will also show the error growth versus wavelength in the form of a spectrum analysis.

CHAPTER IV

PRACTICAL PREDICTABILITY

This chapter examines the results of the practical predictability experiments of the ‘02 Flood. Practical predictability seeks to explore the real-time forecast difficulties and begins to look at the nature of error growth. Recall from Chapter I that practical predictability, utilizing a numerical weather prediction model, is the ability to forecast based on current procedures, that includes the model imperfections and uncertainties in initial conditions (Lorenz 1996). To examine practical predictability, the experiments begin by investigating the development of forecast divergence resulting from common deficiencies in the numerical weather forecast including: model errors stemming from different forecast lead times (initial condition errors), different physics parameterizations, and different model resolution (model errors). First, a control simulation will be established; it will be assumed that this simulation will stem from a perfect model. Then, the experiments as detailed in Chapter III will be conducted. The limit of intrinsic predictability under the assumption of a perfect model will be discussed in Chapter V.

4.1 Control simulation

As previously stated in section 2.1, the ‘02 Flood began on 29 June and lasted through 6 July. There were several days throughout this period that heavy rainfall was experienced; since San Antonio is the major metropolitan closest to the area that received the greatest amount of rain, it will therefore be the reference point used throughout this investigation. One of the days of heaviest precipitation was 2 July (recall from the previous chapter that this period extends from 12Z 1 July through 12Z 2 July), and this is

also the period when San Antonio experienced its heaviest rainfall, 8.79 inches (223 mm). Therefore, this research will be centered on this day. Both practical and intrinsic predictability experiments will be conducted for each day throughout the event as well.

Tests were conducted included varying the boundary layer scheme, microphysics options, and the cumulus options. Details regarding the methods and parameter changes are presented in section 3.3 (refer to Table 1 for the physics parameterization schemes that were used). The control simulation is initialized at 00Z 1 July and run over the coarse 30-km grid. This model run has a simulation time of 36 hours and is denoted as CNTL30km. Referring back to Fig. 2.1d, also seen in Fig. 4.1a, the 24-hour accumulated precipitation analysis for 2 July is depicted. Fig. 4.1b shows the simulated forecast of 24-hour accumulated precipitation for the 36-hour forecast. The model forecast performs reasonably well compared to the analysis, showing good representation of the total accumulated precipitation, as well as the proximity and spatial extent of rainfall near San Antonio. The discrepancies include the unverified precipitation located near the College Station area, as well as the rainfall east of Amarillo. A comparison between the 320K isentropic 36-hour forecast (Fig. 4.2a) with the 320K analysis (from Chapter II, now shown in Fig. 4.2b) shows a long finger of positive PV stretching from southern Nebraska into Mexico that extends farther into Mexico than in the analysis, and it is tilted more in a southwest to northeast orientation. The forecast depicts an elongated trough extending into southern Nebraska very much like the analysis, but it does not show the positive PV advecting toward San Antonio as shown to be the case in the analysis (Fig 4.2a). The analysis indicates stronger and more northerly winds in west Texas, the

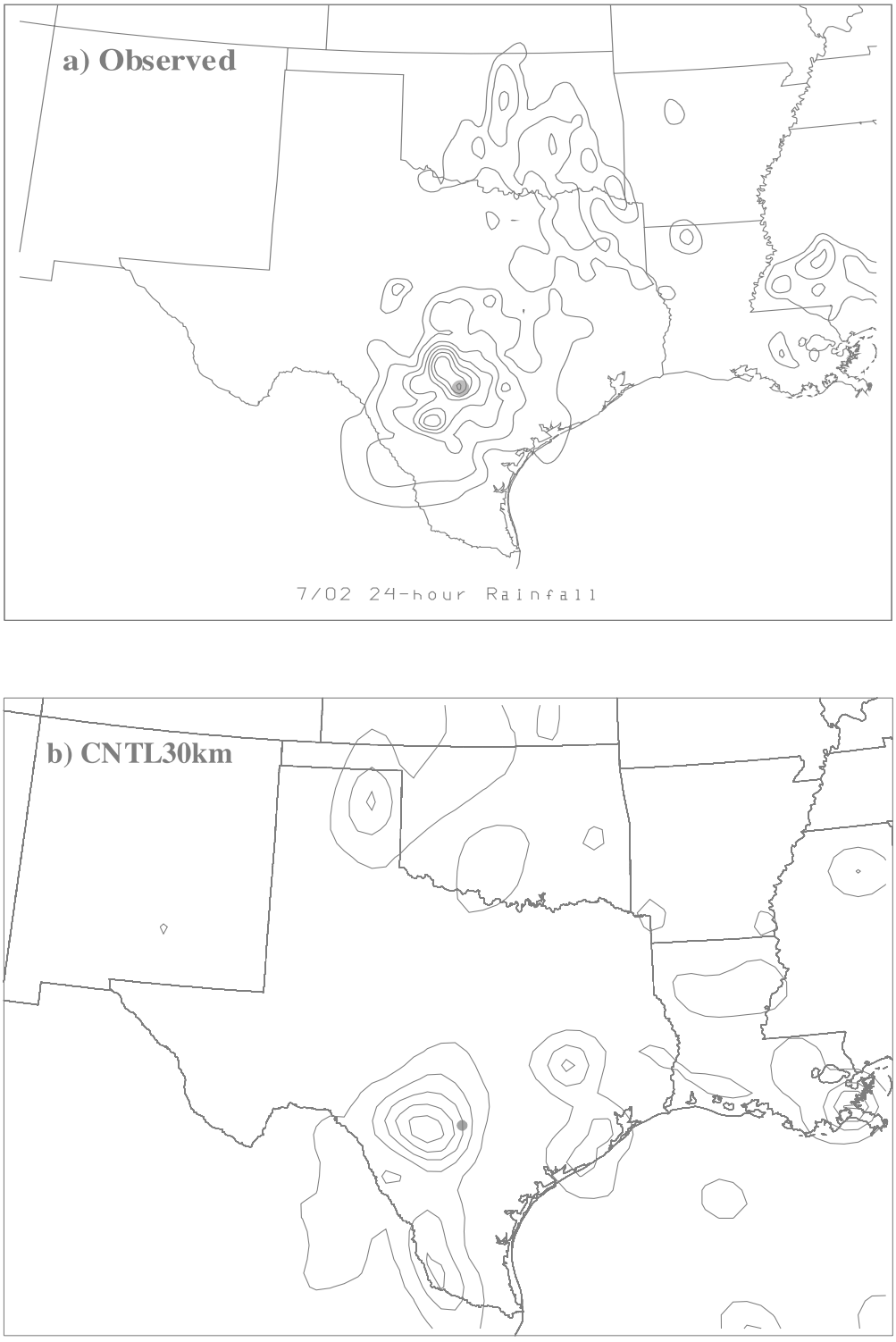

Fig. 4.1 24-hour accumulated precipitation at 12Z 2 July (contours every 20 mm, beginning at a 10mm contour) (a) observed; (b) CNTL30km.

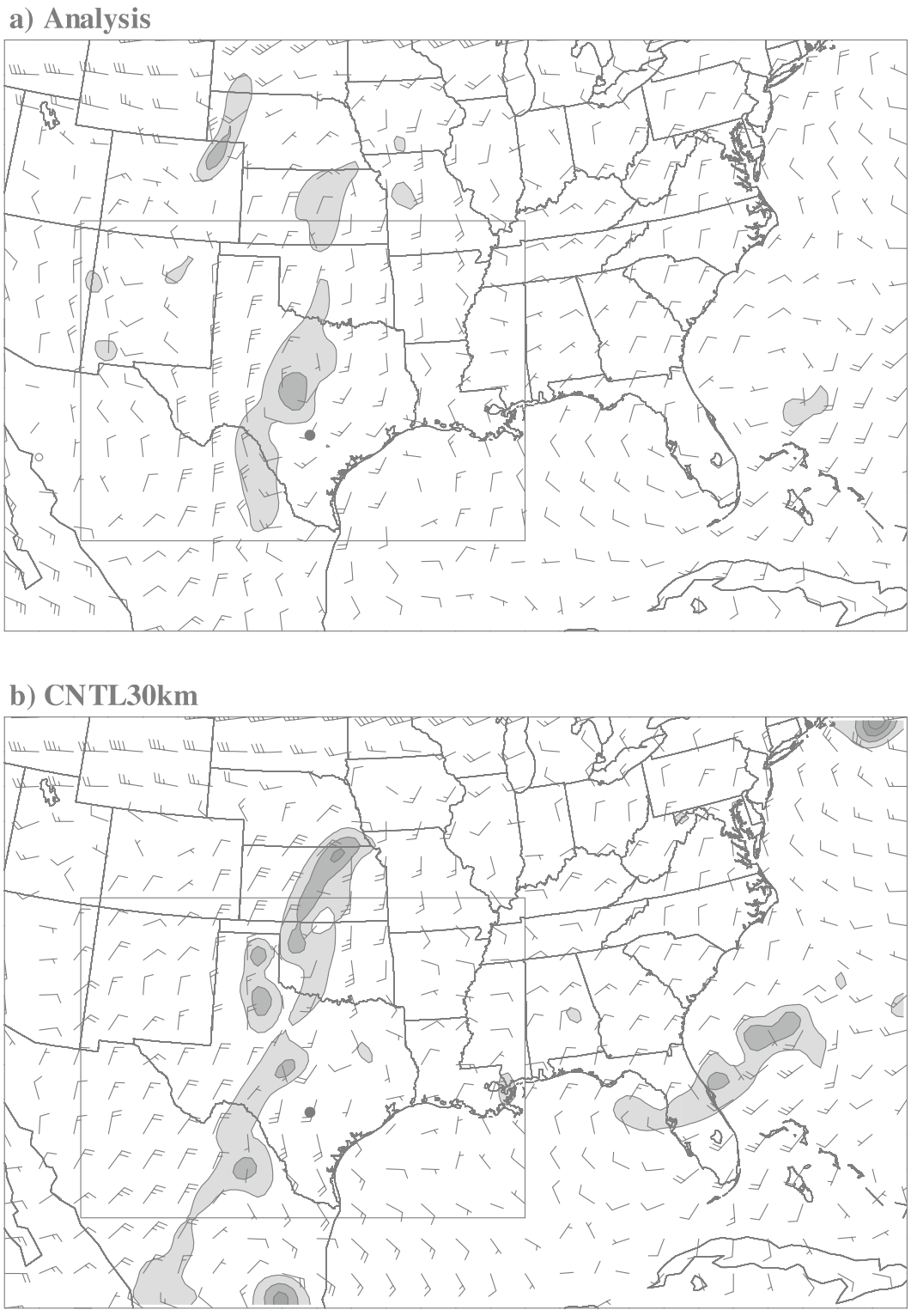

Fig. 4.2 Isentropic potential vorticity at 320K (shading, every 0.5 PVU) and wind vectors (full barb denotes 5 ms^{-1}) (a) Analysis; (b) CNTL30km.

positive PV anomaly is closer to San Antonio, and there is also a more notable shear zone in the analysis compared to the forecast (Fig. 4.2b). Certainly the precipitation forecast performed well, and the isentropic forecast did a good job overall with some minor discrepancies.

4.2 The 30-km control simulation with different lead times

This section will begin exploring practical predictability by comparing the forecast with different lead times; limited lead-time-forecast accuracy is also subject to intrinsic predictability, which will be discussed in the subsequent chapter. Typically as the forecast time extends, the accuracy of the simulation is reduced; thus the accuracy between forecasts with lead times of 24, 36, and 48 hours (LEAD24hr, CNTL30km, and LEAD48), respectively will be compared.

The 24-hour accumulated precipitation forecast is compared with the 24-hour observed accumulated rainfall for 2 July in Fig. 4.3 (recall from Chapter II that the 24-hour precipitation total for a given day extends from 12Z on the previous day to 12Z on the current day being described). From the previous section, the control forecast (CNTL30km) is initiated at 2002 July 1 at 00Z, and the 36-hour forecast time is shown in Fig. 4.3c. Also shown is the 24-hour forecast initiated at 2002 July 1 at 12Z (Fig. 4.3b), and the 48-hour forecast initiated at 2002 June 30 at 12Z (Fig. 4.3d). As the forecast time extends beyond 36 hours, the accuracy, particularly of the total rainfall, diminishes significantly. Fig. 4.3b is a rather good forecast, showing good representation of both the rainfall totals and the areal coverage, however there is an overproduction of the heaviest rainfall of 100 mm. Although the greatest precipitation is forecasted to be more south and west, the overall simulation is very good. By the 36-hour forecast (Fig. 4.3c), there

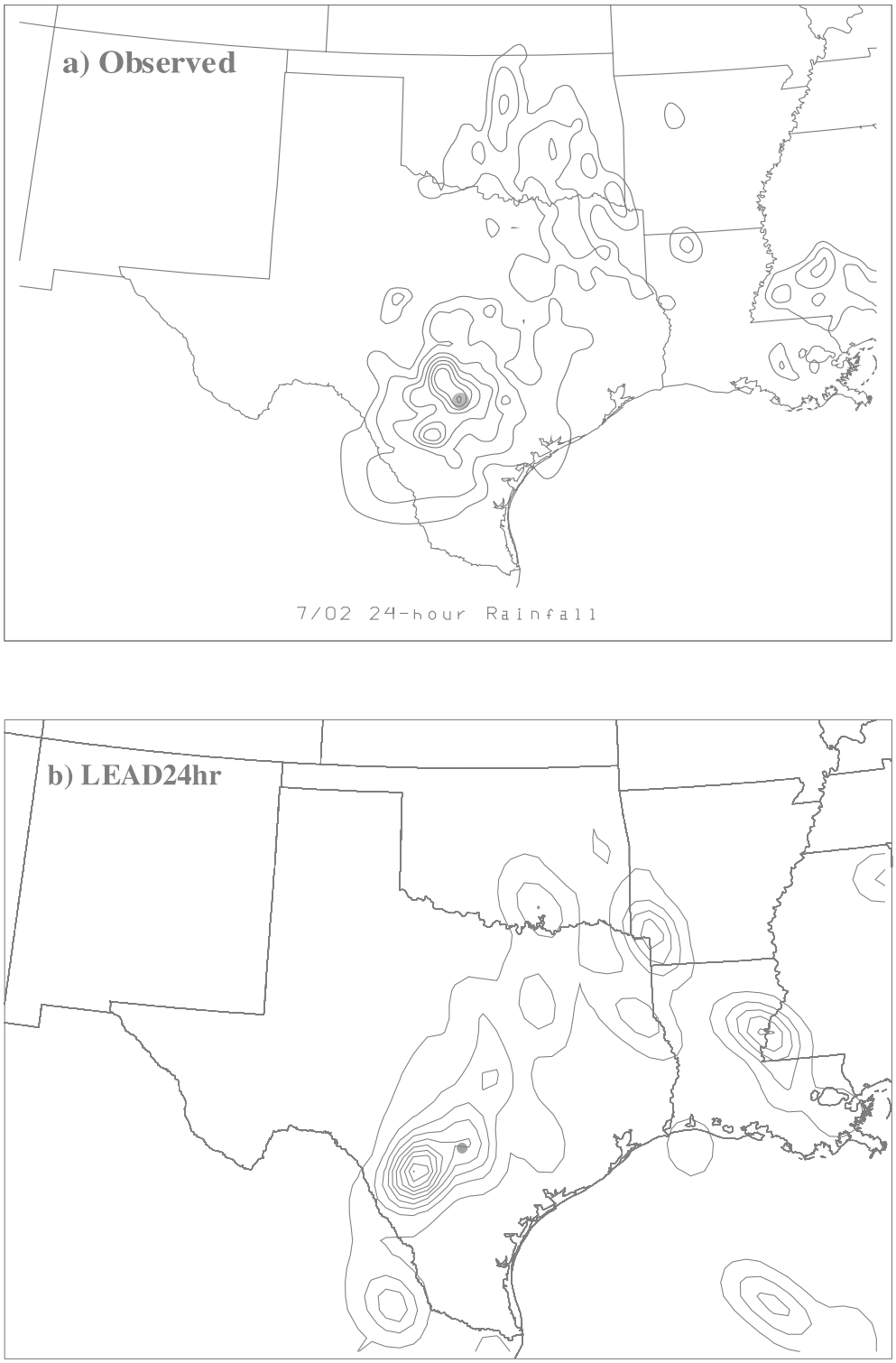

Fig. 4.3 24-hour accumulated precipitation at 12Z 2 July, contours as in Fig. 4.1, (a) Analysis; (b) LEAD24hr; (c) CNTL30km; (d) LEAD48hr.

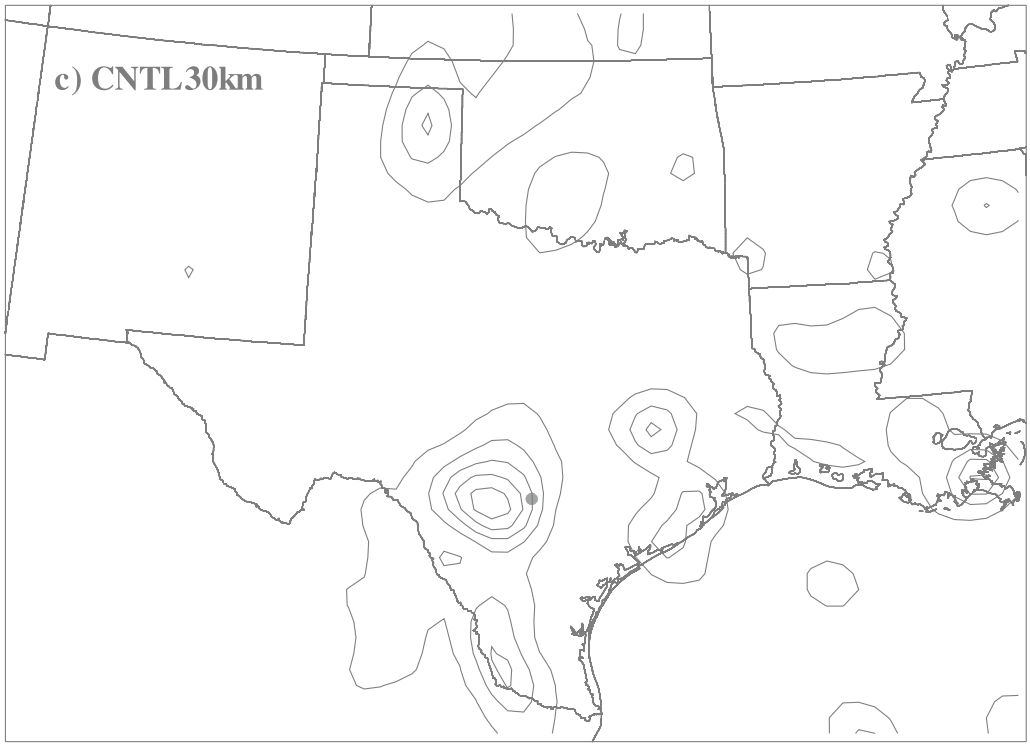

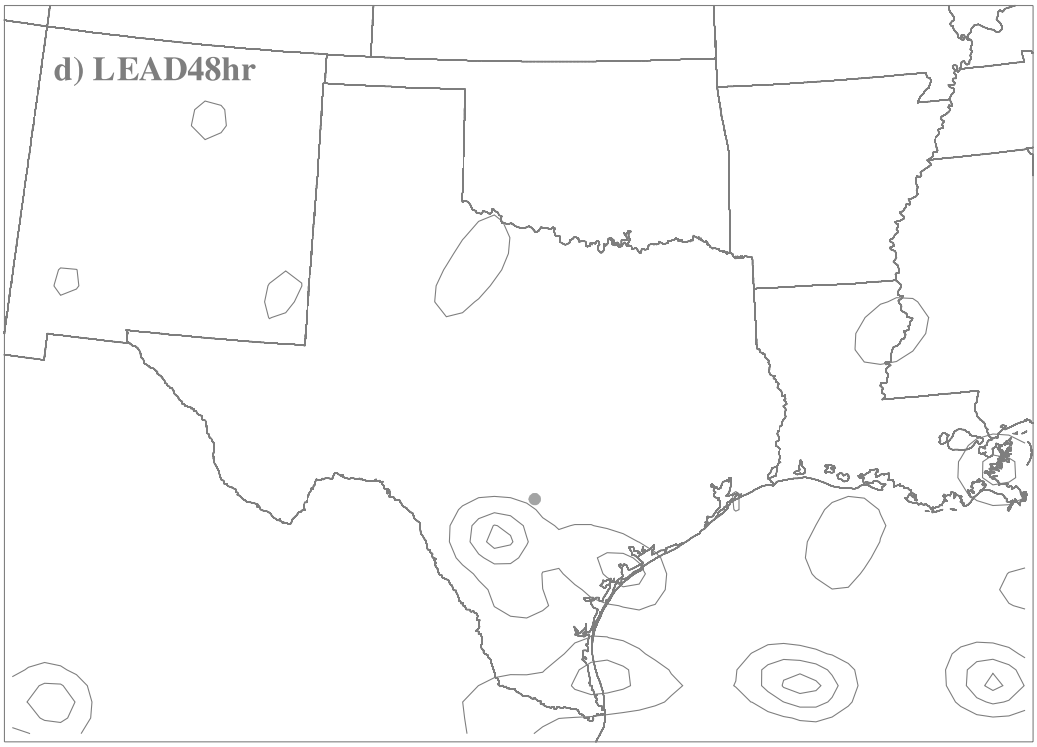

Fig. 4.3 continued.

is a substantial reduction in the total precipitation to a 120 mm maximum, which correlates well with the observational analysis; the proximity and general coverage is also very good. The 48-hour simulation has dramatically reduced the total precipitation quantity and coverage (Fig. 4.3d). It would be reasonable to forecast scattered showers with perhaps some heavy precipitation south and west of San Antonio; as for the 24-hour lead time forecast, one could say that there is a reasonable likelihood of heavy precipitation west of and including the San Antonio area.

To further explore practical predictability with different lead times, the following examines the PV features, which has been shown in Chapter II to be important in the generation of the heavy precipitation. Fig. 4.4 shows the 320K isentropic forecast of PV for each of the above-mentioned lead-times, with Fig. 4.4a depicting the observational analysis used in section 2.2. Fig. 4.4b shows the 24-hour forecast, which depicts strong north-northwest winds in west Texas resulting from high pressure in the western United States, and strong southerly winds in central Texas. The strong positive PV anomaly is also present near San Antonio, was produced by the heavy rain forecasted in Fig. 4.3b, and resembles the analysis well. The 36-hour forecast (Fig. 4.4c) has been diagnosed in section 3.2. Fig. 4.4d shows southerly winds at the Big Bend area of Texas, a weak shear zone in northern Texas in a southwest to northeast orientation, and very slight positive PV near the San Antonio area. There does appear to be diabatic generation of PV near Laredo, Texas, but this would be advected toward Mexico and not San Antonio. Very similar to the precipitation forecasts from above, as the simulation lead time extends beyond the 36 hour forecast time, there is a substantial reduction in the accuracy of the forecast outcome.

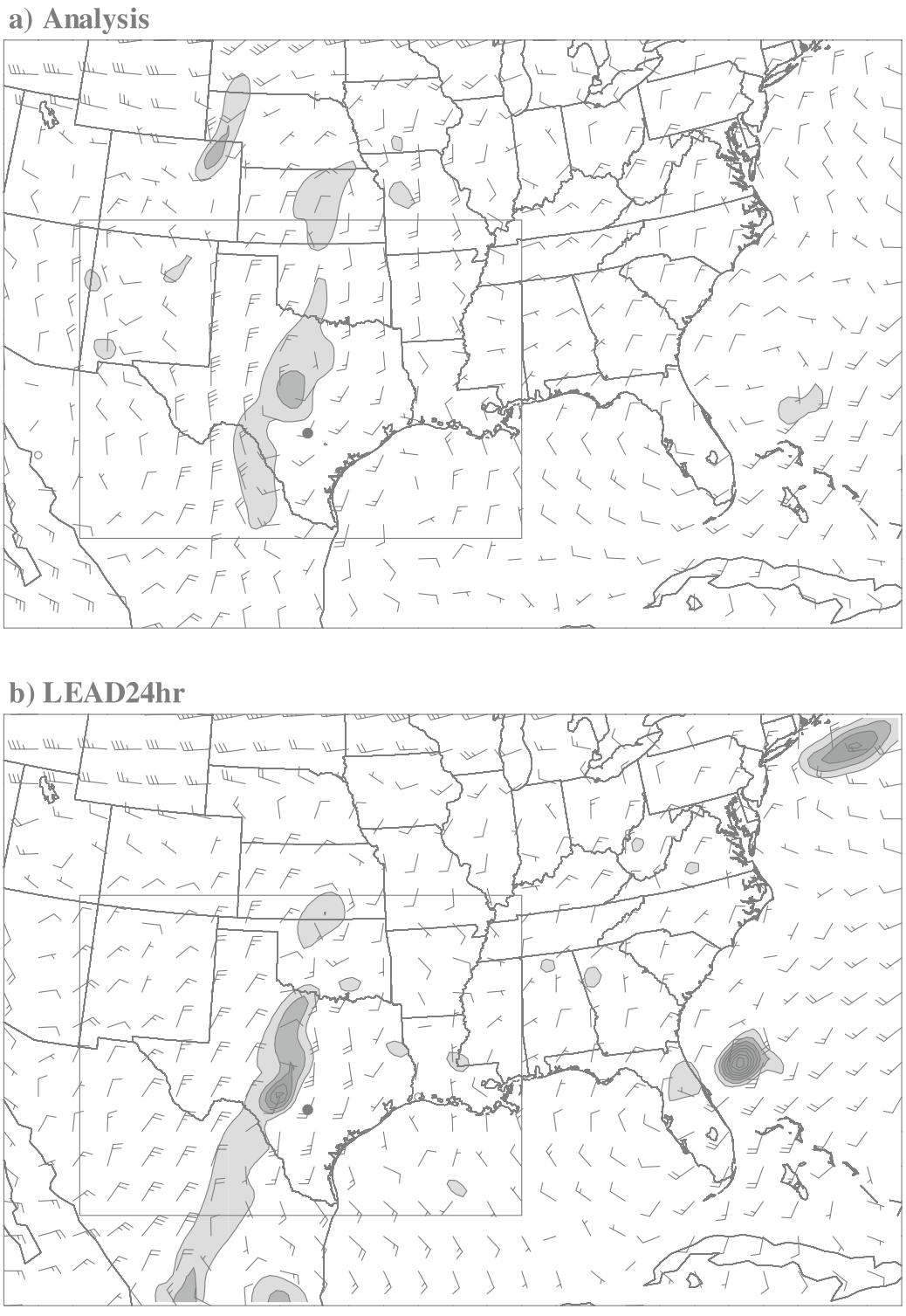

Fig. 4.4 Isentropic potential vorticity at 320K, as in Fig. 4.2, (a) Analysis; (b) LEAD24hr; (c) CNTL30km; (d) LEAD48hr

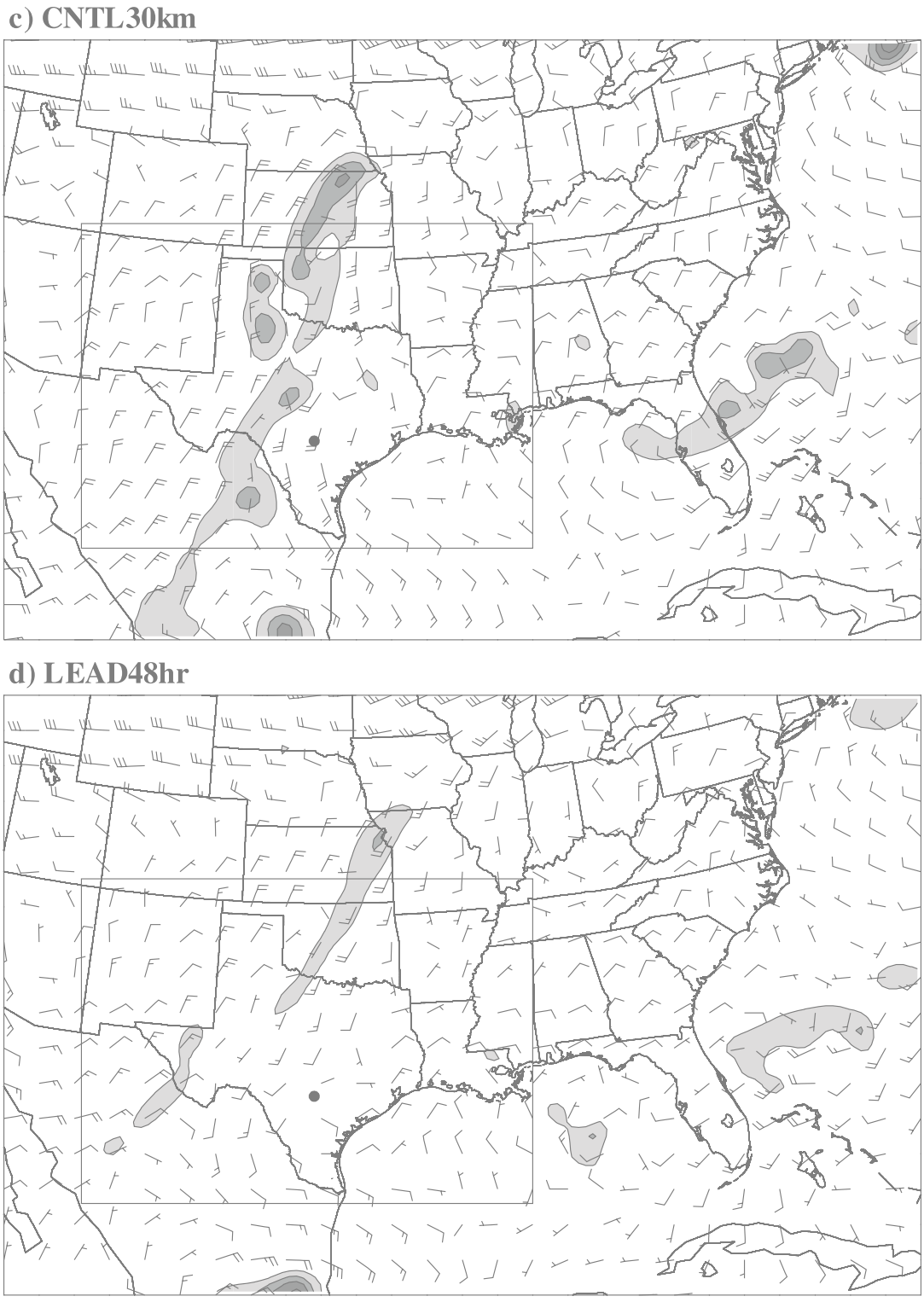

Fig. 4.4 Continued.

It has been shown that as the simulation time increases, there is a much reduced accuracy of the forecast. The rather good forecast provided by the 24-hour lead time (as compared to the observational analysis) may indicate that the event has a 24-hour predictable time scale. This raises the question of why there is such forecast divergence between 36- and 48-hour simulations compared to the 24- and 36-hour simulations. One possibility could be due to intrinsic limits, in that forecast errors grow rapidly at small scales, which will be explored more thoroughly in Chapter V. Another likely possibility is that the 24- or 36-hr lead-time forecasts could be solutions out of many possible realizations that happens to be the closest to the truth (observational analysis). This will be examined further with the sensitivity analysis to different physics parameterizations. In principle, error growth due to both practical and intrinsic aspects of predictability can lead to diminishing forecast accuracy as the lead time increases. Further discussion of the forecast value will be addressed in Section 4.4.

4.3 Sensitivity to model resolution

ZSR02 explored the impacts of higher resolution simulations in an extreme precipitation event, albeit a winter event. They found that resolution improved the forecast by more accurately resolving moist processes, thus leading to more detailed mesoscale features. The greatest improvement was made between the 30-km and 10-km simulations, with much reduced improvements in the 3.3-km model run. Nonetheless, they speculated that improved model resolution has the tendency to yield better forecast accuracy, particularly for discrete mesoscale features (ZSR02 and references therein).

Similar to ZSR02 with respect to grid sizes of 30-, 10-, and 3.3-km respectively, experiments were conducted to determine if improvements in the forecast quality will be

established if the model resolution was increased for the ‘02 Flood. Two-way nesting has been performed for the high resolution runs (domain sizes of 10 and 3.3 km). Fig. 4.5 shows the 24-hour accumulative precipitation at the 36-hour forecast for each domain, compared with the observational analysis. HIGH30km is very similar to CNTL30km with respect to the overall proximity of the rainfall, however there is a reduction in the intensity. HIGH10km (Fig. 4.5c), surprisingly shows a significant reduction in the precipitation quantity, and the coverage across the domain is also substantially reduced, which would result in a forecast for San Antonio to have very light rainfall. The areal coverage is further reduced, and the precipitation quantity over the primary flooding region has been reduced to nearly zero in the HIGH3.3km, as shown in Fig. 4.5d. A forecast based on this simulation would indicate a slight to no chance of precipitation over San Antonio.

It has been shown in this case that as the resolution increases, the accuracy of the forecast has diminished. This is in complete contrast with the findings of ZSR02, where improvements were made, particularly of the mesoscale features. There are a number of possibilities one could speculate as the reason for the poor performance. Firstly, the data points may be too coarse to resolve intricate mesoscale features in such resolutions. Secondly, as discussed in ZSR03, small errors grow faster at higher-resolutions, thus intrinsic implications may play a significant role and will be examined in Chapter V. This would potentially imply that the threshold of convective instability is not reached at many of the grid points, or it is achieved at others, and small perturbations may yield a significantly different forecast. ZSR02 established that sensitivity of the forecast is based on, “the initial conditions that are within the uncertainty of the operational analysis”

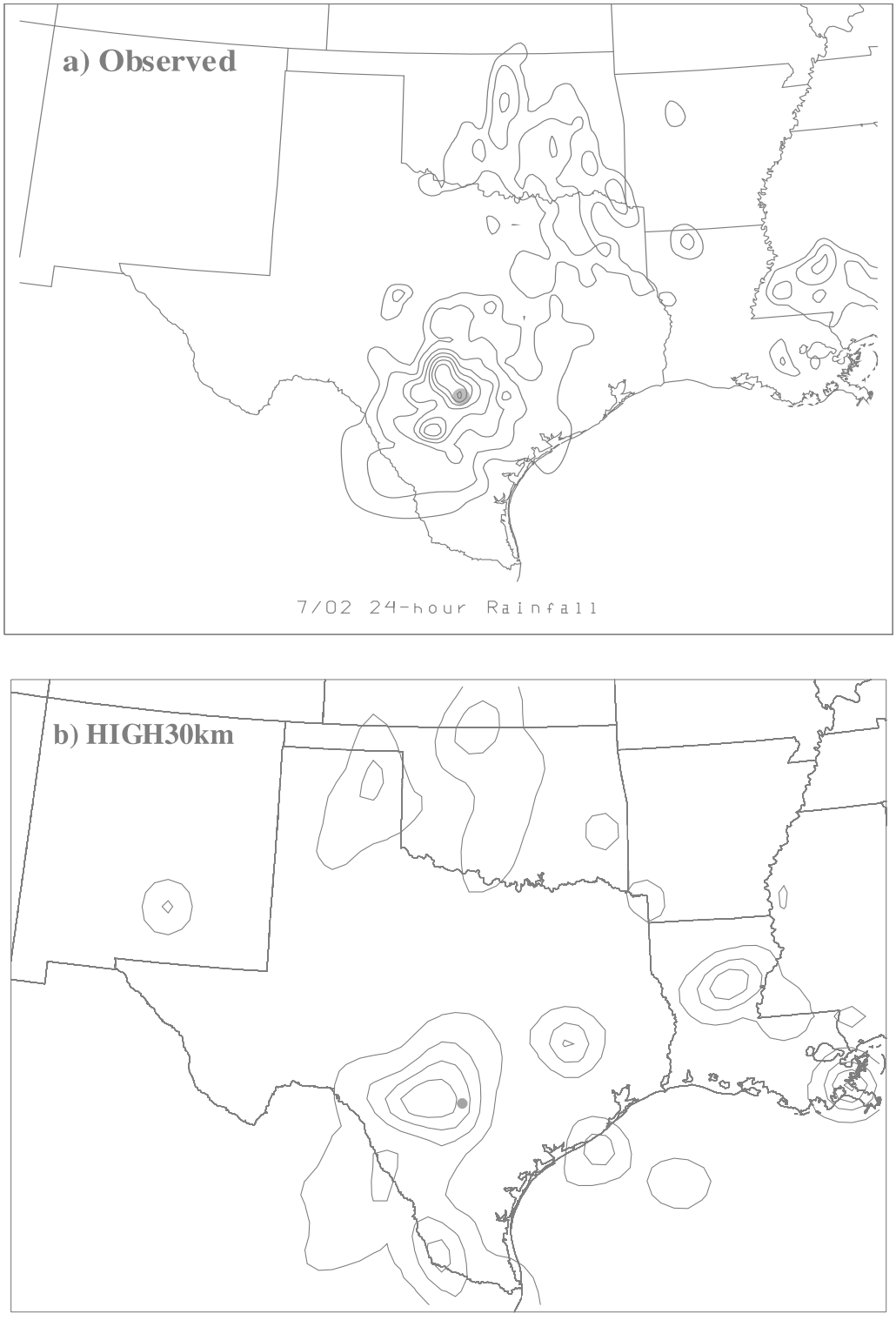

Fig. 4.5 24-hour accumulated precipitation at 12Z 2 July, contours as in Fig. 4.1, (a) Observed; (b) HIGH30km; (c) HIGH10km; (d) HIGH3.3km.

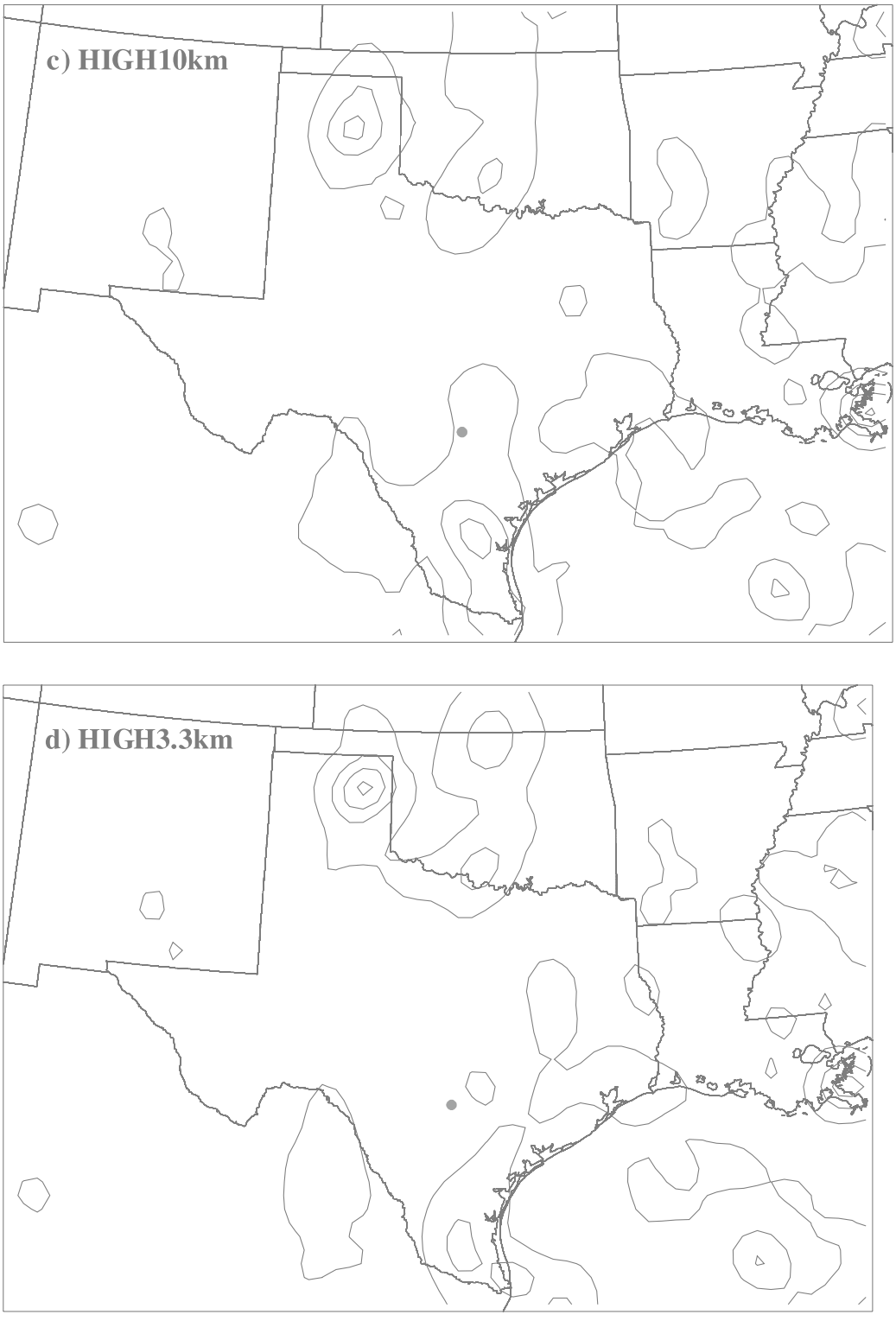

Fig. 4.5 Continued.

(ZSR02). It is also plausible that for such a high resolution simulation, other combinations of physical parameterization schemes may have performed better, but this would require further investigation.

4.4 Sensitivity to physics parameterizations

Another limit of practical predictability is due to errors in the forecast model itself, and a specific source of such limitations stems from the physical parameterization schemes. This section attempts to examine forecast sensitivity to model errors by varying the physics parameterization schemes within MM5. Recalling from Chapter III and referring back to Table 1, a single parameterization scheme will be changed, then a simulation will be conducted to compare the results from changes to cumulus, microphysics, and PBL schemes with respect to CNTL30km.

The first set of experiments involved changing the cumulus scheme from Grell to Kain-Fritch (CPS-KF), then another simulation using no cumulus scheme was tested (NoCPS). The Kain-Fritsch (KF) parameterization incorporates rather sophisticated physics, including cloud-mixing for entrainment and detrainment (Kain and Fritsch, 1993), and it has been shown to be rather successful in several previous case studies by generating results that were very comparable to observations (Wang and Seaman, 1996, Gallus and Segal, 2000). Fig. 4.6a shows the 24-hour precipitation accumulation for the control time of the observations (2002 July 2 at 12Z), and the 36-hour forecast for CNTL30km (Fig. 4.6b), CPS-KF (Fig. 4.6c), and NoCPS (Fig. 4.6d). The NoCPS simulation performed quite well, with regards to the proximity and accumulated precipitation, and it is quite similar to CNTL30km, including the erroneous forecast of rain at the Texas-Oklahoma Panhandles. The CPS-KF, however, performed quite poorly:

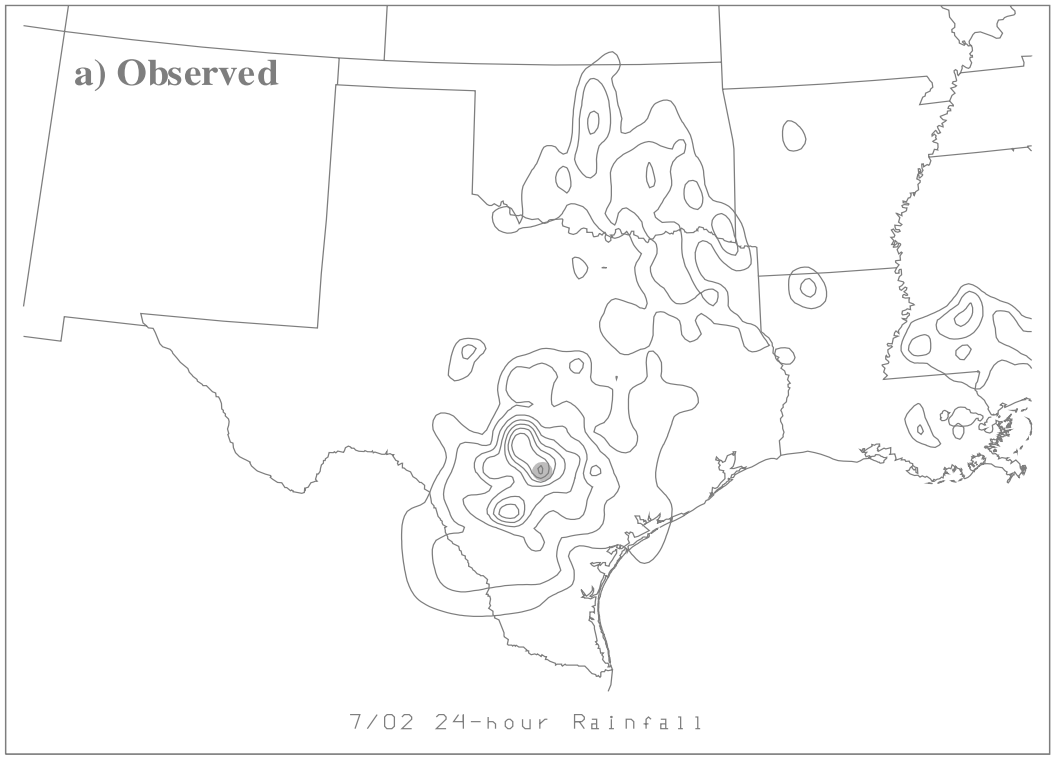

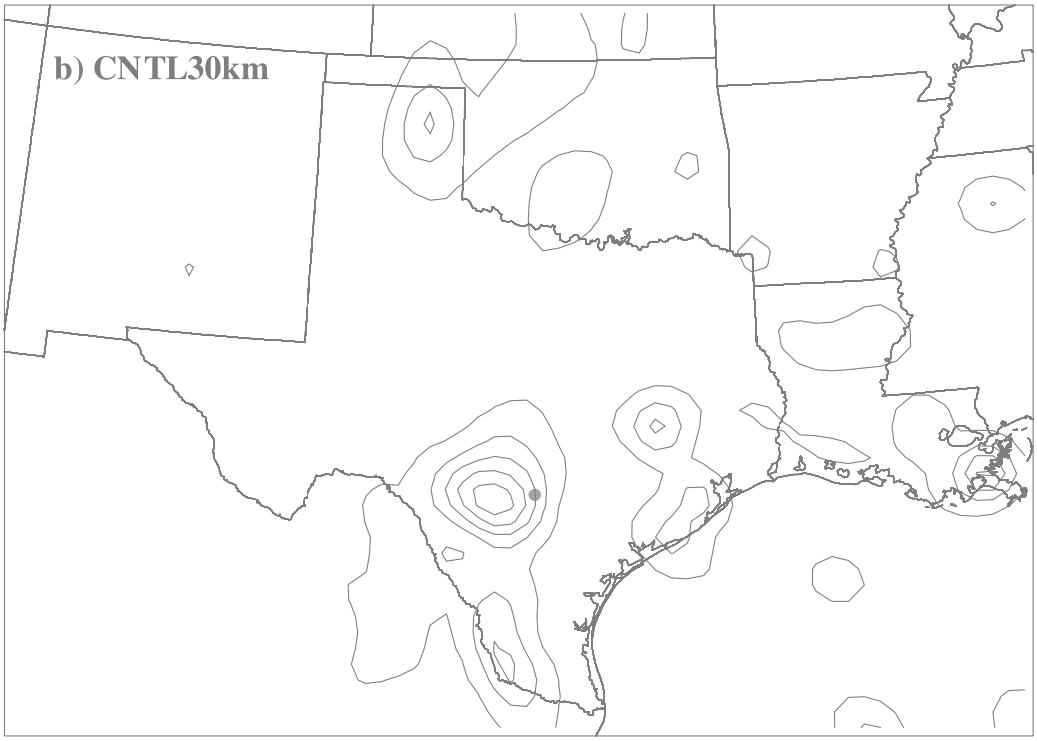

Fig. 4.6 24-hour accumulated precipitation at 12Z 2 July, contours as in Fig. 4.1, (a) Observed; (b) CNTL30km; (c) CPS-KF; (d) NoCPS.

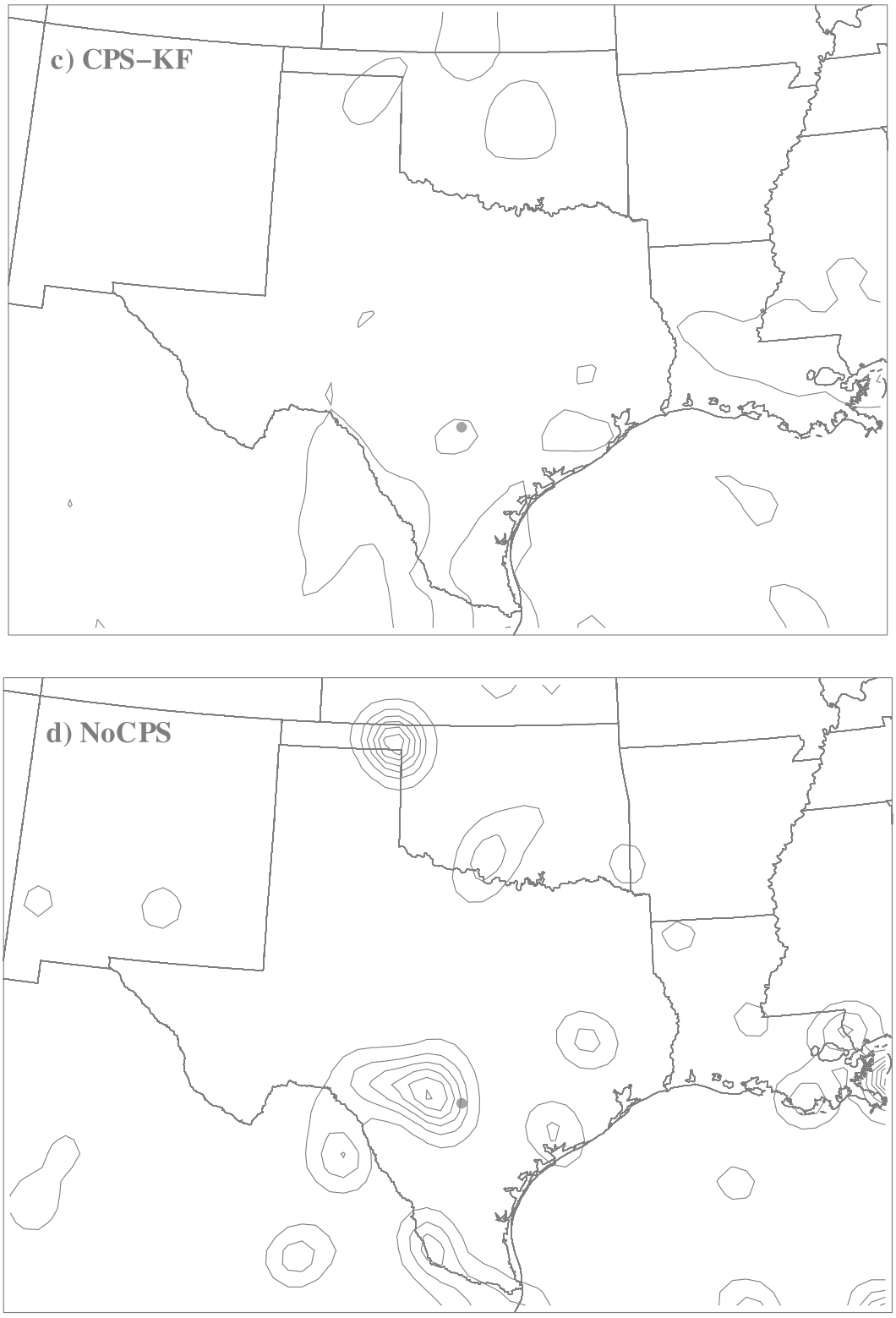

Fig. 4.6 Continued.

there is little to no forecasted precipitation in the area that was flooded, and based upon this forecast, one may predict scattered and light precipitation. A study by Spencer and Stensrud (1998) demonstrated that the CPS-KF parameterization induced mechanisms that propagated boundaries away from the primary convective area, indicating precipitation, but no potential for flooding. Also included in their study were modifications to the CPS-KF parameterization that produced improved 24-hour precipitation totals compared to control simulations. A closer examination of the CPS-KF simulation revealed that the majority of precipitation occurred earlier in the forecast period, between the 6- and 12-hour timeframe, but the precipitation totals still would not be indicative of very heavy rainfall. Further discussion of the onset of precipitation using CPS-KF will be detailed in Chapter V.

The next group of parameterization changes was to the explicit moisture scheme. CNTL30km utilized the Reisner 2 microphysics, which was changed to the Goddard microphysics (EXP-GD) and the Simple Ice (Dudhia) scheme (EXP-SI). The 24-hour precipitation total at the 36-hour forecast is shown in Fig. 4.7; each of the microphysics schemes (except for the high resolution Reisner 1) is shown and compared with observations. There are quite a number of similarities between each of the simulations, and all yield more accurate results to the observations compared to other physics parameterization changes to CNTL30km. First, each forecast shows the potential for heavy precipitation at and around the San Antonio area, with some rainfall in Oklahoma, but farther to the west than the observed rainfall. Second, there is also forecasted precipitation for the New Orleans, Louisiana area as well as for the area between College Station and Houston, Texas. CNTL30km produced heavier rainfall totals than the other

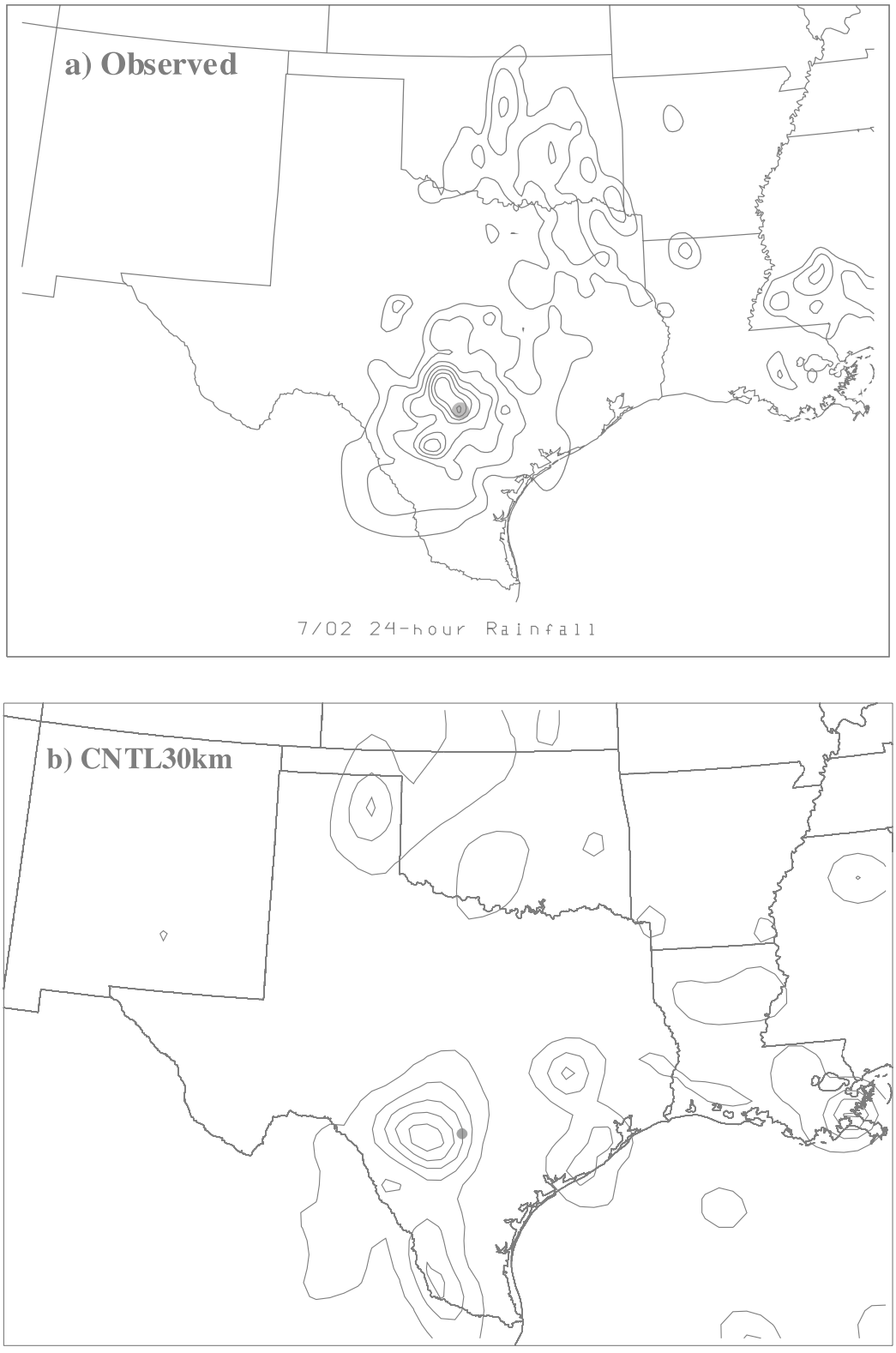

Fig. 4.7 24-hour accumulated precipitation at 12Z 2 July, contours as in Fig. 4.1, (a) Observed; (b) CNTL30km; (c) EXP-GD; (d) EXP-SI.

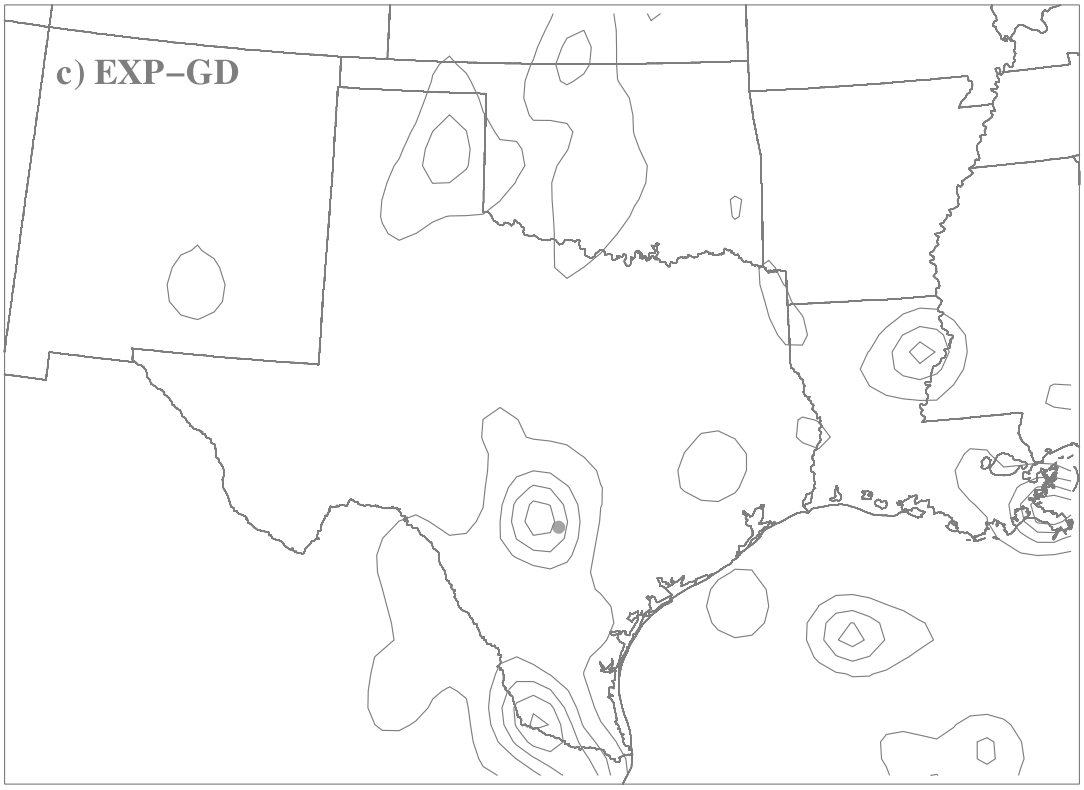

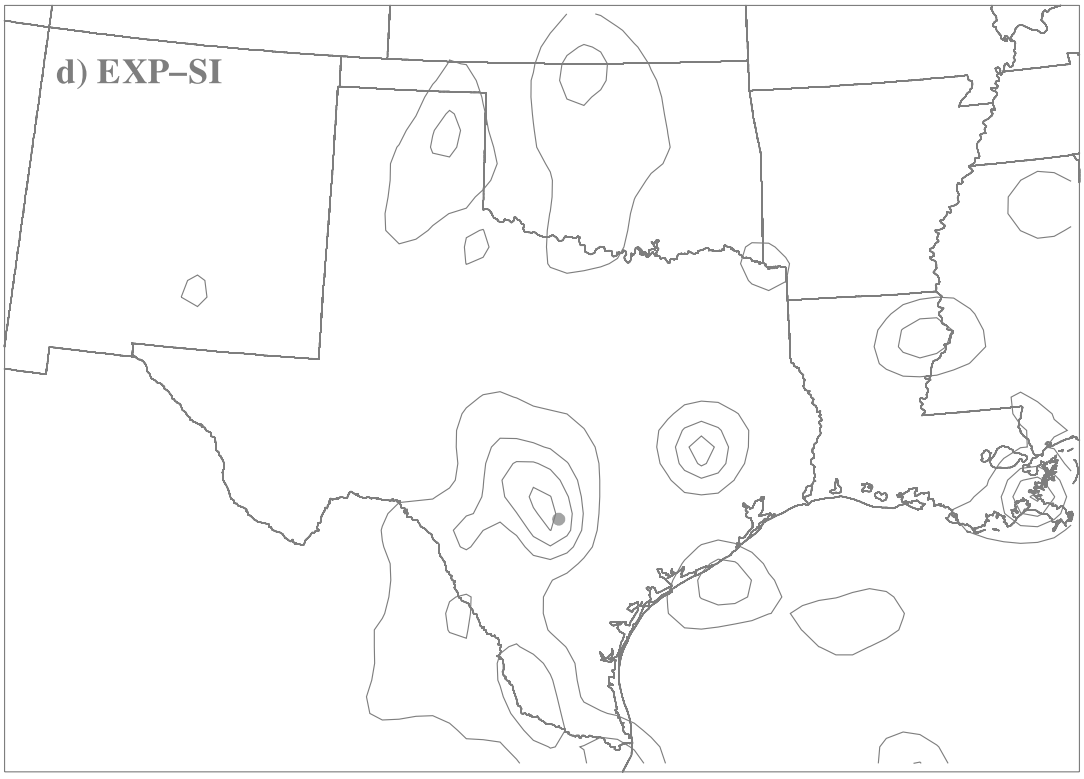

Fig. 4.7 Continued.

schemes including in the vicinity of the College Station area, seen in Fig. 4.7b. The EXP-GD (Fig. 4.7c) forecasted lighter rainfall in this area, which according to observations is more accurate. Since CNTL30km utilized a more complex microphysics option that includes graupel, and the EXP-SI scheme is the least complex of those tested, it is reasonable to speculate that more sophisticated explicit moisture options may be required to accurately represent such extreme events (refer to Figs. 4.7b versus 4.7d). Although the ’02 Flood occurs during the summer and is in the southern portions of the mid-latitudes, such convection would appear to involve other cold-rain processes. This would included graupel and a greater ice concentration that is configured in the Reisner 2 microphysics scheme.

The last group of experiments with varied physics parameterization options consisted of changing the PBL scheme. Recalling that CNTL30km uses the ETA PBL, this option was changed to the PBL-MRF and Blackadar PBL scheme (PBL-HIR). Comparison of each of the PBL options with observations is shown in Fig. 4.8 with the analysis and CNTL30km in Figs 4.8a and 4.8b respectively. Fig. 4.8c shows the PBL-MRF scheme which under-forecasts the rainfall in the San Antonio area, and in general the rainfall is not as widespread. The same holds true for the PBL-HIR simulation (Fig. 4.8d), but the rainfall totals are further reduced near San Antonio. It is interesting to note that the rainfall quantity near New Orleans has increased in both the PBL-MRF and PBL-HIR simulations compared to CNTL30km, since both forecasts indicate heavy rainfall but CNTL30km does not. Some studies have examined the impacts of various PBL and microphysics schemes on convective instability. Bright and Mullen (2001) have investigated convection during the Southwest Monsoon, in which they found that the

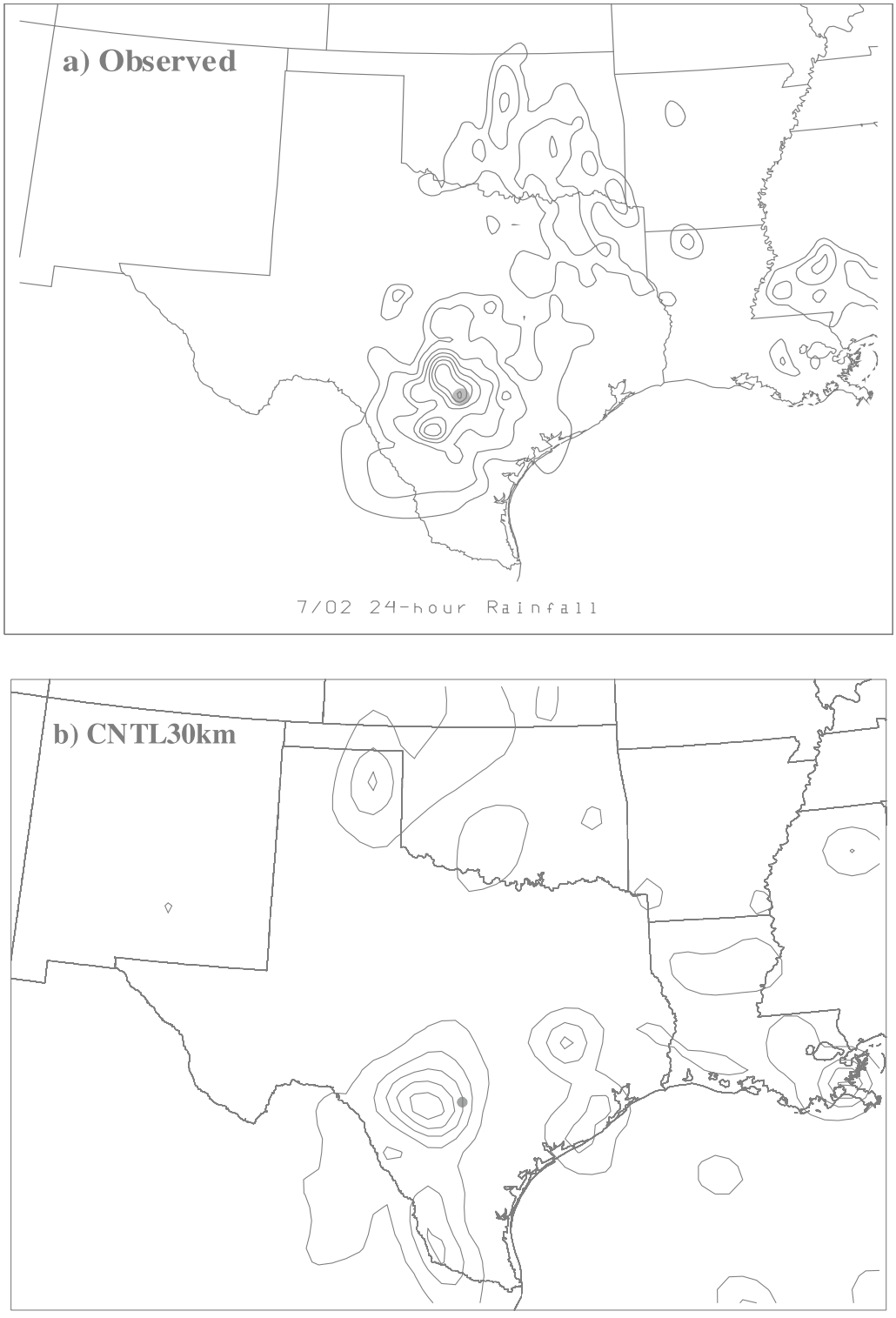

Fig. 4.8 24-hour accumulated precipitation at 12Z 2 July, contours as in Fig. 4.1, (a) Observed; (b) CNTL30km; (c) PBL-MRF; (d) PBL-HIR.

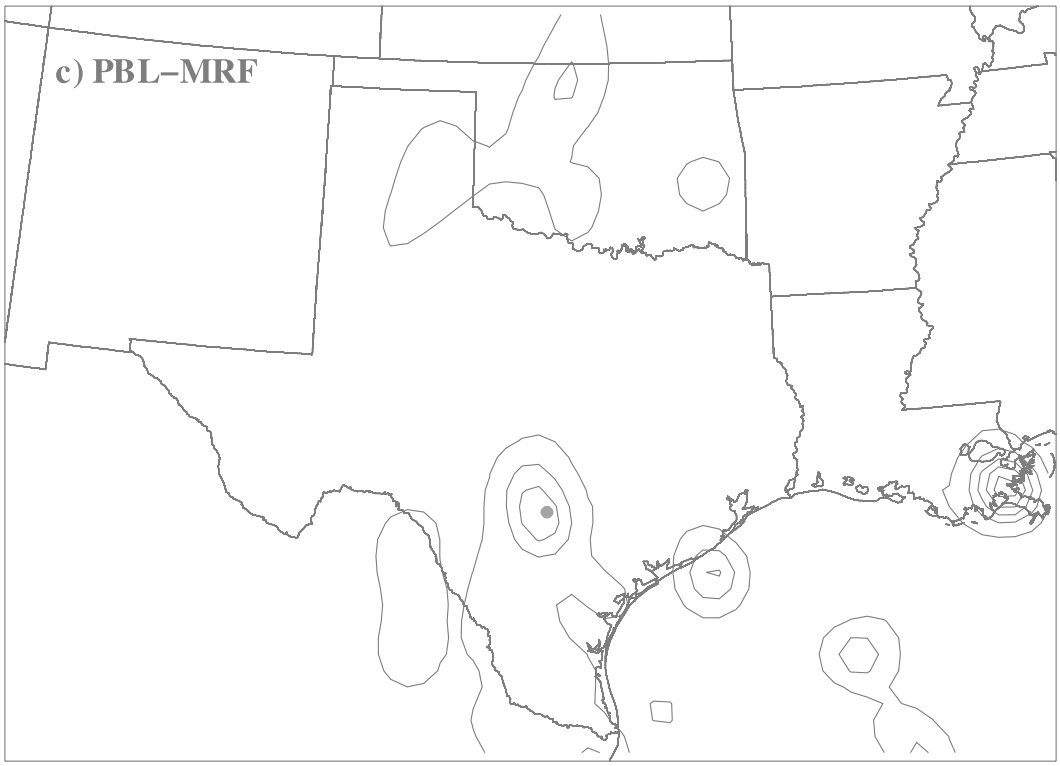

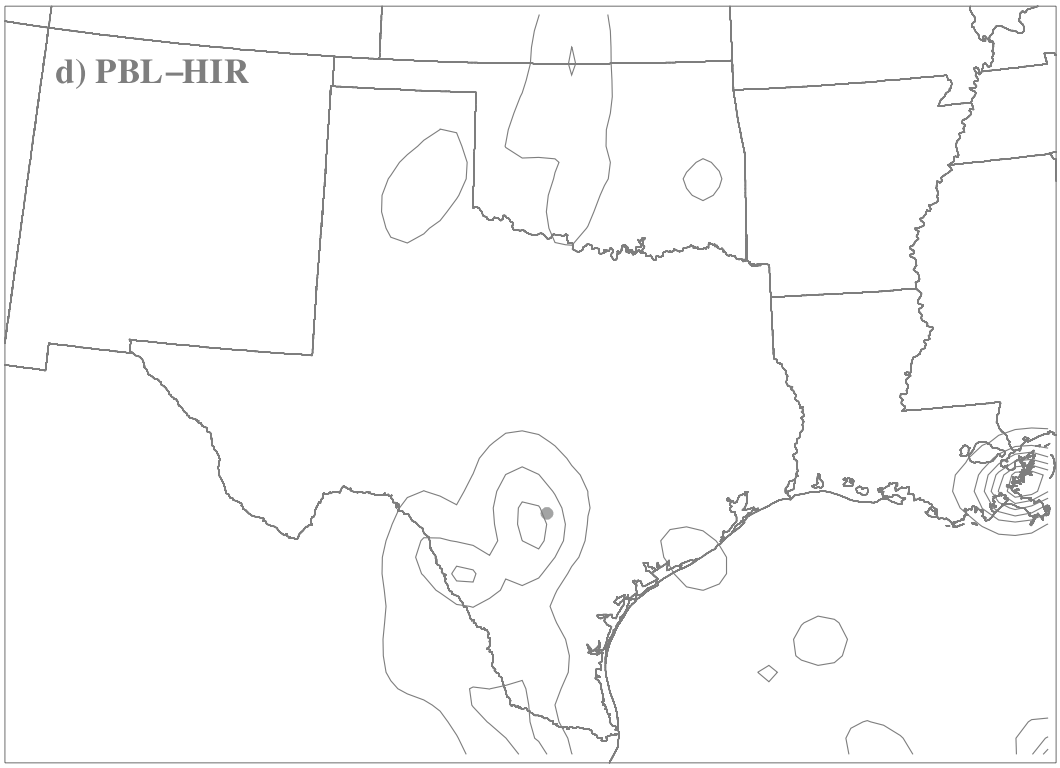

Fig. 4.8 Continued.

PBL-HIR and PBL-MRF schemes produced the best forecast results for the monsoon, whereas the ETA did not.

4.5 Summary of practical predictability results

This chapter explored the fundamental aspects of practical predictability of an extreme weather event. When establishing the importance of practical predictability, one of the primary goals should be to examine the value of a forecast. The context of value used here simply means that a forecast should provide some indication of an extreme weather event to aid in a decision making process. Naturally the forecast lead time is critical; if more advanced notice of an extreme event is given, then this allows for more decision and preparation time. It was found that the greater the lead-time the less valuable the forecast became (refer back Section 4.1), which may be a result of intrinsic limitations and will be examined further in Chapter V; the greatest value occurs with the 24-hour forecast that shows there is likely to be heavy rainfall over San Antonio and the surrounding areas.

With regards to the high resolution simulation, the value has been significantly reduced since the forecast failed to yield heavy precipitation within the 36-hour timeframe in the higher resolution simulations. It is reasonable to speculate that the higher resolution simulations require better initialization during the forecast period in which error growth is fastest. Since it is expected that a high resolution simulation should increase the accuracy of a forecast, especially within a short simulation period, these possibilities would need to be further examined to completely diagnose the practical predictability issues with this event. It was also seen that as the configuration of the

model physics parameterizations changed, the forecast also changed. In some instances, the forecast value decreased significantly, since there was little forecasted rainfall.

This chapter has explored the practical predictability of the ‘02 Flood as it pertains to forecast initialization lead time (initial conditions), model physics parameterizations, and resolution dependence, the latter two both contribute to model errors. Large differences in the initial conditions (from different boundary analyses) or boundary conditions are also significant sources of practical predictability (ZSR03). Since errors occurred with modifications to CNTL30km, how do these errors evolve with time? Chapter V will investigate the error growth dynamics, which will attempt to answer where and how rapidly errors evolve, and what the intrinsic limitations are.

CHAPTER V

INTRINSIC PREDICTABILITY

The previous chapter addressed the different practical predictability aspects. The next question is if a perfect model existed, and the initial conditions are nearly perfect, would forecast errors still develop and how would these errors evolve with time. As previously illustrated, Lorenz (1969) proposed a finite limit of predictability; specifically, intrinsic predictability is, "the extent to which prediction is possible if an optimum procedure is used." ZSR02 and ZSR03 demonstrated the influence of initial errors on numerical weather prediction through the introduction of small-scale, small-amplitude perturbations on the initial conditions. These small errors grew rapidly at the mesoscale, then spread to the larger scales to affect the 24-36 hour forecast. It was found that the rapid error growth stemmed from moist processes, in particular the areas of convective instability. The convective nature of the '02 Flood was a self-perpetuating event that lasted for several days, and the dynamics of this event were more barotropic. Therefore, if optimal procedures are assumed, including a perfect model assumption, what would be the source of intrinsic errors; thus stems the motivation to evaluate the evolution of error growth under these assumptions.

The methodologies used in these experiments will include the incorporation of random grid-point perturbations to the initial conditions, similar to TZRS04, however different from ZSR03. This form of initial condition uncertainties leads to a representation of random small-scale errors. Uncertainties in the boundary conditions are neglected, similar to ZSR03 in which the region of interest is far from the boundaries.

Section 5.1 will illustrate the error growth of CNTL30km followed by a comparison between error growth and resolution, realization, and magnitude in section 5.2. Error growth in different days and diurnal variation of the error evolution will be discussed in section 5.3, followed by the effects of moist convection and parameterized physics in section 5.4.

5.1 Error growth in the CNTL30km

As in TZRS04, random grid perturbations of amplitude 0.2K were added to the initial temperature field of CNTL30km, and a 36-hour forecast, PERT30km, was performed. Three-hour accumulated precipitation differences between CNTL30km and PERT30km are shown in Fig. 5.1; Fig 5.1a shows CNLT30km as seen in Chapter IV. After only three hours of simulation, small differences appear in northeastern Texas and northern Alabama, as seen in Fig. 5.1b. Fig. 5.1c shows a spreading of the spatial coverage along the southeast United States and an increase in the magnitude of the differences following twelve hours of simulation, including difference dipoles in South Carolina, Florida, and a weak dipole in Texas near San Antonio. A dipole structure of the difference fields denotes a spatial shift of the forecast variable from one simulation to the other. After 24 hours of simulation, the difference field has spread farther across the domain (Fig. 5.1d) with an increase in the number of higher magnitude differences. Lastly, Fig. 5.1e shows not as much spreading of the differences over the domain, but there is an increase in the difference magnitude, and the number of higher magnitude

Fig. 5.1 The 3-hour precipitation difference between CNTL30km and PERT30km initialized at 00Z 1 July for the (b) 3-, (c) 12-, (d) 24-, and (e) 36-hour forecast time. Contour intervals are every 4 mm; dashed lines indicate negative values. (a) shows the CNTL30km 24hr precipitation total for the 36hr forecast; contours as in Fig. 4.1.

differences has increased compared to Fig. 5.1c. To further exemplify the extent of the difference field across the domain and magnitude of the difference field, Fig. 5.2 shows the 24-hour accumulative precipitation difference of the 36-hour simulation, in which the maximum difference between the two simulations is 70 mm (2.75 inches).

To further illustrate the error growth at low resolution, a difference field of the y-component of the wind velocity is depicted at the 350K isentropic level. The difference wind fields (Fig. 5.3), when compared with the difference precipitation fields, show a similar results in that the differences grow in magnitude and across the domain as the simulation time increases. Fig. 5.3a shows a very small magnitude and localized difference in northeast Texas following three hours of simulation. The differences have grown considerably, however, in the 12-hour forecast time (Fig. 5.3b), but are concentrated primarily over South Carolina, Georgia, and Florida. The differences spread substantially over the domain by the 24-hour forecast simulation (Fig. 5.3c), to encompass much of the southeastern United States, portions of Texas, and the states surrounding Lake Michigan. Also, the spatial coverage of differences across the domain has spread considerably, and the magnitude of the positive and negative differences has increased to a maximum of 11 ms^{-1}. By the 36-hour forecast (Fig. 5.3d), there has been a substantial increase in the spatial extent ofe the errors, as well as an increase in the quantity of errors over the domain. The maximum difference (between the positive and negative differences) has also increased to 15 ms^{-1}. Both the wind and temperature differences (not shown) show a similar pattern at other isentropic and pressure levels in the troposphere: as the forecast simulation progresses, the errors increase in magnitude, and the spreading of errors over the domain increase.

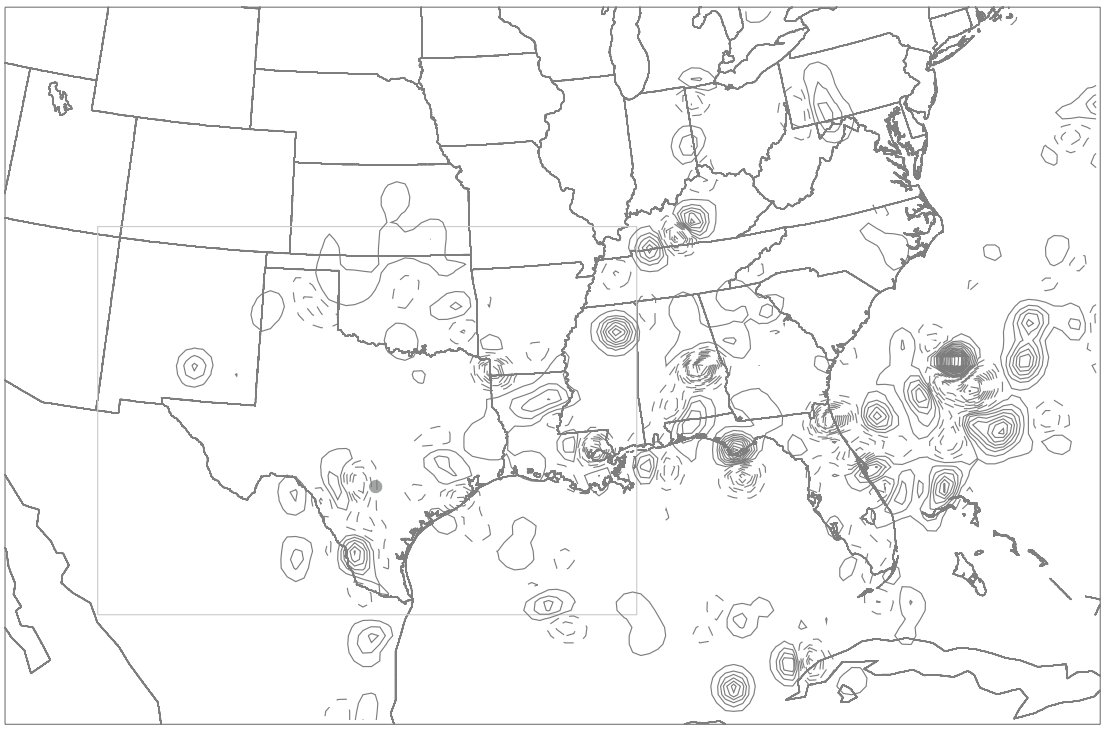

Fig. 5.2 The 24-hour difference between CNTL30km and PERT30km at 36-hour forecast time, initialized at 00Z 1 July. Contour intervals are every 4 mm; dashed lines indicate negative values.

Fig. 5.3 The difference field of the y-component of the wind velocity at the 350K isentropic level between CNTL30km and PERT30km at 00Z 1 July for the (a) 3-, (b) 12-, (c) 24-, and (d) 36-hour forecast time. Contour intervals are every 1 ms^{-1}; dashed lines indicate negative values.

The most significant differences grow in magnitude and across the domain between the 3 to 12 hour forecast, then the differences quickly saturate. It is apparent that very slight perturbations, essentially representing two nearly perfect initial conditions, can lead to noticeable errors in as early as a 12-hour forecast time. The reason for this, as proposed by ZSR03, is that flow of interest at some locations during its evolution may lie close to critical points where the instability is at a threshold of being stable or convectively unstable. Since the values at these grid points are not known exactly, any slight deviation can trigger convection differently or at different locations, thus resulting in errors at such locations which spread to the mesoscale. This is observed in Figs. 5.2, which shows that the accumulated precipitation is small, but the location of the convection has been altered, thus resulting in a shift in the precipitation pattern. There is no doubt that greater temperature deviations than 0.2K can be present at these critical points, and may trigger greater differences, which will be addressed later in this chapter.

To further explore the error growth, a power spectrum analysis, examining DTE (defined in section 3.4) at different wavelengths, is shown in Fig. 5.4. As suggested by the previous difference plots, the most rapid error growth occurs between the 3-hour and 12-hour simulation: very little error growth is noted in the first 3 hours, however by the 12th hour substantial differences have evolved and spread over a much larger area than the third hour results. The spectral analysis shows the greatest error growth occurring between the 6- and 9-hour simulation, corresponding to the difference fields in Figs. 5.1

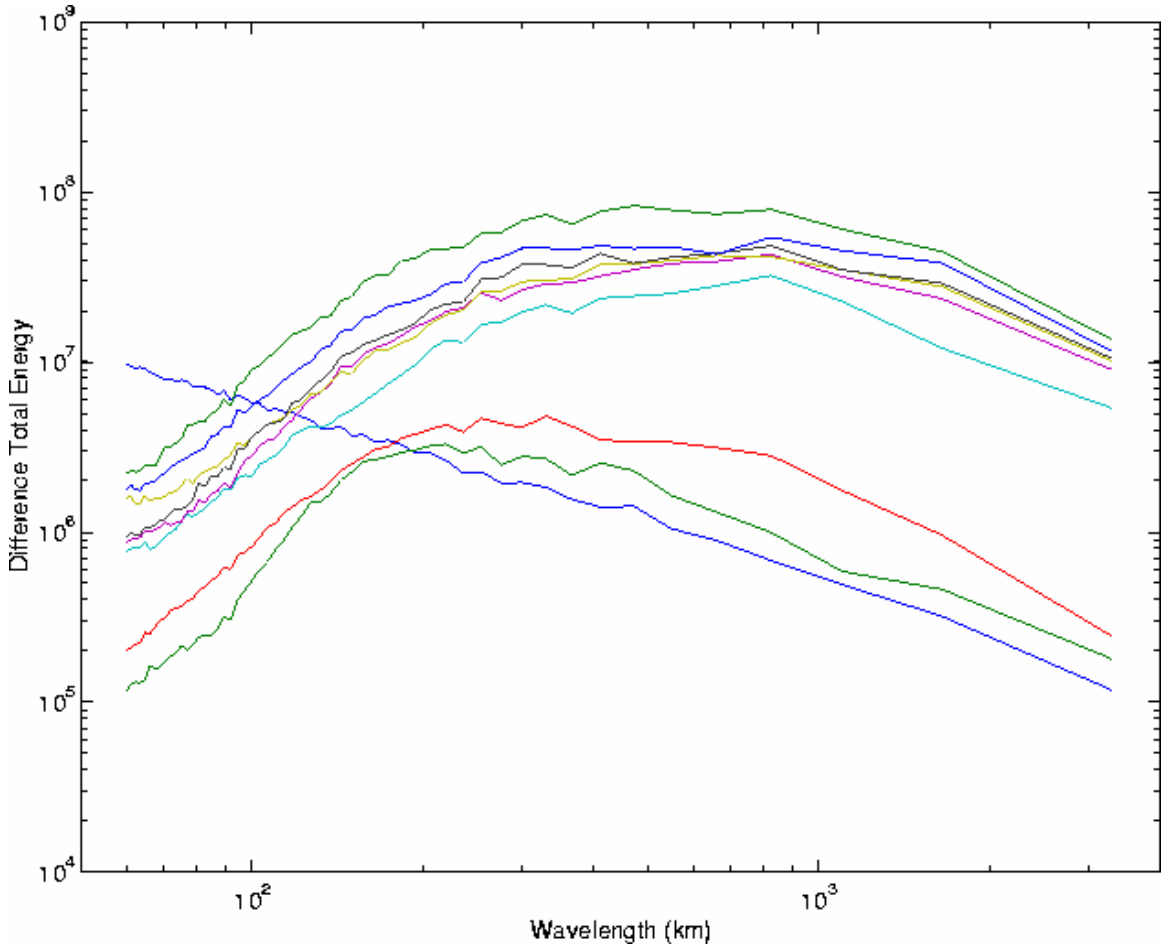

Fig. 5.4 Power spectra of the DTE (m^2s^{-2}) between CNTL30km and PERT30km plotted every 3 hours.

and 5.3. The evolution of growth slows after the 12-hour forecast, with a slight increase in the error growth between the 21- and 27-hour forecast, more prevalent at the smaller wavelengths. The peak of the spectrum at each forecast time interval shifts to the right, or shifts towards a larger wavelength, particularly in the earlier simulations, which correlates to the increase in the spatial scale and the extent of forecast differences (ZSR03). It is important to note that the spectral peak in each simulation appears to not extend beyond 1000 kilometers. ZSR02 reported that differences decayed at scales larger than 1000 kilometers due to each simulation using the same lateral boundary conditions (ZSR03, and studies from Vukicevic and Errico 1990 and references therein).

The evolution of DTE between CNTL30km and PERT30km is shown in Fig. 5.5. Following a slight decrease in forecast error over the first three hours, there is a marked increase in the DTE over the next six hours, then the rate of error growth slows over the next 24 hours. This clearly shows the timing of the greatest forecast error growth to be early in the forecast period, between hours 3 through 19. There is an abrupt decrease in the first 3 hours, followed by steady error growth. Similar to TZRS04 the initial decrease in DTE during the first few hours of simulation can be explained through the notion that the initial error, essentially random noise, decreases via numerical diffusion, or geostrophic adjustment, over the domain by the temperature being unbalanced with respect to the U and V wind fields, then eventually becoming balanced; the difference growth occurs in the areas of moist convection (TZRS04). Following this slight reduction in DTE, the sharp error growth observed in Fig. 5.5 is mostly due to moist processes, which will be discussed in more details in section 5.4.

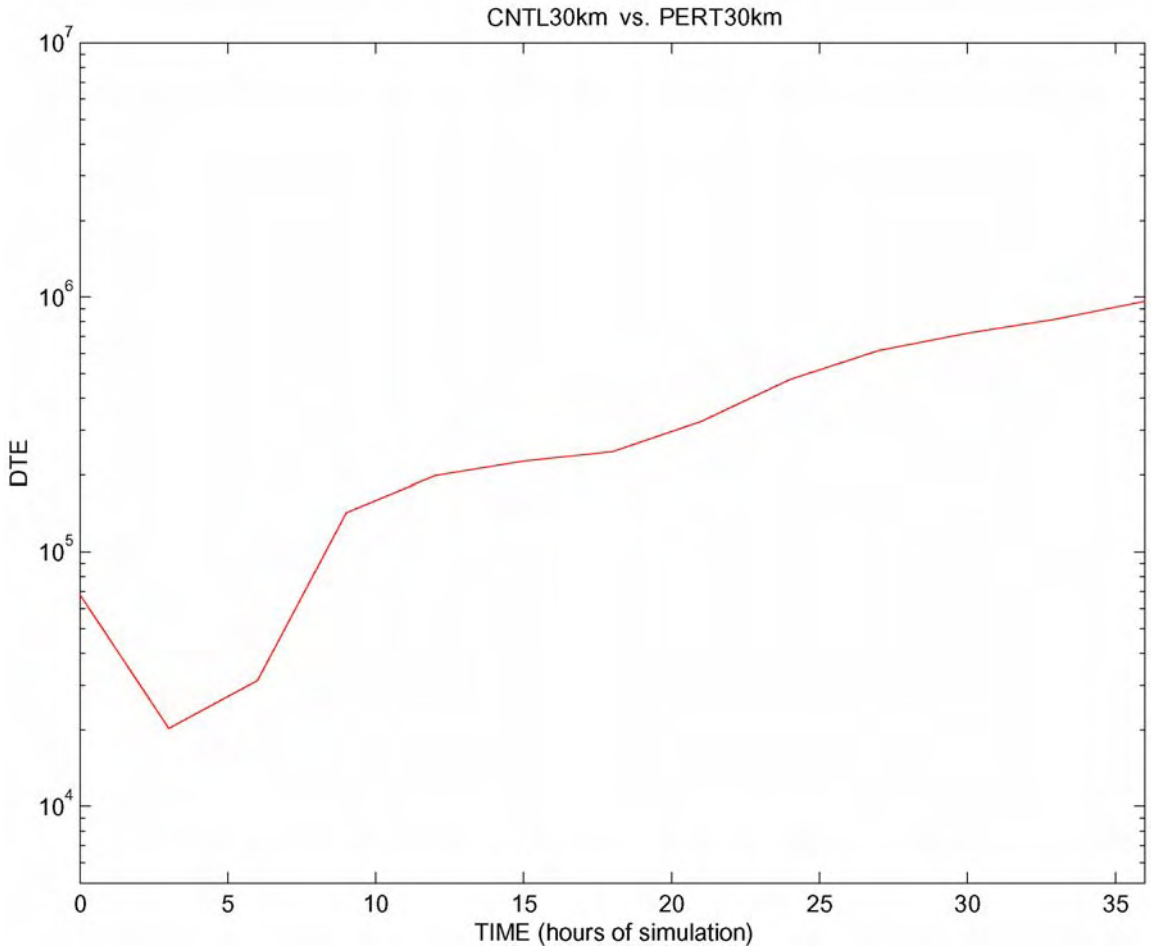

Fig. 5.5 Evolution of DTE (m^2s^{-2}) between CNTL30km and PERT30km.

The maximum accumulated precipitation difference stemming from small random noise was 70 mm, and this is of secondary importance when compared to the observed differences from the practical predictability experiments, when the initial errors are quite large and the model error is substantial. Compared to the results of ZSR03, the error growth is substantially smaller. However, these research results for the ’02 Flood are consistent with TZRS04, which may support the lack of a large area of convective instability. The weaker error growth could also be due to weaker larger-scale instability for the current event.

5.2 Error growth versus resolution, realization, and magnitude

The next question to address is whether or not the results from the low resolution experiments coincide with those of a high resolution simulation. A pair of two-way nested simulations (HIGH3.3km, and PERT3.3km) were performed using a 0.2K perturbation amplitude (same initial condition as PERT30km) as described previously. The resulting difference fields and graphs were created using the first domain of the high resolution forecast for comparison with the 30-km domain (HIGH30km and PERT30km) at the same forecast time. The difference fields, Figs. 5.6 and 5.7, show a close resemblance to the coarser simulations (Figs. 5.1 and 5.3); the compared parameters (precipitation and wind) diverge in a similar fashion between the two resolutions. There is slightly stronger error growth with PERT10km and PERT3.3km forecasts (Fig. 5.8), but there is a very similar error growth spectrum to PERT30km simulation (Fig 5.9). These differences between the error growth in the high and low resolution simulations are also smaller than those found in ZSR03.

Fig. 5.6 (a-e) as in Fig. 5.1, but between HIGH30km and PERT30km.

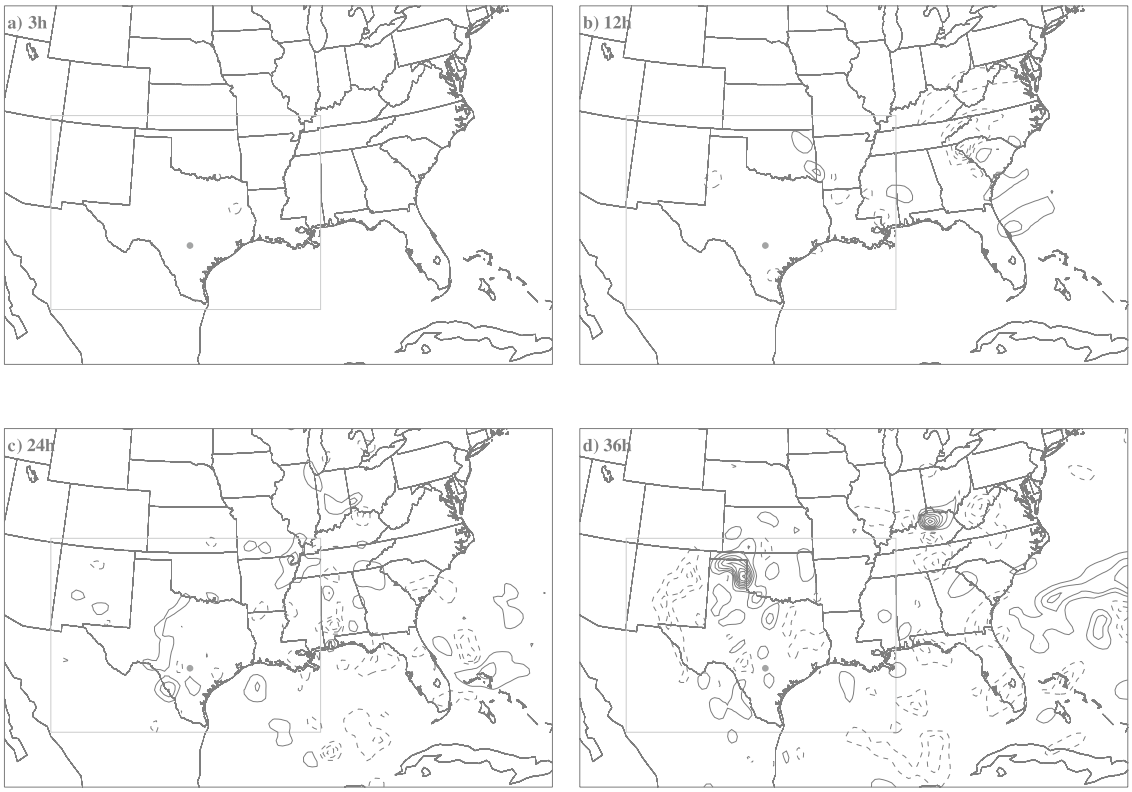

Fig. 5.7 (a-d) as in Fig. 5.3, but between HIGH30km and PERT30km.

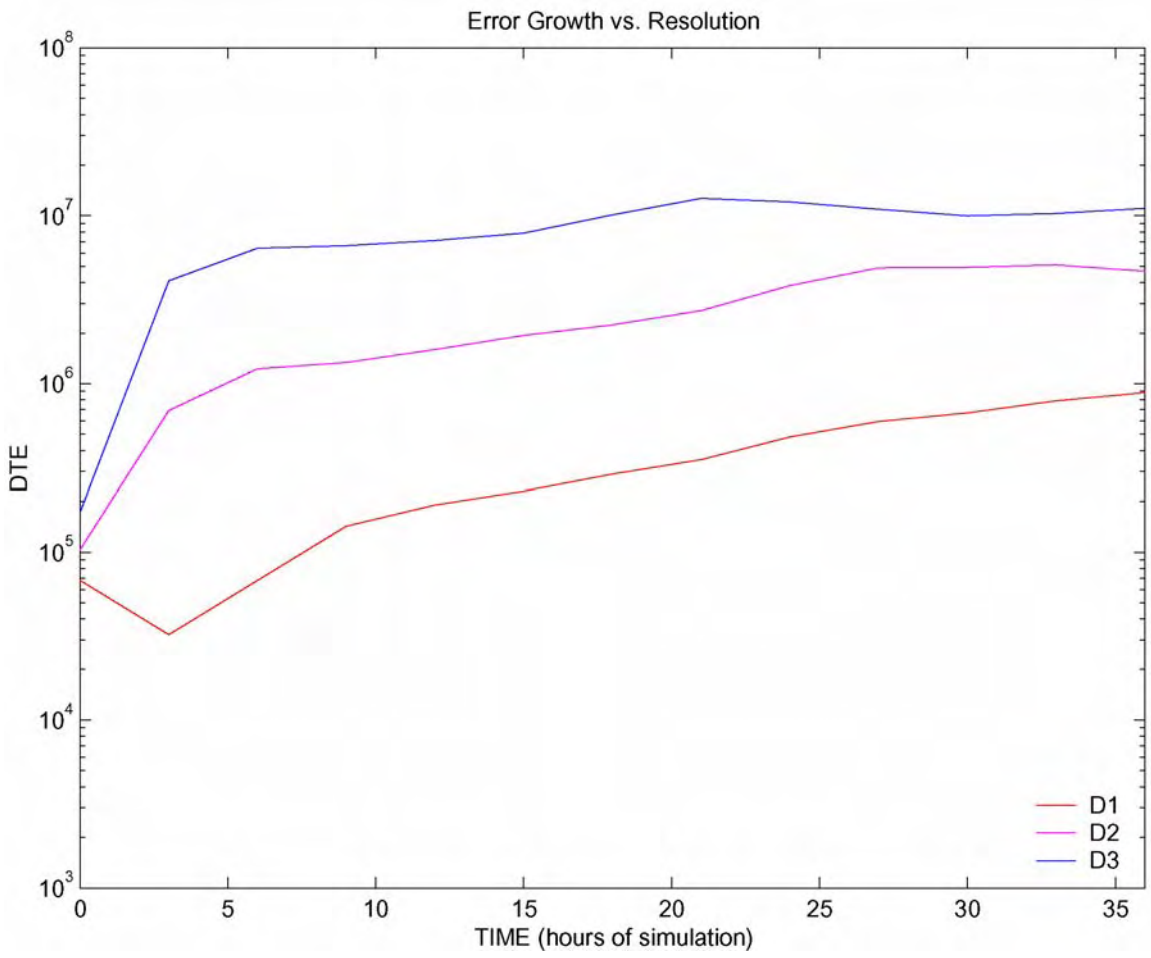

Fig. 5.8 Evolution of DTE, as in Fig. 5.5, but for HIGH30km-PERT30km (D1), HIGH10km-PERT10km (D2), and HIGH3.3km-PERT3.3km (D3).

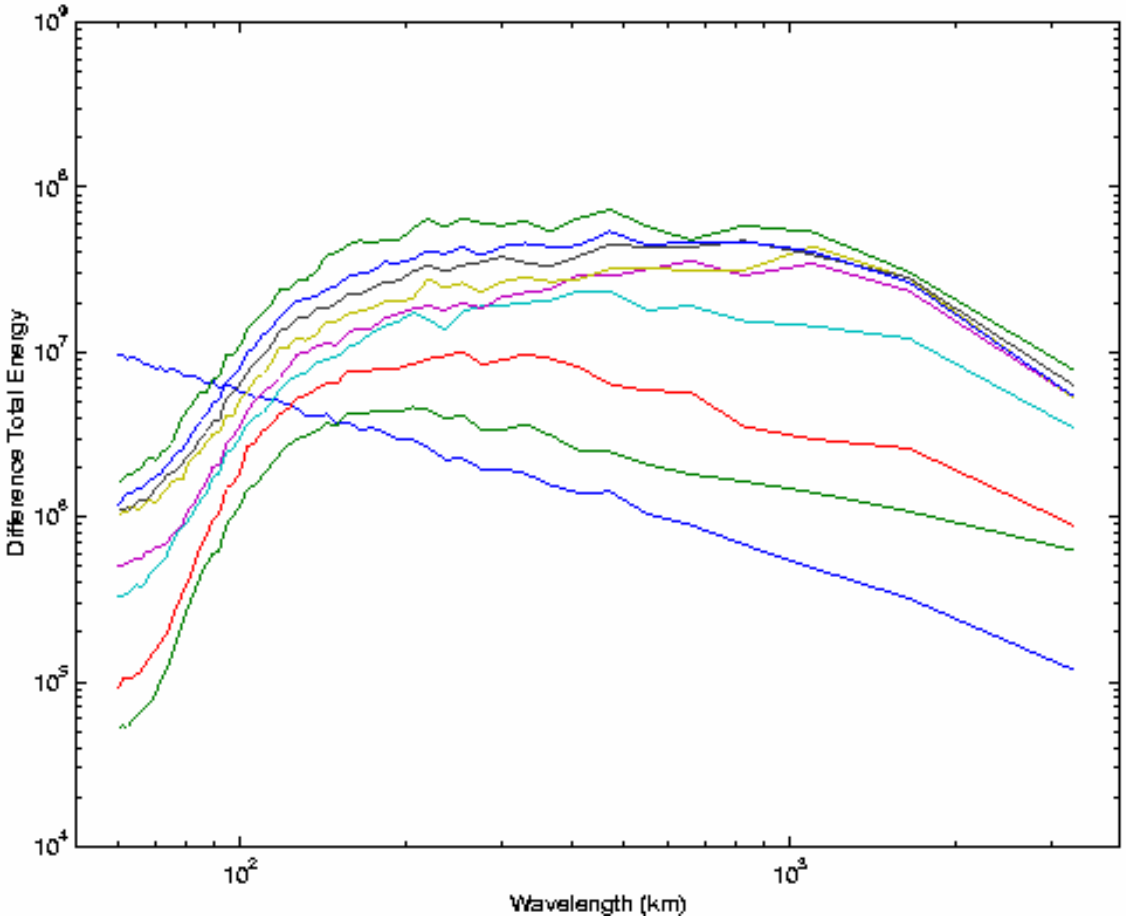

Fig. 5.9 Power spectra of DTE, as in Fig. 5.4, but between HIGH3.3km and PERT3.3km.

There are some dissimilarities between the low and high resolution results. First, there is greater spreading of the differences over the domain earlier in the forecast period (comparing the 12-hour results) for the high resolution simulation, as well as an increase of errors over the domain. Second, the maximum amplitude of errors is reached earlier in the high resolution simulation. This coincides with Lorenz's theory that there is a finite limit of predictability despite improvements in resolution (ZSR03, Lorenz, 1969). Given a high resolution simulation, errors tend to grow much faster, thus indicating a finite limit of predictability.

The next set of experiments included running five additional simulations using the control perturbation amplitude (0.2K) for each. The purpose of this is to determine the sensitivity of the error growth from realization to realization due to the randomness of the perturbations. Since the perturbations are random across the domain, essentially white noise, small discrepancies were expected. The power-spectrum analysis for another realization (denoted R-2) is shown in Fig. 5.10; when compared with PERT30km (Fig. 5.4), they show very similar results. The evolution of error growth of each random realization is shown in Fig. 5.11. Each realization behaves in a closely related manner to PERT30km with no significant outliers; the control simulation is higher than the others during the 6-9 hour period. This is also the timing of the largest spread, which is during the nighttime when CIN is typically the strongest; thus this period may be the most sensitive to convective triggering.

Similar to ZSR03, experiments have been performed with different perturbation amplitudes. To reiterate from Section 3.4, the perturbation amplitudes were changed from the PERT30km simulation of 0.2K, to 0.002K, 0.02K, 0.4K, 1.0K and 2.0K.

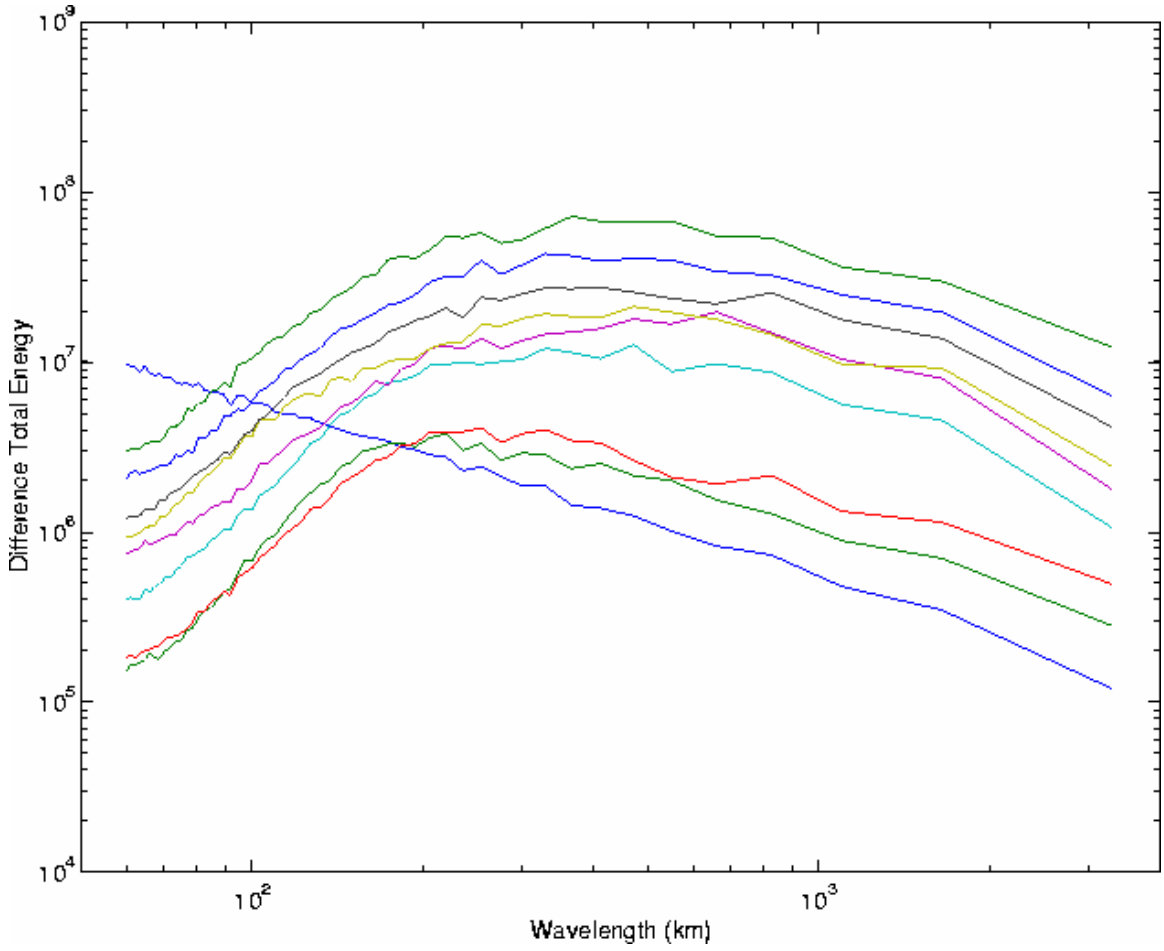

Fig. 5.10 Power spectra of DTE, as in Fig. 5.4, but for another realization (R2) with perturbation amplitude of 0.2K initialized at 00Z 1 July.

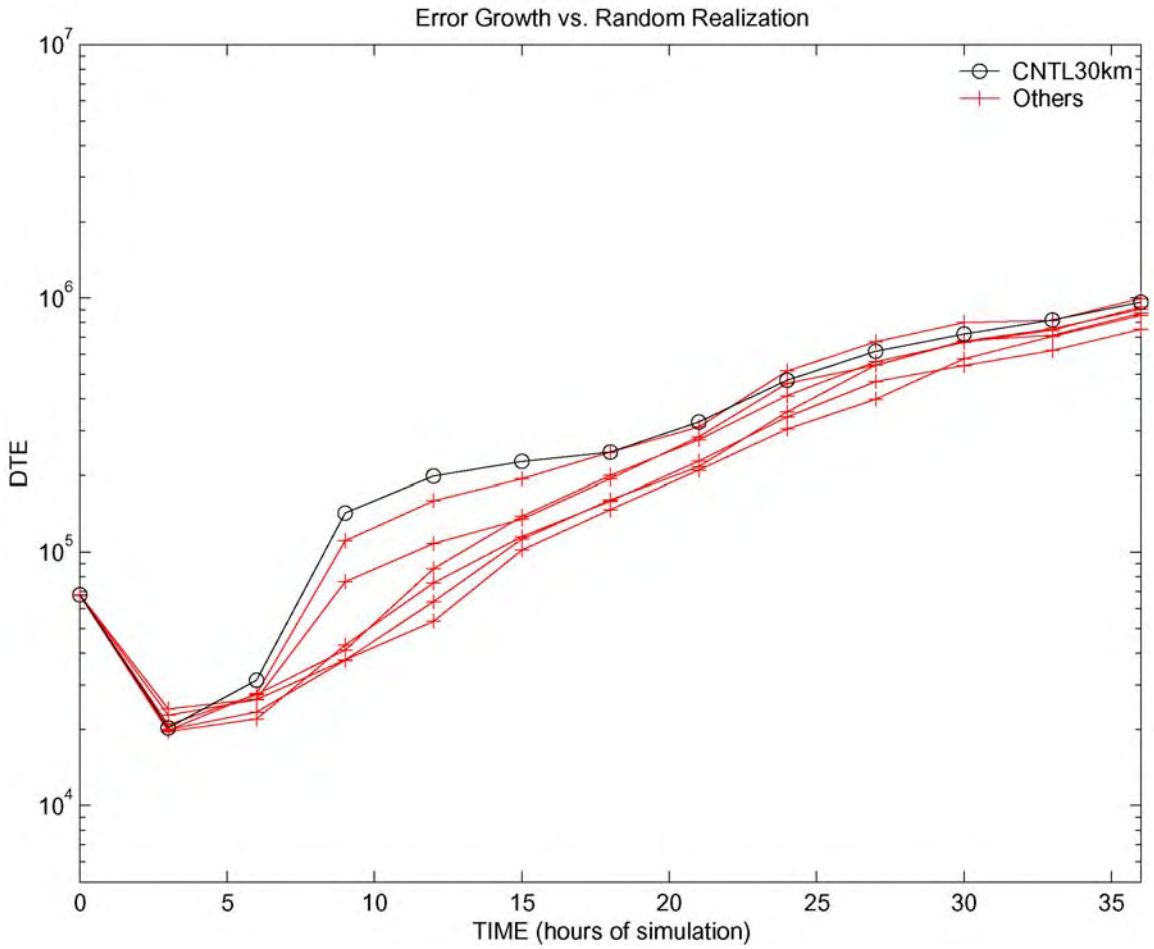

Fig. 5.11 Evolution of DTE, as in Fig. 5.5, for all realizations with perturbation amplitude of 0.2K initialized at 00Z 1 July.

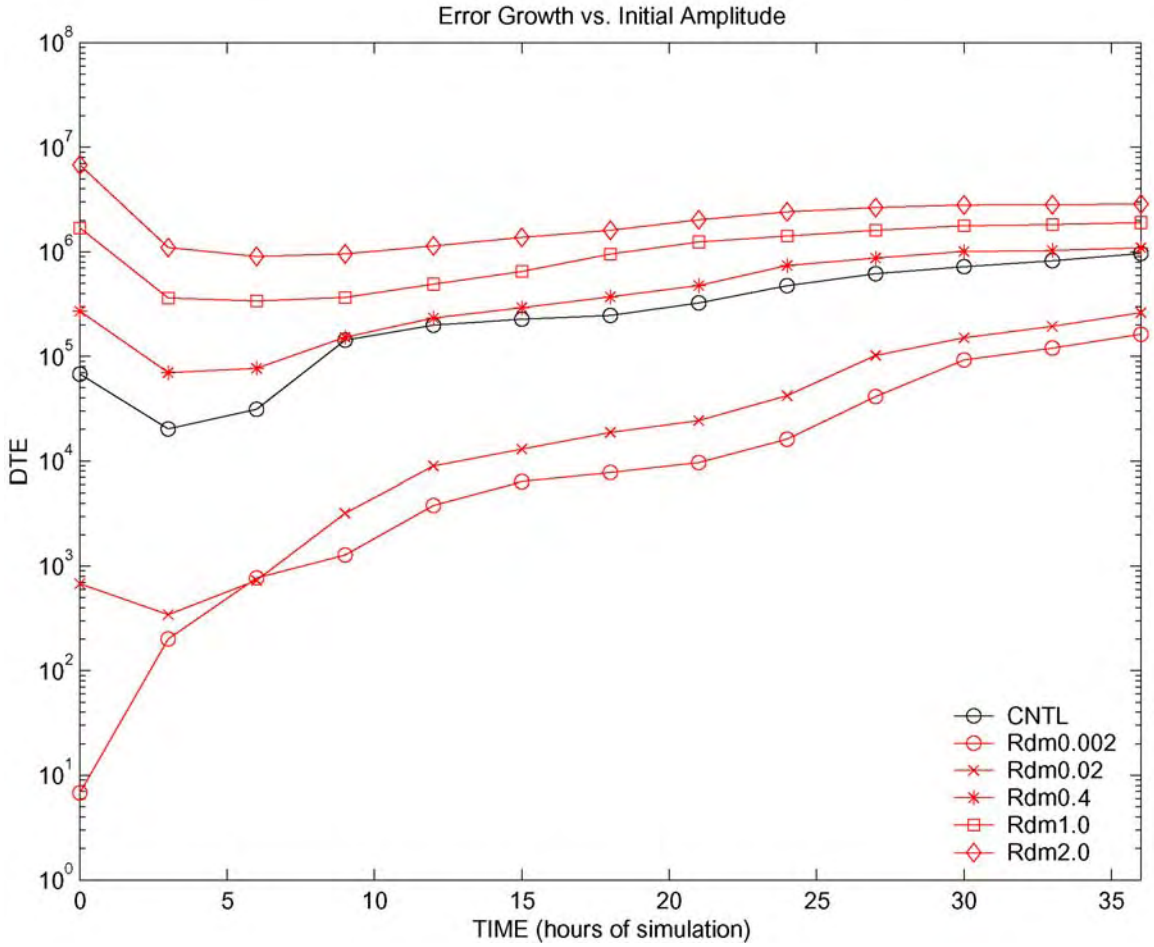

Fig. 5.12 Evolution of DTE, as in Fig. 5.4, but with experiments with idealized perturbations of different magnitudes in the initial temperature field. Curves are labeled with the values of T_0 in Eqn. 3.1.

Generically speaking, the smaller amplitude perturbations generate errors that grow faster at the mesoscale, but then these differences approach a saturation level close to the DTE with a higher initial perturbation amplitude after 36-hours of simulation; this is illustrated in Fig. 5.12. The fact that the growth of the forecast errors varies upon perturbation amplitude indicates that the evolution of the differences is non-linear (ZSR03). This implies that a limit is reached, given current computational abilities, in which there is diminishing return; although initial errors can be reduced, say by half, the forecast accuracy increases only a few hours (ZSR03).

5.3 Error growth for different days and diurnal variation at 00Z and 12Z

The ‘02 Flood lasted for eight days with little synoptic movement, though there exists a strong variation of the convection. Since the convective instability over the whole region of interest shows the same diurnal variation over the entire duration of the event, it was important to investigate the intrinsic error growth each day to determine any possible outliers that may exist. In conjunction with this experiment, the initial error growth due to the diurnal variations (00Z and 12Z respectively) is examined as well. Similar experiments to PERT30km were set up, using a 0.2K perturbation amplitude initiating at each day from 28 June through 5 July, both at 00Z and 12Z.

A power spectrum of a 12Z simulation, initialized at 30 June (figure not shown) exhibits a very similar pattern as Fig. 5.4, the spectral analysis between CNTL30km and PERT30km. Fig. 5.13 shows the evolution of error growth for each initialization. The ensemble of results is very consistent with PERT30km: there is a decrease in DTE within the three-hour forecast, with one 12Z initialized forecast decreasing in DTE through six hours. This is followed by an increase in the DTE over the next twelve hours, and a

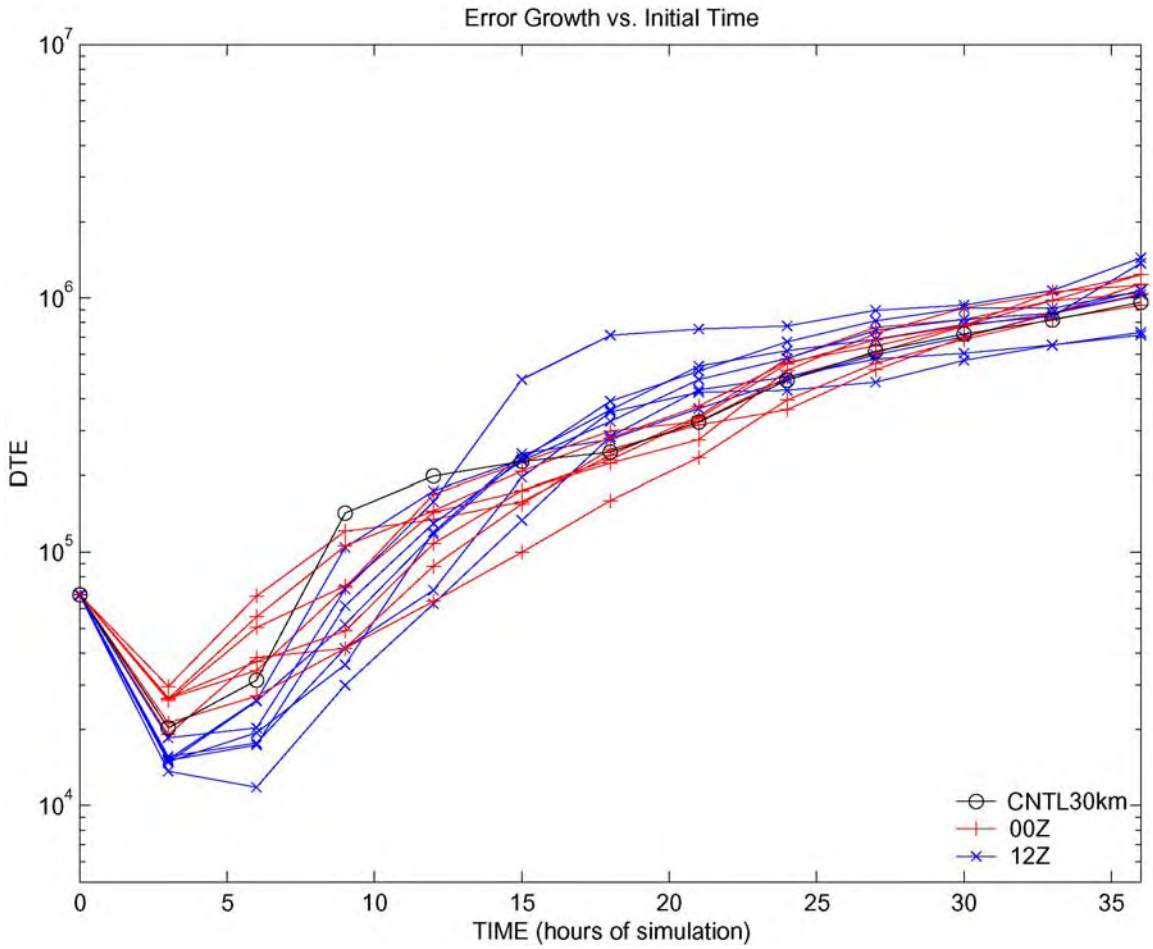

Fig. 5.13 Evolution of DTE, as in Fig. 5.5, for all initialization times every 12 hours beginning at 00Z 28 June and ending 12Z 5 July. 12Z initializations are blue, and 00Z initializations are red.

rather tight saturation in the latter forecast times. The greatest evolution of error growth occurs approximately six hours into the simulation with the 12Z realizations; since this corresponds to an early morning initialized forecast, there is greater stability in which the convection must overcome. As diabatic heating occurs later in the day, corresponding to a later simulation time, then destabilization occurs initiating convective instability. Coincidentally, the greatest DTE growth occurs after the six-hour forecast time, when the strongest convection likely occurs (between 18Z and 21Z). Further evidence of the diurnal variation can be seen later in the forecast period: the DTE of the 00Z simulations increases slightly between simulation hours 15 through 24, while little DTE growth slows in the 12Z simulations between simulation hours 21 through 30, coinciding with less instability that occurs during the nighttime.

5.4 Effect of moist convection and parameterized physics

ZSR02 found that moist processes played a critical role in forecast divergence early in the forecast period. This was farther investigated in ZSR03 through the use of a "fake-dry" simulation; the results showed that DTE was significantly reduced without latent heating taking place. Although error growth and upscale spreading of differences are weaker than the results found in ZSR03, it is still found that initial rapid error growth originates from parameterized moist processes. Fig. 5.14 shows the evolution of error growth in the "fake-dry" simulation for the '02 Flood, in which the latent heat release from moist processes is turned off (details in Section 3.4). These results are consistent with those of ZSR03, in which the error growth is significantly reduced throughout the forecast duration. Following the initial decrease in DTE up to the three-hour forecast,

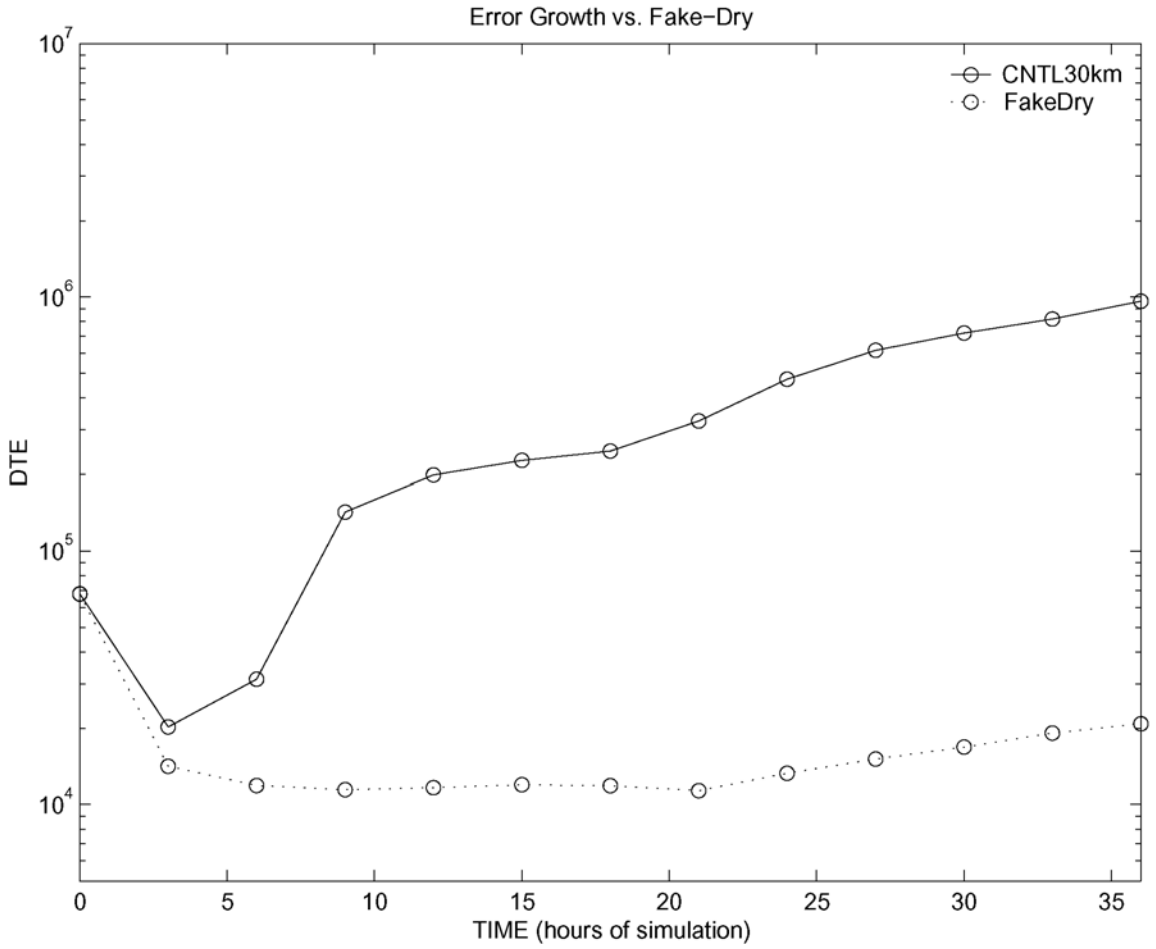

Fig. 5.14 Evolution of DTE, as in Fig. 5.5, but for the fake-dry experiment (dotted curve). Solid curve shows the moist experiment.

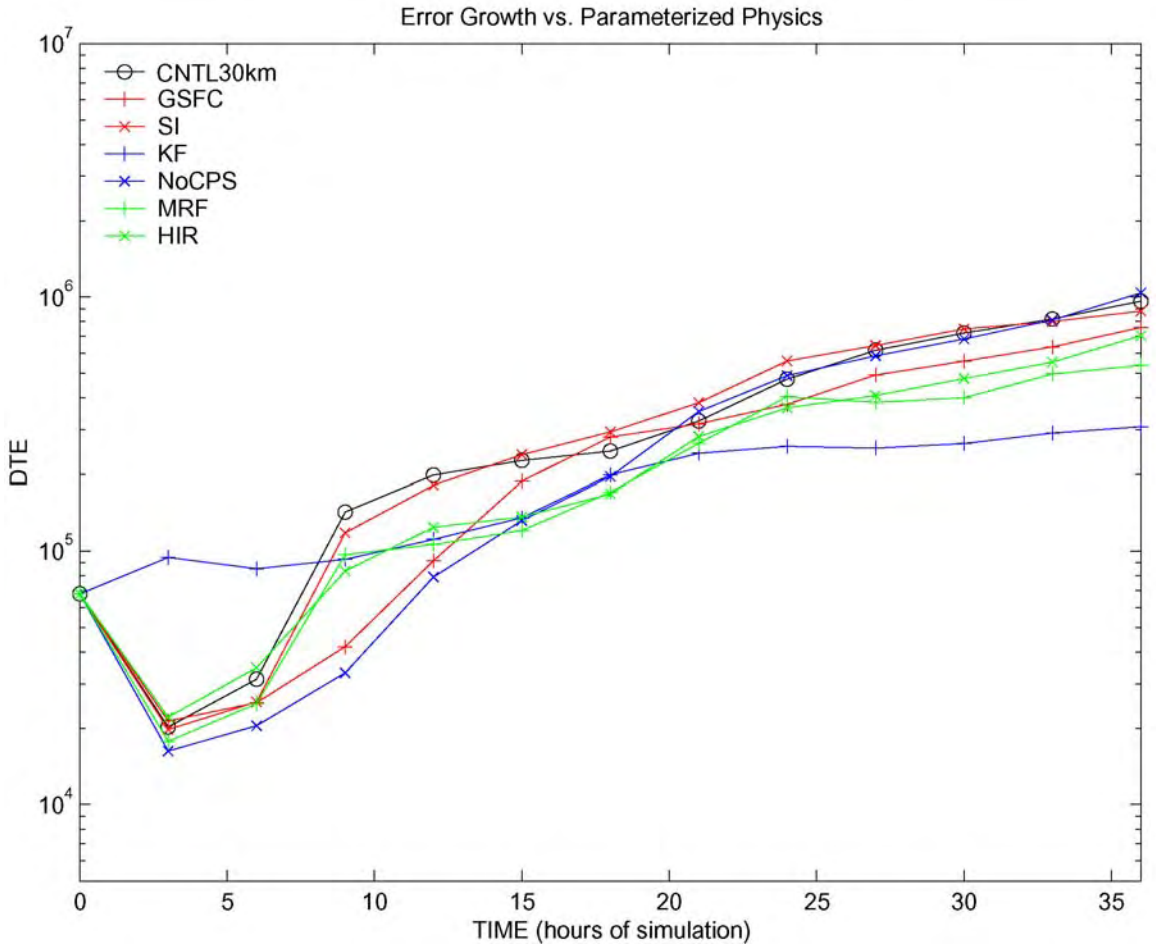

Fig. 5.15 Evolution of DTE, as in Fig. 5.5, but for all different physics parameterization schemes used. Also includes the fake-dry experiment.

there is not any significant increase in DTE as compared to the other perturbed simulations that incorporates latent heating.

To ensure that the evolution of error growth observed in these results is not prone to one type of convective parameterization, the last group of experiments incorporates the physics parameter changes as presented in the practical predictability section (section 4.2). Following an unperturbed simulation with a change in one physics parameter, a second was conducted using the control perturbation amplitude of 0.2K; this was done for each of the six different physics parameters (detailed in the Section 3.4). Fig. 5.15 shows the evolution of the error growth for each pair of simulations, and includes the fake-dry simulation and the high resolution simulation of domain 1; recall that the high resolution forecast required the use of Reisner 1 microphysics. Most DTE curves behave in a similar fashion to the previous experiments with a slight decrease through the 3hr forecast, a sharp increase of DTE through the 12hr forecast, followed by a saturation towards the latter forecast times. Aside from the fake-dry experiment, only the CPS-KF experiment tends to behave differently. Instead of an initial decrease in DTE, there is a slight increase in the first three hours, then a slight decrease for the next three hours, followed by slight increase in DTE through the end of the forecast duration. As previously noted, the CPS-KF simulation did remarkably poor with respect to the precipitation forecast at the 36-hour time. It is speculated that the CPS-KF DTE curve behaves in such a manner due to triggering lighter precipitation earlier in the simulation and reduced convective instability throughout the simulation; therefore there is not a sharp increase in DTE following a “spin-up” of convective instability. The other possibility is the CPS-KF simulation may produce precipitation earlier, hence initiating

convective instability prior to the 3-hour forecast time. Upon investigating total forecasted precipitation, it was found that there was a slight increase in rainfall at the 6-hour forecast, however it was not located in the San Antonio area but in northeast Texas (graphic not shown). Therefore, one possibility for the behavior of the CPS-KF simulation is convection initiating in a completely different area at an early time.

5.5 Summary

Following an investigation into practical predictability implications, many questions remained as to the origin and behavior of error growth. Perfect initial conditions and forecast model are assumed, and the evolution of error growth is explored. Through the use of random grid-point perturbations with a specified amplitude, differences between the perturbed and CNTL30km are evaluated across the domain and graphically calculated as a difference total energy. It was found that error growth increased substantially from forecast hours 3-12, following an adjustment of the unbalanced energy variables within the first 3 hours, the error growth slowed but continued to slightly increase for the duration of the simulation time. This error growth was not exclusive to this simulation, and the other model runs exhibited similar error growth behavior. This same assessment holds true for different days throughout the storm event as well as for the opposite phase of the diurnal cycle; in the cases of a morning initialization, the adjustment period was longer as convective instability was initiated during the period of greatest diabatic heating. Perturbation amplitude did not indicate much difference in the peak error magnitude, and there was a saturation of DTE between control and the perturbed simulations towards the end of the forecast. Similar to ZSR03, as the resolution increased, there was greater error growth which resulted in a

limit of forecast value; the implication is if the initial conditions improve substantially, there are marginal improvements in the extent of the mesoscale forecast. Lastly, experiments with different model physics showed similar results, with exception of a "fake-dry" simulation in which latent-heating was turned off. During this simulation, error growth did not occur following the unbalanced adjustment, indicating that such processes that lead to convective instability are one of the primary factors leading to model forecast divergence at the mesoscale.

It is clear through the experiments detailed here that the limits of intrinsic predictability arise from moist processes in general. It has been shown that small random perturbations, essentially representing uncertainties in the initial conditions, can cause substantial forecast errors, particularly in the early forecast times at the mesoscale. These differences can grow multiple times over the initial amplitude. However, it was also shown that given a large perturbation amplitude, the difference growth slows toward the latter part of the forecast period, nearing a saturation point when compared to smaller perturbation amplitudes. Farther discussion of the results will follow in the next chapter.

CHAPTER VI

DISCUSSION AND CONCLUSION

6.1 Summary of the storm event

Beginning on 29 June 2002 and lasting through 6 July, a catastrophic flood event took place in Central Texas, primarily affecting the Edwards Plateau and South Central regions. San Antonio was one of the major metropolitan areas impacted by heavy precipitation. Rainfall totals accumulated to over 30 inches (762 mm) in some communities in Kendall and Comal counties. As evident from the analysis, the principal mesoscale dynamics associated with the heavy rainfall and the formation of an MCS included continual diabatic generation of PV over the same vicinity, continual supply of deep moisture, and little vertical wind shear.

An upper-level PV anomaly was positioned south of Brownsville, Texas, along the Mexican coast. An elongated trough was positioned over central Texas, helping to create a shear zone, and combined with high levels of moisture extending up to 8 km and little vertical shear, a focusing mechanism for convection was present. Positive PV anomalies would advect into the area, due to the return flow around the southern end of the trough. With little convective inhibition, convection would initiate and further diabatic generation of PV ensued. Essentially this resulted in a self-perpetuating system until the northern-most portion of the trough and the associated positive PV was advected into Colorado. As a result of this retrogression, PV advection toward Central Texas diminished, and there was reduced convergence and more vertical shear leading to lower moisture content.

6.2 Discussion of model simulations and results

This research focused on both practical and intrinsic predictability of an extreme weather event, similar to the studies conducted in ZSR02 and ZSR03. The methods employed used the MM5 model with a 30-km resolution to produce a 36-hour control simulation, then conducting several experiments to explore the limits of predictability. To examine the practical predictability issues, simulations testing different lead times, resolution dependence, and various physics parameterization schemes were performed. In addition to the practical experiments, a perfect model and initial condition scenario was assumed to examine intrinsic predictability. For this investigation, random grid-point perturbations were induced to the initial conditions. This was followed by experiments to investigate the predictability due to perturbation magnitude, diurnal variation/different days, resolution error growth, and physics parameterization which includes a "fake-dry" simulation In association with the practical experiments, the changes to the forecast value were considered based on the various simulations.

The reduction in forecast lead time, from 48 to 24 hours, led to a considerably improved precipitation forecast. The rainfall amount and location of the heaviest precipitation improved, which would ultimately increase the value of the forecast. Not only are these different lead-time forecasts subject to practical predictability issues but to intrinsic aspects as well. The small random perturbations that were implemented into the initial conditions would generate differences in the forecasts that would begin at the mesoscale, then these differences would evolve to ultimately affect the sub-synoptic scale features, thus limiting the overall accuracy of the forecast lead-time to nearly 36 hours.

This research showed that a high resolution forecast of accumulated precipitation might be rather inaccurate; there was no indication of heavy convective rainfall totals, nor was there an adequate representation of the precipitation proximity from simulations with a 3.3 km grid spacing. Speculatively, such an inaccurate forecast may stem from the initial conditions, in which the resolution of the data set is 40 km. Also, small errors tend to grow faster at higher resolutions, as was demonstrated in Chapter V. These findings are consistent with those of ZSR03, in which their experiments showed a more rapid error growth early in forecast period, initially near the locations of convective cells, thus indicating that convective instability is not being reached at many of the potentially unstable grid points. With such a poor 36-hour forecast, the value is substantially reduced with respect to practical predictability, and therefore would not have facilitated any warning of the impending flooding rainfall for the ’02 Flood.

The location and quantity of rainfall changed with each parameterization change, more so with the cumulus options than with the microphysics option. Ultimately, the KF simulation had the weakest performance, again reducing the forecast value. Variations from changing physical parameterizations indicate that model errors are still significantly large, thus there is still considerable room for improving forecast models to accurately simulate such an extreme warm-season event.

As previously seen in ZSR03, moist convection plays the most critical role in the rapid error growth. This is noticeable in the first 6 hours of simulation at small scales (ranging from 100-200 km) then spreading to larger scales (approaching 1000 km) by the latter forecast periods. Comparison of simulations with and without temperature perturbations with a standard deviation of 0.2K (which is much lower than the current

observational or analysis errors) randomly distributed over the model grid-points indicated that forecast differences, or forecast errors, spread over the domain and spatial scale, and increased in magnitude as the forecast time increases; the differences predominantly originate at the grid points that are at the threshold of convective instability or neutrality . Without latent heat release, essentially a “fake-dry” simulation, the evolution of error growth was substantially reduced; typically observed with moist convection was a slight decrease of DTE following the first 3 hours of simulation, then a rapid increase of DTE over the next 12 to 18 hours. This was not observed in the fake-dry simulation: following the initial decrease in DTE, there was not a noticeable increase for the rest of the forecast period. Further evidence linking the forecast error growth to convection was found with the examination of the diurnal experiments. When the forecast simulation was initialized at 12Z, when there is weaker convective instability (versus 00Z), there was a greater lag time for the rapid error growth to occur (typically 6 to 9 hours into the model run). This suggests that the errors grew most rapidly with the onset of the strongest convection, since a 12Z initialization is in the morning in Texas, and it would require several hours for destabilization to occur, hence the onset of afternoon convective initiation.

The results demonstrated that, even if forecast models are perfect, intrinsic error growth would ultimately limit predictability, as suggested by Lorenz (1969). It has been shown that forecast errors originate near grid points at the threshold of convective instability at convective scales, then grow and ultimately affect larger scales (up to 800 km) in a 36-hour simulation. This has been represented in both the spectrum analysis and the graphical analysis: the spectrum analysis indicated that the DTE peak was shifting to

higher wavelengths as the forecast extended further from initialization; the graphical analysis shows that the forecast errors spread across the domain and spatial scale, particularly from the 24- to 36-hour forecast timeframe. These findings are consistent with the winter-time extreme event studies in ZSR03, which further exemplifies the constraints placed on the forecast accuracy of the mesoscale models, consistent with Lorenz's theory (1969).

The important question, also proposed in ZSR03, is how far are the present forecast models from the point of diminishing return? With continual advances in computing technology and capabilities, finer resolution simulations can be simulated in a shorter period of time. Excluding intrinsic error considerations, forecast models appear to have substantial room for improvement; this will certainly be aided by not only computing power, but also by better representation of the dynamics that drive the atmosphere. Given the results established in the present research, an accurate forecast representing mesoscale features can have a lead time of approximately 36 hours; beyond this timeframe, forecast value diminishes rapidly, particularly in the forecasting of heavy precipitation. It can be stated that after the initial conditions were considerably improved (upon the current operational analysis error), to reduce the small initial errors by half, this would only lead to an increase in forecast accuracy on the order of hours (not days). In other words, the implication of this research is that even as initial conditions and forecast models improve, there still exists a finite level of predictability.

6.3 Forecasting implications

The motivation behind this research came from the operational difficulty of predicting both the amount of precipitation and the duration of the event. Additional

ramifications due to the heavy rainfall also contributed to the difficulty of forecasting the temperatures, due to extended periods of cloud cover keeping temperatures below normal. This research found that predictability is complicated by moist convection and the associated latent heating feedback. From a practical standpoint, forecast lead time, resolution dependence, and physics parameterizations can greatly impact the outcome, and hence the forecast value, of such events. Although the reduced value that stemmed from higher resolution simulations in this research, it is expected that such resolutions would typically help with the forecast outcome and increase value, provided that the resolution would not be too high to simulate in a reasonable period of time (ZSR03, and references therein).

Intrinsic predictability also limits the value of the deterministic forecast, since errors tend to develop near areas of mesoscale convective instability, then grow to ultimately effect larger scales. However, with an understanding of intrinsic errors leading to different forecast outcomes, perturbations can be established to generate short-range ensembles. Although this is not an innovation, probabilistic forecasts using ensembles stemming from perturbed initial conditions that span the power spectrum can yield a variety of outcomes, which can ultimately provide insight to such extreme events. Utilizing probabilistic results, assessment of risk leading to emergency planning can be established to provide the necessary warnings that could ultimately save money and lives. Not only would such risk assessment benefit emergency preparers, but it would also help any organization or industry whose well-being is impacted by weather and could potentially suffer from such extreme events.

6.4 Further research

This research conducted several experiments exploring the impacts of both practical and intrinsic predictability. Intrinsically, the focus has been on moist convection as a result of a random temperature perturbation. Although ZSR03 established a different perturbation scheme, essentially a constant magnitude perturbation across the grid instead of a random grid perturbation with a set standard deviation. It is speculated that the methods employed in ZSR03 would yield similar results and would not be a consideration for further investigations. Alterations to the land scheme may make a significant difference in both practical and intrinsic predictability, since the upslope effect of the Balcones Escarpment may have contributed significantly to the high moisture content observed in the upper levels. The question is how much of an effect would the topography play on the content of moisture in the upper levels, or would the system still be self-perpetuating due to the lack of vertical wind shear and sufficient convective instability provided by PV.

Changes to the data set that provides the initial conditions should also be considered. ZSR02 utilized a reanalyzed ETA data set as well as analysis provided by the ECMWF. It is certainly plausible that a different data set utilized for the initial conditions may yield different results with regards to practical predictability, particularly for the high resolution simulation. It is also possible that the KF simulation may yield a better forecast with another data set. It would not be expected, however, for the intrinsic results to be different, since the perturbed simulation would be compared to a control simulation using the other data set, and since the results presented in this research coincide with the findings of ZSR03.

Lastly, the use of ensemble forecasts has been proven to be valuable to practical predictability. It can be said that the present research conducted some form of an ensemble of forecasts, a more typical method of ensemble generation should be explored to depict increased value of the forecast from a practical standpoint. One of the initial intents of this research was to apply predictability towards an assessment of risk to be applied to industry and emergency preparedness. Unfortunately, due to time constraints, such an investigation was not conducted. Previous research by Zhu et al. (2002) looked at the economic value of ensemble forecasts. Their study established a simple cost-loss model comparing a forecast with a single control run versus a forecast with an ensemble of outcomes, and it specifically looks at economic ramifications but not societal impacts. A probabilistic forecast could by implemented into a risk model, of cost-loss or a success-failure régime, that could conceivably be applied to a societal or environmental analysis, as well as for economic gain. Through the use of ensembles, outliers can be determined, which can then be employed for economic/hedging decisions, or they can be used to assess a possible outcome for emergency management decisions.

6.5 Conclusion

Throughout this research, both practical and intrinsic predictability have been explored. Experimental method by varying the forecast lead time, resolution dependence, and individual physics parameterization schemes, provided an understanding of the practical complications, using a state-of-the-art forecast model in a 36-hour forecast. Various perturbations were implemented to unperturbed forecasts to ascertain outliers that may contribute to forecast divergence. Similar to results from other predictability studies, there are intrinsic limitations on model forecasts that arise from moist

convection. Resolution also played a critical role, both practically and intrinsically. It is therefore reasonable to conclude that a detailed and accurate forecast of this particular event would be difficult to impossible to predict beyond 2 days.

REFERENCES

Bluestein, H., 1993: *Observation and Theory of Weather Systems*. Vol. 2, *Synoptic-Dynamic Meteorology in Midlatitudes*, Oxford University Press, 594 pp.

Bright, D. R., and S. L. Mullen, 2002: Short-range ensemble forecasts of precipitation during the Southwest monsoon. *Wea. Forecasting*., **17**, 1080–1100.

Caracena, F. and J. M. Fritsch (1983): Focusing mechanisms in the Texas Hill Country flash floods of 1978. *Mon Wea. Rev*., **111**, 2319-2332.

Dudhia, J., 1993: A nonhydrostatic version of the Penn State-NCAR Mesoscale Model: Validation tests and simulation of an Atlantic cyclone and cold front. *Mon. Wea. Rev*., **121**, 1493-1513.

Dudhia, J. and Coauthors, 2001: PSU/NCAR Mesoscale Modeling System Tutorial Class Notes and User's Guide. Boulder, CO: National Center for Atmospheric Research (available online at http://www.mmm.ucar.edu/mm5/doc/html).

Errico, R. M., and D. P. Baumhefner, 1987: Predictability experiments using a high-resolution limited area model. *Mon. Wea. Rev*., **115**, 488-504.

Gallus, W. A., and M. Segal, 2000: Sensitivity of forecast rainfall in a Texas convective system to soil moisture and convective parameterization. *Wea. Forecasting*., **15**, 509-526.

Gochis, D. J., W. J. Shuttleworth, and Z. Yang, 2001: Sensitivity of the modeled North American monsoon regional climate to convective parameterization. *Mon. Wea. Rev*., **130**, 1282-1298.

Grell, G. A., 1993: Prognostic evaluation of assumptions used by cumulus parameterizations. *Mon. Wea. Rev*., **121**, 764-787.

Ham, Joy L., 2001: Using Ensemble Forecasting to Estimate the Background Error Covariance for Mesoscale Data Assimilation. Thesis Proposal, Texas A&M University.

Ham, Joy L., 2002: Mesoscale predictability and background error covariance estimation through ensemble forecasting. M.S. Thesis, Texas A&M University.

Hoskins, B.J., M. E. McIntyre, and A. W. Robertson, 1985: On the use and significance of isentropic potential vorticity maps. *Quart. J. Roy. Meteor. Soc.,* **111**, 877-946.

Kain, J. S. and J. M. Fritsch, 1992: Convective parameterization for mesoscale models: the Kain-Fritsch scheme. *The Representation of Cumulus Convection in Numerical Models, Meteor. Monogr*., No 46, Amer. Meteor. Soc., 165-170.

Kalnay, Eugenia, 2003: Atmospheric Modeling, *Data Assimilation and Predictability*. Cambridge University Press, pp 205-258.

Koller, Glenn. *Risk Assessment and Decision Making in Business and Industry: A Practical Guide*. Florida: CRC, 1999.

Lorenz, E. N., 1963: Deterministic nonperiodic flow. *J. Atmos. Sci*., **20**, 130-141.

Lorenz, E. N., 1969: The Predictability of a flow which possesses many scales of motion. *Tellus*, **XXI**, 289-307.

Lorenz, E. N., 1996: Predictability – a problem partly solved in *Proceedings of the ECMWF Seminar on Predictability*. September 4-8, 1995, Reading, England, Vol. 1, ECMWF, Shinfield Park, Reading, England, 1-18.

Mass, C. F., and D. Ovens, K. Westrick, and B. A. Colle, 2001: Does decreasing horizontal resolution produce more skillful forecasts?. *Bull. Amer. Meteor. Soc.*, **83**, 407-430.

Mellor, G. L., and T. Yamada, 1982: Development of a turbulence closure model for geophysical fluid problems. *Rev. Geophys. Space Phys*., **20**, 851-875.

National Center for Atmospheric Research. Projects sponsored by U.S. weather research program and NOAA radar operations center, image archive. Maintained by Dave Ahijevych. http://locust.mmm.ucar.edu/case-selection/. Accessed on December 10, 2003.

Petroski, T. J. 2000: Numerical simulation of the 16-19 October 1994 Southeast Texas heavy rain event: Precipitation results and diagnosis of the lifting mechanism. M.S. Thesis, Texas A&M University.

Raymond, D. J. and H. Jiang, 1990: A theory for long-lived mesoscale convective systems. *J. Atmos. Sci*, **47**, 3067-3077.

Reisner, J., R. J. Rasmussen, and R. T. Bruintjes, 1998: Explicit forecasting of spercooled liquid water in winter storms using MM5 mesoscale model. *Quart. J. Roy. Meteor. Soc.*, **124B**, 1071-1107.

Schneider, T., and S. M. Griffies, 1998: A conceptual framework for predictability studies. *J. Climate*, **12**, 3133-3155.

Scott, R. K. 2001: The south central Texas heavy rain event of October 1998: An MM5 simulation and diagnosis of convective initiation. M.S. Thesis, Texas A&M University.

Spencer, P. L., and D. J. Stensrud, 1998: Simulating flash flood events: Importance of the subgrid representation of convection. *Mon. Wea. Rev*., **126**, 2884-2912.

Trier, S. B., and C. A. Davis, 2001: Influence of balanced motions on heavy precipitation within a long-lived convectively generated vortex. *Mon. Wea. Rev*., **130**, 877-899.

Tan, Z., and F. Zhang, R. Rotunno, and C. Snyder, 2004: Mesoscale predictability of moist baroclinic waves: Experiments with parameterized convection. *J. Atmos. Sci*, **61**, 1794-1804

Wang, Wei, and N. L. Seaman, 1996: A comparison study of convective parameterization schemes in a mesoscale model. *Mon. Wea. Rev*., **125**, 252-278.

Wyoming, University of. College of Engineering. Department of Atmospheric Science. Upper Air Soundings. Maintained by Larry Oolman. http://weather.uwyo.edu/upperair/souding.html. Accessed on September 6, 2004.

Zhang, F., 2004: Dynamics and structure of mesoscale error covariance in the snowstorm of 24-25 January 2000 estimated through short-range ensemble forecasts. *Mon. Wea. Rev*, in review.

Zhang, F., C. Snyder, and R. Rotunno, 2002: Mesoscale predictability of the "surprise" snowstorm of 24-25 January 2000. *Mon. Wea. Rev*., **130**, 1617-1632.

Zhang, F., C. Snyder, and R. Rotunno, 2003: Effects of moist convection on mesoscale predictability. *J. Atmos. Sci*., **60**, 1173-1185

Zhu, Y., Z. Toth, R. Wobus, D. Richardson, and K. Mylne, 2002: The economic value of ensemble-based weather forecasts. *Bull. Amer. Meteor. Soc*., **83**, 73-83

VITA

Andrew Michael Odins was born in Albuquerque, New Mexico on August 11, 1973. He graduated from the University of New Mexico in December of 1996 with a Bachelor of Science in biology, and a second major in English, with the intent of pursuing a career in the health-sciences. Becoming disenchanted with the potential health-profession careers, he decided to follow his heart's desire to study meteorology. He graduated from The University of Louisiana at Monroe, Louisiana with a second Bachelor of Science in atmospheric sciences in May of 2001.

In August 2001, he began graduate school at Texas A&M University in the Department of Atmospheric Sciences. While in graduate school he worked as the Assistant State Climatologist under the State Climatologist, Dr. John Nielson-Gammon. He is currently employed with Progress Energy Ventures, Inc. in Raleigh, North Carolina. Andrew Odins can be contacted via 1107 Rainesview Lane, Apex, North Carolina, 27502.